

Design and Control of the BlueFoot Platform :  
A Multi-terrain Quadruped Robot

A Thesis  
Submitted in Partial Fulfillment  
of the Requirements for the  
Degree of  
Master of Science (Electrical Engineering)  
at the Polytechnic University

by

Brian Cairl  
May 2015

Master's Examination Committee:  
Copy Number: 1

Approved by:

---

Advisor

---

Date

---

Department Head

---

Date

## VITA

|                    |  |
|--------------------|--|
| Mar 23, 1992 ..... | Born   |
| Sep, 2010 .....    | Entered the NYU Polytechnic School of Engineering as a Mechanical Engineering major and an Honors student.   |
| Jun, 2012 .....    | Completed a minor in Mechanical Engineering.   |
| Oct, 2014 .....    | Submitted a paper to the 2015 International Conference on Robotics and Automation (ICRA) summarizing the design and control of the BlueFoot platform .                 |
| Mar, 2015 .....    | Submitted a paper to the 2015 International Conference on Intelligent Robots and Systems (IROS) on a NARX Neural Network trunk leveling controller for legged robots . |
| Apr, 2015 .....    | Admitted to the NYU Polytechnic School of Engineering as PhD Fellow under the advisement of Professor Farshad Khorrami.  |

I would like to thank Professor Farshad Khorrami for his advisement throughout the course of this project, as well as for his help in guiding my path of study in the fields of controls and robotics during my career as a BS/MS student. The knowledge and skills I have gained under Professor Khorrami's advisement will be invaluable to my future work and continued learning.

I would also like to thank Dr. Krishnamurthy for his guidance in various implementation matters and providing me with invaluable insight to particular problems that I faced during the course of my work. Additionally, I would like to thank my colleague Griswold Brooks for numerous instances of assistance with hardware-related matters during the design and construction of my robot.

*I would like to dedicate this work to my loving mother, father, brother and grandparents for thier love and support through all my endeavors.*

## THESIS ABSTRACT

### POLYTECHNIC UNIVERSITY GRADUATE SCHOOL

**NAME:** Brian Cairl

**QUARTER/YEAR:** Spring 2015

**DEPARTMENT:** Electrical Engineering

**DEGREE:** M.S.

**ADVISER'S NAME:** Dr. Farshad Khorrami

**TITLE OF THESIS:** Design and Control of the BlueFoot Platform : A Multi-terrain Quadruped Robot

This thesis presents the development and control of a small-scale quadruped robot platform with 16 actuated degrees-of-freedom, named “BlueFoot.” The BlueFoot platform has been developed for the purpose of studying multi-terrain navigation and gait control in concert with full-body actuation, which may be used for reorienting payloads (e.g., laser distance sensor and vision-sensor peripherals). This thesis will detail the design of the BlueFoot platform and its hardware sub-systems; an in-depth analysis of the system’s kinematic model and robot dynamics; core Central-Pattern Generator (CPG) based gaiting algorithms introducing reflexive, feedback-driven mechanisms; and a unique foot placement and Zero-Moment Point (ZMP) posture controller based on a virtual force model and a posture feedback loop utilizing inertial measurements.

In addition, this thesis offers a method for disturbance rejection and constant orientation of the trunk of a multi-legged (here a quadruped) robot. This is significant when payloads (such as cameras, optical systems, armaments) are carried by the robot. The trunk is stabilized by the utilization of an on-line learning method to actively correct the open-loop gait generated by a CPG or a limit-cycle method. The learning method is based on a Nonlinear Autoregressive Neural Network with Exogenous inputs (NARX-NN)—a recurrent neural network architecture typically utilized for modeling nonlinear

difference systems. A supervised learning approach is used to train the NARX-NN. The efficacy of the proposed approach is shown in detailed simulation studies of a quadruped robot.

Lastly, this thesis will present several algorithms related to navigation control, terrain modeling, and rough-terrain gait planning. In particular, algorithms for surface reconstruction and foothold planning over uneven terrain will be integral components for future developments related to the BlueFoot project. Results from simulations and actual robot trials will be presented to demonstrate the performance of these control elements.

---

Adviser's Signature  
Department of Electrical  
Engineering

## TABLE OF CONTENTS

|  |            |
|--|------------|
| <b>VITA</b>  | <b>ii</b>  |
| <b>LIST OF FIGURES</b>   | <b>vii</b> |
| <b>LIST OF TABLES</b>  | <b>x</b>   |
| <b>I. Introduction</b>   | <b>1</b>   |
| 1.1 Central Pattern Generators for Gait Control . . . . .          | 3          |
| 1.2 Zero Moment Point Body Placement Control . . . . .             | 5          |
| 1.3 Trunk stabilization . . . . .                                  | 6          |
| 1.4 Potential-Fields Navigation . . . . .                          | 9          |
| 1.5 3D Surface Reconstruction for Rough Terrain Planning . . . . . | 12         |
| 1.6 Overview of Thesis . . . . .                                   | 14         |
| <b>II. Hardware and Design</b>                                     | <b>15</b>  |
| 2.1 Overview and Design Goals . . . . .                            | 15         |
| 2.2 Robot Structure . . . . .                                      | 17         |
| 2.2.1 Main Body (Trunk) Design . . . . .                           | 18         |
| 2.2.2 Leg Designs . . . . .  | 20         |
| 2.3 Computational and Sensory Hardware . . . . .                   | 22         |
| 2.3.1 Device Descriptions . . . . .                                | 23         |
| 2.3.2 Device Networking . . . . .                                  | 26         |
| 2.4 System Power . . . . .   | 27         |
| 2.4.1 Power Routing . . . . .                                      | 27         |
| 2.4.2 Energy Requirements and Runtime . . . . .                    | 28         |

|   |           |
|---|-----------|
| <b>III. Software</b>  | <b>29</b> |
| 3.1 System Software Architecture . . . . .                      | 29        |
| 3.1.1 System Task Allocation . . . . .                          | 30        |
| 3.1.2 Inter-processor Communication . . . . .                   | 33        |
| 3.2 Ground Station . . . . .                                    | 36        |
| <b>IV. System Modeling</b>                                      | <b>38</b> |
| 4.1 Kinematic Model . . . . .                                   | 38        |
| 4.1.1 Forward Position Kinematics . . . . .                     | 38        |
| 4.1.2 Inverse Position Kinematics . . . . .                     | 42        |
| 4.1.3 Range of Motion . . . . .                                 | 43        |
| 4.1.4 Velocity Kinematics . . . . .                             | 44        |
| 4.2 Dynamical Model . . . . .                                   | 46        |
| 4.2.1 System State Vector and General-Form Dynamics . . . . .   | 46        |
| 4.2.2 Joint-Servo Dynamics . . . . .                            | 47        |
| 4.2.3 Single Leg Dynamics . . . . .                             | 47        |
| 4.3 BlueFoot Simulator . . . . .                                | 47        |
| <b>V. Gaiting and Gait-Stability Control</b>                    | <b>51</b> |
| 5.1 Overview . . . . .  | 51        |
| 5.2 Central Pattern Generator (CPG) Based Gaiting . . . . .     | 51        |
| 5.2.1 Reflexive Gait Adaptations . . . . .                      | 53        |
| 5.3 Foot Placement Control . . . . .                            | 55        |
| 5.4 ZMP Based Trunk-Placement Control . . . . .                 | 61        |
| 5.5 Trunk Leveling via NARX-Network Learning Approach . . . . . | 65        |
| 5.5.1 NARX-Neural Network . . . . .                             | 66        |
| 5.5.2 NARX-NN Training Regimen . . . . .                        | 67        |
| 5.5.3 Compensator Output . . . . .                              | 68        |
| 5.5.4 NARX-NN Implementation . . . . .                          | 69        |
| 5.5.5 NARX-NN Compensator Results . . . . .                     | 69        |
| <b>VI. Perception and Navigation</b>                            | <b>75</b> |
| 6.1 Flatland navigation and goal (feature) tracking . . . . .   | 75        |
| 6.1.1 LIDAR-based Potential-Fields Algorithm . . . . .          | 76        |
| 6.1.2 Simulated Potential-Fields Navigation Results . . . . .   | 79        |

|             |  |            |
|-------------|--|------------|
| 6.1.3       | Incorporation of Camera-based Feature Tracking . . . . .                   | 80         |
| 6.2         | Towards Rough Terrain Navigation . . . . .                                 | 83         |
| 6.2.1       | Terrain Mapping from 2D scans . . . . .                                    | 83         |
| 6.2.2       | Height-map Generation from a 3D point cloud . . . . .                      | 85         |
| 6.2.3       | An approach for cost assignment from a height-map . . . . .                | 89         |
| 6.2.4       | A sliding-window approach for sub-optimal rough terrain planning . . . . . | 92         |
| 6.2.5       | Surface Reconstruction . . . . .   | 98         |
| <b>VII.</b> | <b>Concluding Remarks</b>  | <b>102</b> |
| <b>A.</b>   | <b>Leg Jacobian with respect to frame <math>O_{i,0}</math></b>             | <b>105</b> |
| <b>B.</b>   | <b>Fixed-base Leg Dynamics</b>   | <b>106</b> |
| <b>C.</b>   | <b>Summary of Trigonometric Abbreviations</b>                              | <b>109</b> |

## LIST OF FIGURES

|    |  |    |
|----|--|----|
| 1  | The BlueFoot Quadruped Robot . . . . .   | 2  |
| 2  | Parallel NARX-network model with a linear output layer. . . . .  | 7  |
| 3  | The BlueFoot Quadruped Robot: single-camera configuration ( <i>left</i> ); stereo-camera configuration ( <i>right</i> ). . . . .                       | 17 |
| 4  | Root section of trunk. Call-out in top-right shows main-switch access through the bottom of the root module. . . . .                                   | 18 |
| 5  | Main section of trunk. Call-out in the top-right shows how the ODROID-XU and AutoPilot computers fit within the module. . . . .                        | 19 |
| 6  | Head section of trunk. Monocular camera configuration with Hokuyo-URG ( <i>left</i> ); and Stereo configuration with PLDS ( <i>right</i> ). . . . .    | 20 |
| 7  | Closeup of BlueFoot’s leg. ( <i>left</i> ) shows effective link lengths and the location of defined joint positions. . . . .                           | 21 |
| 8  | Series elastic brackets. . . . .   | 21 |
| 9  | BlueFoot device networking diagram. . . . .  | 26 |
| 10 | BlueFoot power routing. . . . .  | 27 |
| 11 | BlueFoot’s on-board processes / signals and their relationships. . . . .   | 31 |
| 12 | Communication flow between processors on the BlueFoot Platform. . . .  | 34 |
| 13 | A visualization of BlueFoot’s coordinate frame configuration. . . . .  | 39 |
| 14 | Range of motion for body’s planar position ( <i>left</i> ) and body pitch and roll ( <i>right</i> ) while in the default stance. . . . .               | 44 |
| 15 | Visualization of the BlueFoot simulator. . . . .   | 48 |
| 16 | Joint position comparison between the simulated and real quadruped while performing a gait which achieves a forward velocity of $60\frac{mm}{s}$ . . . | 49 |
| 17 | CPG output and phase plots for a two-paced gait over two gait cycles. .  | 56 |
| 18 | CPG output and phase plots for a four-paced gait over two gait cycles. .   | 56 |
| 19 | CPG output transition during four-pace to two-pace gait switch. . . . .  | 57 |

|    |  |    |
|----|--|----|
| 20 | Real joint angles during a gait at $65 \frac{mm}{s}$ . . . . .   | 58 |
| 21 | Virtual foothold representation. Blue arrows represent an attractive “force” between the feet and their corresponding virtual foothold. . . . .    | 60 |
| 22 | Stepping pattern generated using virtual-force foothold controller during two-pace gait sequence at $v^r = 40 \frac{mm}{s}$ . . . . .              | 61 |
| 23 | Stepping pattern generated using virtual-force foothold controller during four-pace gait sequence at $v^r = 40 \frac{mm}{s}$ . . . . .             | 62 |
| 24 | Body motion generated using ZMP controller during two-pace ( <i>top</i> ) and four-pace ( <i>bottom</i> ) gaiting sequence. . . . .                | 64 |
| 25 | Quadruped tipping about planted feet. . . . .  | 66 |
| 26 | Full system diagram with NARX-NN compensator mechanism. . . . .  | 70 |
| 27 | NARX Network MSE convergence for trial shown in Figure 32 . . . . .  | 72 |
| 28 | Trunk orientation during $60 \frac{mm}{s}$ gait with $\alpha = 0.125$ . . . . .  | 72 |
| 29 | Trunk orientation during $60 \frac{mm}{s}$ gait with $\alpha = 0.250$ . . . . .  | 73 |
| 30 | Trunk orientation during $60 \frac{mm}{s}$ gait with $\alpha = 0.350$ . . . . .  | 73 |
| 31 | Trunk orientation during $80 \frac{mm}{s}$ gait with mixing parameter set to $\alpha = 0.35$   | 74 |
| 32 | Trunk orientation during $100 \frac{mm}{s}$ gait with $\alpha = 0.35$ . . . . .  | 74 |
| 33 | Potential-field around environmental obstacles. . . . .  | 77 |
| 34 | Path (shown in yellow) taken by robot through a simulated set of rooms and halls using the LIDAR-based potential-fields navigation scheme. . . . . | 79 |
| 35 | Path (shown in yellow) taken by robot through a simulated set of rooms and obstacles. . . . .  | 80 |
| 36 | Path (shown in yellow) taken by robot through a real-world lab setting showing the robot’s view of the goal marker. . . . .                        | 82 |
| 37 | LIDAR swept over a range of angles, $\theta_{b,x} \in [\theta_{b,x,1}^r, \theta_{b,x,N}^r]$ . . . . .  | 84 |
| 38 | Original 3D point-cloud of terrain patch ( <i>top</i> ) and corresponding view from robot’s on-board camera ( <i>bottom</i> ). . . . .             | 86 |
| 39 | A height-map ( <i>left</i> ) and its corresponding gradient ( <i>right</i> ). . . . .  | 88 |
| 40 | Height-map showing terrain variation. . . . .  | 88 |
| 41 | Projections of a sample cost-tensor generated from the height-map shown in Figure 39. . . . .  | 92 |
| 42 | Path planned over rough terrain with $d_w = d_u = 1$ . . . . .   | 94 |
| 43 | Path planned over rough terrain with $d_w = d_u = 5$ . . . . .   | 95 |



## LIST OF TABLES

|    |  |    |
|----|--|----|
| 1  | Link and body-offset lengths for each leg. . . . .   | 22 |
| 2  | System communication port-pairs and corresponding data transfer rates . .  | 26 |
| 3  | Power consumption summary by device (for single-camera configuration). .   | 28 |
| 4  | Battery power supply and estimated runtime summary. . . . .  | 28 |
| 5  | Structure of the packets sent from Ground-Station to TM4C. . . . .   | 34 |
| 6  | Structure of the packets sent from the TM4C to the Ground-Station. . .   | 35 |
| 7  | Structure of the packets sent from the RM48 to the ODROID. . . . .   | 35 |
| 8  | Structure of the packets sent from the ODROID-XU to the RM48. . . . .  | 36 |
| 9  | DH parameters for all legs. . . . .  | 40 |
| 10 | Imposed joint limits. . . . .  | 43 |
| 11 | Physical joint limits. . . . .   | 44 |
| 12 | Locations for the platform and feet when in the default stance, written with respect to the frame $O_{b'}$ . . . . . | 44 |
| 13 | Sum of costs for four path-planning trials with varying initial positions varying optimization windows. . . . .      | 93 |

## CHAPTER I

### Introduction

The design of legged robots and associated methods of locomotion control has been an area of interest spanning the past several decades, as shown by [1–5]. Quadruped robotic systems have gained popularity in studies pertaining to variable terrain navigation and full-body stability adaptation. Well known examples of this from the past 15 years are the Tekken [6], Kolt [7], BigDog [8], and HyQ [9] quadrupeds. Many of these systems have been implemented on a larger scale so that they can carry substantial payloads while maintaining adequate system bandwidth for fast gaits and robustness to rough terrains. Few, however, have been implemented on the scale of a hobby-robot platform while still maintaining an aptitude for rough terrain navigation and comparable sensory prowess.

The BlueFoot quadruped is a self-contained, fully-actuated platform with the dexterity to perform stabilization and repositioning maneuvers on variable terrains along the same lines as the LittleDog platform [10]. BlueFoot has been designed with sixteen actuated degrees of freedom to allow for the execution of a wide range of body and leg articulations. This level of dexterity grants the BlueFoot platform the ability to articulate its trunk (main body) over a range of poses, as well as overcome raised or uneven terrain.

BlueFoot is outfitted with several on-board vision sensors, including a LIDAR and camera, which are mounted to its trunk (main body). BlueFoot can articulate (*i.e.*, pitch and yaw) these sensors by posing its trunk using aggregate leg motion controls. BlueFoot also includes a sizable array of other on-board sensors for feedback and control, including joint position, velocity and loading sensors; an inertial measurement unit (IMU); a magnetometer; a GPS unit; humidity and temperature sensors; and foot-contact sensors. Using the computational, sensory and motor capacities at hand, BlueFoot has the ability to utilize similar control mechanisms to those implemented on larger quadruped systems.

The BlueFoot platform inherently demands active control to achieve locomotion

and system stability, making this robot an ample platform for studies related to gait design and motion planning. In particular, BlueFoot’s controllers make direct use of the system’s kinematic model and involve applications of open-loop gait design and stabilization for the purpose of achieving dynamic locomotion control. In particular, BlueFoot is gaited via a central pattern generator (CPG) based technique which is augmented with a foothold controller along the same lines as [11] and [12]. Active platform stabilization is performed via a zero-moment point (ZMP) based body placement controller which stabilizes the system using planar trunk motions during arbitrary gaiting sequences. Both such controllers make use of virtual-forces to drive system reference commands. These controllers apply BlueFoot’s forward kinematic model for the purpose estimating joint and foot positions. Finally, outer-loop control routines are implemented to supply commands and corrections used in system navigation control. Among these controllers are a potential-fields navigation controller, which incorporates image-feature tracking; and 3D point-cloud processing routines for surface reconstruction and foot-placement planning.



Figure 1: The BlueFoot Quadruped Robot

## 1.1 Central Pattern Generators for Gait Control

As previously mentioned, BlueFoot’s core gaiting routine relies on the utilization of artificial Central Pattern Generators (CPGs). This control mechanism is inspired from biological neural networks which generate rhythmic motions [13]. Biological CPGs are described in [14] as a form of self-organizing cellular neural network with the role of limited feedback in CPG networks. In fact, a key feature of these networks is that they can act without explicit sensory feedback inputs or directions from a higher-level command unit, such as a brain. Instead, signals emanating from independent motor units (and, sometimes, feedback gathered from sensory neurons) are utilized to trigger or inhibit a sequence of successive, self-coordinated motor operations. These activation sequences create loops which give rise to cyclic motion patterns.

In robotics, biological CPG’s are modeled via an artificial counterpart which applies multi-state unit-oscillators to represent neural units. The dynamics of each unit oscillator in an artificial CPG network are designed to influence the dynamics of other network oscillators through tunable coupling parameters. Typically, the coupled oscillator network is implemented on a digital controller, which numerically integrates the dynamics of each neural oscillator. The output states of each unit-oscillator are used to drive selected robot degrees of freedom. Oscillator outputs could also be used for planning periodic motions in the robot’s task space, which are then translated into the joint-space references via an inverse kinematics mapping, as is done in BlueFoot’s gait control routine. In implementation, specific motions are achieved through careful tuning of oscillator coupling parameters which incurs particular phase offsets between the individual limit-cycles produced by each unit-oscillator. The ability to coordinate unit-oscillator dynamics is what allows artificial CPGs to be used in the control of higher-level motor tasks, such as walking or crawling.

The selection of a unit-oscillator for use in a CPG network is a fundamental matter in CPG network design. CPG networks can be designed to employ unit-oscillators with varying oscillator dynamics (*i.e.*, varying number of states, tuning parameters, etc.) which exhibit different limit-cycle behaviors. Hopf Oscillators are used in BlueFoot’s CPG implementation, as well as in [12, 15, 16]. Other unit-oscillator types which have been applied to CPGs include Van der Pol Oscillators, as detailed in [13], and the Matsuoka Neural Oscillator [17].

Studies dealing specifically with the application of CPG’s to multi-legged robot gait-

ing (*i.e.*, quadrupeds, hexapods and octopodal robots) have been carried out in [18–27]. In particular, [13] states that the attractiveness of CPG’s in the control of legged robot locomotion lies in the ability to decouple robot motor control, *i.e.*, walking, from higher-level planning, such as navigation and body-posture control. Additionally, CPG’s offer an effective way for smoothly switching between gaiting patterns, such as walking, trotting, or pacing, simply through the modification of a few control parameters. Moreover, the application of artificial CPG’s greatly reduces the dimensionality of the gaiting control problem for legged robots.

The specific CPG controller implemented on the BlueFoot robot allows for the generation of coordinated motions which can be modified to yield different overall motion patterns without explicitly directing the motion each joint. Moreover, BlueFoot’s CPG controller does not use a separate unit-oscillator to control the motion of each joint. Instead, four unit-oscillators are used to control the motion of each *foot*. In doing so, CPG outputs are mapped to stepping trajectories in the robot task-space. The resulting task-space reference commands are mapped into angular joint position references using an inverse kinematics solution for the entire robot. This approach gives way to a hybrid gaiting mechanism which combines the conveniences of CPG-based gaiting with the explicitness of strict foot trajectory planning. In BlueFoot’s control scheme, foot-placement is prescribed via a separate planning mechanism which is entirely decoupled from the CPG gait controller. This controller hybridization allows a CPG-based motion generator to be applied to gaiting over varying terrains.

Another important aspect of BlueFoot’s CPG implementation is the incorporation of feedback mechanisms which modify CPG parameters. The use of feedback towards improving gaiting stability in CPG-based applications was inspired by the work of [6, 17]. For our purposes, BlueFoot’s CPG-based gait generation incorporates inertial feedback signals into its CPG mechanism to modify unit-oscillator amplitudes and modulate unit-oscillator frequencies. Coupling the unit-oscillator dynamics with sensory feedback gives rise to *reflexive* motions which can be tuned to help prevent the system from excessive tipping during gaiting. Reflexive motion incorporation, as it is applied into BlueFoot’s CPG gaiting scheme, will be covered in more detail in Section 5.2.

Due to the fact that CPG-based gaits are inherently open-loop motion control routines, a combination of auxiliary mechanisms must be used in concert with the CPG gait controller in order to ensure system stability during gaiting. The incorporation of feedback signals to modify CPG parameters aids in achieving stability although it

might be insufficient for stable walking over exclusively uneven terrains. Additionally, this method requires very careful parametric tuning to perform robustly under a larger variety of terrain conditions. Thus, other means of stabilization have been incorporated into BlueFoot’s gaiting routine to aid in stability.

BlueFoot’s core stabilization routine applies a concept named *artificial synergy synthesis*. Using this technique, gait control is carried out independently of a stabilization control. Namely, body stabilization is performed by a subset of the robot’s degrees of freedom while gaiting is carried out by the remaining [28, 29]. In original implementations of this technique, adaptations to trunk motion were utilized to stabilize the overall motion of the robot utilizing a zero moment point (ZMP)-based approach while gaiting is controlled by a fixed-motion routine. Here, body and foot-placement are both controlled as independent, dynamic routines which supply reference commands in the robot task-space.

## 1.2 Zero Moment Point Body Placement Control

The zero-moment point (ZMP), which is equivalent to the center of pressure (CoP), is formally defined as a point on the ground beneath a walking system at which the net moment acting upon the trunk (referred to as the *tipping moment*) is zero [30]. The concept of ZMP and its application to legged robotics was originally introduced by [28] and expanded upon in [31]. Both such studies apply ZMP theory towards the control of biped robots.

Formally, the ZMP can be defined using a formulation for the CoP wherein the moments about  $\tau_x$  and  $\tau_y$ , the lateral tipping-moments applied to the robot’s body in the world frame, are equal to zero. It will be denoted  $p_{ZMP}$ . The solution for  $p_{ZMP} \in \mathcal{R}^3$ , with respect to a set of  $N$  foot contact points  $p_{i,e} \in \mathcal{R}^3$  and  $N$  associated applied foot-contact forces  $f_{i,e} \in \mathcal{R}^3$ , arises as a bounded set of solutions to the equation

$$\sum_{i=1}^N (p_{i,e} - p_{ZMP}) \times f_{i,e} = \begin{bmatrix} \tau_x \\ \tau_y \\ \tau_z \end{bmatrix} = \begin{bmatrix} 0 \\ 0 \\ * \end{bmatrix} \quad (1.1)$$

where  $z$ -coordinate of  $p_{ZMP}$ ,  $[p_{ZMP}]_z$ , is strictly zero when the walking surface is flat, as shown in [5]. Here, derivations for flat-surface ZMP motion will be described, but equations associated with this technique can be extended to non-flat terrain motion in a straight-forward way with a conceptually equivalent end result. The following expression

is derived from dynamical equations which describe the total angular momentum,  $\dot{L}$ , about the legged system's center of gravity (COG),  $p_{COG}$ :

$$\dot{L} = \sum_{i=1}^N p_{i,e} \times f_{i,e} - m_T p_{COG} \times (\ddot{p}_{COG} + \vec{g}) \quad (1.2)$$

where  $m_T$  is the total mass of the legged system and  $\vec{g}$  is the standard gravity vector. Assuming that all points of foot-contacts exist on a flat plane, *i.e.*,  $[p_{i,e}]_z = 0 \forall i = \{1, \dots, N\}$ , and all contact force,  $f_{i,e}$  are pointing upward, the  $p_{ZMP}$  of the system can be written as

$$p_{ZMP} = \frac{\sum_{i=1}^N (p_{i,e} \times f_{i,e})}{\left[ \sum_{i=1}^N f_{i,e} \right]_z} = \frac{p_{COG} \times (\ddot{p}_{COG} + \vec{g}) + \dot{L} m_T^{-1}}{[\ddot{p}_{COG} + \vec{g}]_z} \in \mathcal{C}_{ZMP} \quad (1.3)$$

where

$$\mathcal{C}_{ZMP} = \text{conv}(p_{1,e}, p_{2,e}, \dots, p_{N,e}) \quad (1.4)$$

with  $\text{conv}(\ast)$  defining a convex hull generated from a set of input points  $(\ast)$ .  $\mathcal{C}_{ZMP}$  is used to represent the solution space of  $p_{ZMP}$ . Moreover,  $\mathcal{C}_{ZMP}$  places a bound on the angular momentum  $\dot{L}$  which results from contact variations presented through  $p_{i,e}$  and  $f_{i,e}$ . Setting  $\dot{L} = 0$ , a condition is defined for zero tipping. For BlueFoot's ZMP controller formulation, it is also assumed that the acceleration of the COG is sufficiently small, *i.e.*,  $\ddot{p}_{COG} \approx 0$  which yields the following, intuitive condition for minimal tipping:

$$\|p_{ZMP} - p_{COG}\| < \epsilon \quad (1.5)$$

where  $\epsilon$  is a scalar bounding constant used to ensure  $p_{COG}$  also falls within the bounded set  $\mathcal{C}_{ZMP}$ . Thus, the general idea of this ZMP-based controller is to compute an approximate ZMP location and place the center of the robot's trunk (described by the translation  $p_b$ ) such that the platform's COG approaches its associated ZMP for some arbitrary kinematic configuration. This is done in an effort to reduce  $\|\dot{L}\|$ , so as to avoid tipping about the contacting feet.

### 1.3 Trunk stabilization

In addition to the aforementioned task-space controllers, a learning controller, which features the use of a NARX neural network (NARN-NN), has been studied and evaluated. In essence, this controller learns to approximate disturbance dynamics during periodic gait routines and corrects trunk orientation by administering adaptations to



Figure 2: Parallel NARX-network model with a linear output layer.

joint position controls. The goal of this NARX-NN based control routine is to achieve a level trunk during locomotion.

A NARX-NN architecture is used in this controller because of its known effectiveness in approximating nonlinear difference systems and making multivariate time-series predictions [32–35]. Moreover, the NARX-NN is a natural fit for a problem of this nature where the dynamics being considered are both periodic and of a high enough complexity where a nonlinear approximation method is warranted. The parallel NARX-NN model, shown in Figure 2, is comprised of a feed-forward neural network whose input layer accepts a series of time-delayed system state values and network-output histories. The NARX-NN is trained to predict system states in the next time-instant from these inputs. Conveniently, NARX-NN training can be performed using standard error back-propagation because recurrence occurs between network inputs and outputs, and not within the hidden layers [36].

An alternative NARX-NN architecture is the series-parallel NARX-NN, in which network prediction target-values are supplied as inputs, as opposed to true network outputs. This formulation is not truly recurrent, but can be trained in the same way as the

parallel NARX-NN. As such, this type of network has different convergence characteristics as compared to the parallel NARX-NN. This NARX-NN showed slower convergence than the parallel NARX-NN for the trunk-leveling application to be presented and was not used in the final implementation.

In this controller implementation, the NARX-NN is trained to capture the effects of forces, moments and dynamical couplings that act on the trunk so that an appropriate torque inputs to the joints can be computed. These torque inputs are then used to reduce disturbance effects on trunk orientation while performing the gate. This is achieved by considering the inverse dynamics corresponding to joint motion.

NARX-NN training is performed on-line using the standard incremental back-propagation (BP) algorithm with an adapted learning rate,  $\gamma^{lr}$  and momentum term,  $\mu$  [37,38]. This error BP algorithm [39] is a gradient-descent based method used to train a feed-forward neural network with  $n$ -layers and layer-connection matrices  $\{W^1, W^2, \dots, W^{n-1}\} \in W$ . The BP algorithm, as used in this control approach, is as follows:

$$\begin{aligned}\Delta W^i &\leftarrow -\gamma^{lr} \delta^i (o^{i-1})^T + \mu \Delta W^i \\ W^i &\leftarrow W^i + \Delta W^i\end{aligned}\tag{1.6}$$

where

$$\delta^i = (\nabla_y \sigma^i (y^i)) e^i$$

$$y^i = W^i o^{i-1}$$

$$e^i = (W^i)^T \delta^{i+1} \quad \forall i \neq n,$$

and  $\gamma^{lr} \in [0, 1]$  defines the learning rate;  $\mu \in [0, 1]$  defines the learning momentum;  $W^i \in \mathcal{R}^{N_O^i \times N_I^i}$ , define the weighting matrix between the  $i^{th}$  layer (of size  $N_I^i$  nodes) and  $(i+1)^{th}$  layer (of size  $N_O^i = N_I^{i-1}$ );  $\Delta W^i$ , defines the corresponding weight update to  $W^i$ ; and  $e^i$  is the output error for each  $i^{th}$  layer. For the output ( $n^{th}$ ) layer,  $e^n$  is equal to the difference between the network output and the network output target, which will be defined later. For all other layers,  $e^i$  represents a *back-propagated* error. from the  $(i+1)^{th}$  layer.

$\sigma^i(y^i)$  is an element-wise activation function which outputs a vector of activation outputs,  $\sigma_j^i(y_j^i)$  for each  $j^{th}$ , weighted input,  $y_j^i$ , defined as follows:

$$\left\{ \sigma^i(y^i) = \left[ \sigma_1^i(y_1^i), \dots, \sigma_{N_I^i}^i(y_{N_I^i}^i) \right]^T : \mathcal{R}^{N_I^i} \rightarrow \mathcal{R}^{N_I^i} \right\}\tag{1.7}$$

For the trunk-leveling controller described in Section 5.5, a symmetric sigmoid activation function is used as a hidden-layer activation function. Formally

$$\sigma_j^i(y_j^i) \equiv \tanh(y_j^i) \in [-1, 1]. \quad (1.8)$$

Hence, the gradient which arises for the activation mapping at each hidden layer,  $\nabla_y \sigma^i(y^i)$ , is defined as follows:

$$\nabla_y \sigma^i(y^i) = \begin{bmatrix} 1 - (\sigma_1^i(y_1^i))^2 & 0 & \dots & 0 \\ 0 & 1 - (\sigma_2^i(y_2^i))^2 & 0 & \vdots \\ \vdots & 0 & \ddots & 0 \\ 0 & \dots & 0 & 1 - (\sigma_{N_I^i}^i(y_{N_I^i}^i))^2 \end{bmatrix} \quad (1.9)$$

(1.9) results from the derivative properties of the tanh (\*) function. For the output layer, a linear activation function is used to avoid output scaling issues. This activation function is defined simply as:

$$\sigma^O(y^O) = y^O \in \mathcal{R} \quad (1.10)$$

with  $\nabla_y \sigma^O(y^O)$  defined as:

$$\nabla_y \sigma^O(y^O) = I_{N_I^O \times N_I^O}. \quad (1.11)$$

The success of this learning mechanism, as it applies to the trunk-leveling controller to be presented, is predicated on the periodicity of the system dynamics during gaiting. Like any BP-trained neural network, repetition of similar input and output sets is paramount for successful network training and, by extension, prediction accuracy. It is assumed that this specification can be met given the inherently cyclic nature of the dynamics being estimated during gaited locomotion.

## 1.4 Potential-Fields Navigation

The method selected for navigating the BlueFoot platform over flatland is a potential-fields control approach. This approach is described in [40] for the purpose of controlling robotic manipulators, and analyzed in-depth in [41]. In particular [41] presents shortcomings of this approach, which will be covered in-brief later in this section. Despite its pitfalls, potential-fields navigation methods offers a relatively simple and intuitive approach to robot navigation and fits well into mobile robotic tasks which involve “wandering”-type navigation over flat-regions. In particular, this approach is applied to situations where the robot has yet to acquire any knowledge of its surroundings. In

the approach to be presented, potential-fields navigation is coupled with a camera-based feature tracking, which is used to guide the robot towards features of interest within the unknown environment.

The potential-fields approach is used in mobile robot navigation by moving the robot according to a guiding virtual force-vector,  $F_{nav}$  [41, 42]. This vector is comprised of a sum of virtual repulsive forces,  $F^-$  (typically generated from range-sensor data), and virtual attractive forces,  $F^+$ , which pull the robot towards known goals. Moreover,  $F_{nav}$  formally defined as:

$$F_{nav} = F^+ + F^- \quad (1.12)$$

The general form for the force components  $F^+$  and  $F^-$  (represented as  $F_c$  in equation (1.13)) is as follows:

$$\begin{aligned} d_k &= p_{POI,k} - p_{robot} \\ F_c &= \alpha_F \sum_k \left( f(\|d_k\|) \frac{d_k}{\|d_k\|} \right) \end{aligned} \quad (1.13)$$

where  $p_{POI,k}$  and  $p_{robot}$  represent the position of each  $k^{th}$  point-of-interest (POI) and the position of the robot platform;  $f(*)$  is a potential function which returns a scalar potential factor with respect to a scalar argument (\*); and  $\alpha_F$  is a scaling parameter which is positive when the POIs considered represent goals and negative when POIs represent obstacles to avoid. The potential function,  $f(*)$ , and scaling factor,  $\alpha_F$ , are designable for particular applications. For BlueFoot's navigation scheme, attractive and repulsive forces are generated using a consolidated, piecewise forcing function which is used to guide through an environment where a goal is not specified before hand.

According to [41] the main pitfall with potential-fields navigation is susceptibility to local minima within the global force-field. At a local minimum, the  $F^+$  and  $F^-$  are of nearly equal magnitude, causing the magnitude of the total guiding force vector,  $F_c$ , to be close to zero. In practice, reaching a point at which robot will be completely stationary is unlikely, as sensor readings used to observe environmental obstructions are corrupted by noise. In turn, this noise induces random perturbations in the robot's motion. In fact, perturbations due to sensor noise could actually aid in relieving a situation in which a robot is stuck in a local minima. However, the gradient of the force-field around a minimum point could be very steep over a large area around the aforementioned singularity. These type of potential-sink regions could cause the robot to

exhibit limit-cycle behavior as it periodically overshoots and re-attracts to the location of the force-minimum.

This can be overcome, in part, by adding an artificial *inertia* (essentially a tunable gain parameter) when updating the robot's navigation reference signals. Given a set of robot navigation command parameters,  $v^r$  and  $\omega^r$ , and potential reference outputs,  $v_L^r$  and  $\omega_L^r$  (which are generated from  $F_{nav}$ ), navigation updates with an added update-inertia,  $B^r \in \mathcal{R}^{2 \times 2}$ , exhibit the following controller dynamics:

$$\begin{bmatrix} \dot{v}^r \\ \dot{\omega}^r \end{bmatrix} = B^r \left( \begin{bmatrix} v_L^r \\ \omega_L^r \end{bmatrix} - \begin{bmatrix} v^r \\ \omega^r \end{bmatrix} \right) \quad (1.14)$$

where  $B^r$  is a strictly positive definite, diagonal “inertia” matrix. This control formulation is equivalent to an outer-loop P-control scheme. Using this update scheme may cause the robot platform to sufficiently overshoot minimum points such that it leaves the local attraction field. Care must be taken in the selection of  $B$ , however, so that system still exhibits stable behavior during navigation control. A more sophisticated approach to escaping local minima is mentioned in [43], which involves a “stuck” detection algorithm. The idea behind such an algorithm involves a deduction about whether or not the robot is captured in a local minima based on samples of the robots motion state (*i.e.*, position and velocity). Once the robot has determined that is it stuck, it executes a small random-walk as a means of escape.

The local minima problem is addressed through the use of auxiliary (possibly dynamic) target points, as done in [42] via a hybrid navigation potential-fields/visual-servoing scheme. Instead of incorporating goal points directly into the potential-fields scheme, goals (in this case, image features) are tracked using an entirely separate navigation scheme. A separate set of navigation reference commands,  $v_C^r$  and  $\omega_C^r$ , are mixed with commands generated via the potential-fields algorithm. The amount of influence either command scheme has over the final navigation command parameters,  $v^r$  and  $\omega^r$ , depends on relative measure of “closeness” to the object being tracked, which the robot determines from an image processing routine. The specifics of the visual-servoing controller will be described in VI.

Hence, the potential-fields portion of this control scheme is used only for the purpose of avoiding potential obstructions, sensed via LIDAR range data. Image-features are used in a visual-servoing routine which guides the robot toward features-of-interest which fall within the robots camera gaze. This approach offers the ability to manually guide the

robot during navigation, by either a human overseer, or a partner robot (which could wear trackable markers), as it performs an independent obstacle avoidance routine. The advantage of this approach lies in its simplicity, as it relies only on immediate environmental samples and, thus, has relatively minimal implementation demands. As a mechanism for partially-guided wandering-type (random) navigation within an unknown region, this approach is certainly adequate as will be shown via empirical results from real-world trials.

## 1.5 3D Surface Reconstruction for Rough Terrain Planning

The previously introduced navigation scheme is utilized for navigation over flat-land, exclusively. As such, it is generally insufficient for navigation and planning over rough terrain. Navigation and footstep planning over rough terrain require the acquisition of 3D surface data from the robots immediate environment, generally with high feature detail. This thesis will provide the preliminaries for rough-terrain navigation by way of several surface reconstruction/representation methods from point-cloud data. First, a method for composing 3D point clouds from successive 2D LIDAR scans will be described. Then, algorithms for generating 3D height-maps will be described and a method for cost assignment based on generated height-maps will be presented for use in rough terrain foot-placement planning. Finally, an implementation for surface reconstruction from raw point-cloud data will be described.

Work related to height-map generation and associated cost-assignment (used in generating discrete cost-maps) from 3D point cloud data is formulated from an intuitive evaluation of the problem of rough-terrain planning. This work should be viewed as the initial steps towards formal rough terrain planning which will later be solidified with existing research. On the other hand, implementations related to 3D surface reconstruction from 3D point clouds rely heavily on algorithms originally outlined in [44] and formally implemented in the OpenPCL library [45].

Surface estimation from 3D point cloud data is approached by way of successive plane-fitting (normal estimation) via Principle Component Analysis (PCA) on a moving subset of points [44, 46]. Specifically, a normal vector is associated with each point,  $\bar{x}_i$ , within the point cloud,  $\bar{\mathcal{S}}$ , by fitting a plane to a subset of neighboring points which fall within a unit-ball (of radius  $d_s$ ) around  $\bar{x}_i$ . Here,  $\bar{\mathcal{S}}$  represents a raw 3D point cloud. This point cloud is pre-conditioned to generate a sparser point cloud,  $\hat{\mathcal{S}}$ , which estimates the collection of points  $\bar{\mathcal{S}}$ . Preconditioning involves a voxel-grid filter, which is used to

down-sample the original point cloud; and a moving-least-squares (MLS) filter, which is used to regularize points and remove outliers. These preconditioning routines aid in the normal estimation process by decreasing computational burden of the estimation algorithm. This is achieved by reducing the density of the space which must be searched for nearest neighbor points about each  $\bar{x}_i$ . Preconditioning also improves the relative smoothness of the reconstructed surface [44].

To estimate a local plane (via PCA) about the point  $\bar{x}_i$ , we define a moving-neighborhood,  $\mathcal{B}_{\bar{x}_i}$ , as follows:

$$\{\bar{x}_j \in \mathcal{B}_{\bar{x}_i} : \|\bar{x}_j - \bar{x}_i\| < d_s, \forall i \neq j\}, \mathcal{B}_{\bar{x}_i} \subset \bar{S}. \quad (1.15)$$

Additionally, the covariance matrix,  $C_{\bar{x}_i} \in \mathcal{R}^{3 \times 3}$ , of the subset  $\mathcal{B}_{\bar{x}_i}$  is defined as:

$$C_{\bar{x}_i} = \frac{1}{S(\mathcal{B}_{\bar{x}_i})} \sum_{\bar{x}_j \in \mathcal{B}_{\bar{x}_i}} (\bar{x}_j - \bar{x}_{c,i})(\bar{x}_j - \bar{x}_{c,i})^T \quad (1.16)$$

where the centroid,  $\bar{x}_{c,i} \in \mathcal{R}^3$ , of the subspace  $\mathcal{B}_{\bar{x}_i}$  is defined as:

$$\bar{x}_{c,i} = \frac{1}{S(\mathcal{B}_{\bar{x}_i})} \sum_{\bar{x}_j \in \mathcal{B}_{\bar{x}_i}} \bar{x}_j \quad (1.17)$$

and  $S(\mathcal{B}_{\bar{x}_i})$  defines the number of points within  $\mathcal{B}_{\bar{x}_i}$ . Note that  $C_{\bar{x}_i}$  is a positive semi-definite matrix with all eigenvalues,  $\lambda_{x_i,j} \geq$  for  $j \in \{1, 2, 3\}$  such that  $\lambda_{x_i,1} \leq \lambda_{x_i,2} \leq \lambda_{x_i,3}$ . The unit-eigenvectors  $v_{x_i,j}$  for  $j \in \{1, 2, 3\}$  represent the principal components of the local subspace  $\mathcal{B}_{\bar{x}_i}$ , and are defined by:

$$\{v_{x_i,j} \in \mathcal{R}^3 : C_{\bar{x}_i} v_{x_i,j} = \lambda_{x_i,j} v_{x_i,j} \forall j \in \{1, 2, 3\}\}. \quad (1.18)$$

The eigenvector  $v_{x_i,1}$  with corresponding smallest eigenvalue  $\lambda_{x_i,1}$  represents a unit-normal which emanates from a 2D manifold of  $\mathcal{B}_{\bar{x}_i}$  whose origin is located at  $x_i$ . This manifold represents a planar least-squares best-fit for the information contained in  $\mathcal{B}_{\bar{x}_i}$ . To fortify this definition, we can also consider that the minimum eigenvalue  $\lambda_{x_i,1}$  indicates that  $v_{x_i,1}$  is a direction in  $\mathcal{B}_{\bar{x}_i}$  with the lowest variational *energy*. Hence, the sum of the square-errors among all points in  $\mathcal{B}_{\bar{x}_i}$  is minimized in the  $v_{x_i,1}$  direction.

Given a preprocessed point cloud  $\hat{\mathcal{S}}$  (generated from a raw point cloud  $\bar{S}$ ), the full normal-estimation algorithm is then implemented using the PCA formulation defined from (1.15)-(1.18) in Algorithm 1, to follow. Here,  $\vec{n}_i \in \hat{N}_{\mathcal{S}}$  represents a normal emanating from each  $i^{th}$  point,  $\hat{x}_i \in \hat{\mathcal{S}}$ .

---

**Algorithm 1** Surface-normal estimation from a preprocessed 3D point cloud.

---

```
init:  $\hat{\mathcal{S}}, \hat{N}_{\mathcal{S}} = \phi$ 
for all  $\hat{x}_i \in \hat{\mathcal{S}}$  do
     $\mathcal{B}_{\bar{x}_i} = \text{getNearestNeighbors}(\hat{\mathcal{S}}, \hat{x}_i, d_s)$ 
     $\vec{n}_i = \text{performPCA}(\mathcal{B}_{\bar{x}_i})$ 
     $\hat{N}_{\mathcal{S}} \leftarrow \hat{N}_{\mathcal{S}} \cup \vec{n}_i$ 
end for
```

---

## 1.6 Overview of Thesis

This thesis will first detail the major hardware components; design considerations; and construction of the BlueFoot platform in Chapter II. Next, BlueFoot’s software and processing architecture, applied in the control the BlueFoot platform, will be described in Chapter III. The kinematic and dynamical models of the BlueFoot system will be described in Chapter IV, followed by descriptions of the controllers which are presently implemented to gait and stabilize the platform in Chapter V. Chapter VI will cover navigation algorithms applied to the BlueFoot platform, including preliminary approaches for rough-terrain planning. Finally, Chapter VII will contain concluding statements about the system’s design and control, including remarks about possible future directions of study related to the BlueFoot platform and legged robotics as extensions of the existing work.

## CHAPTER II

### Hardware and Design

#### 2.1 Overview and Design Goals

The BlueFoot quadruped robot is designed as a small-scale, general-purpose legged mobile platform with enough physical dexterity and on-board computational/sensory power to perform complex tasks in variable environments. BlueFoot is designed as a standalone unit and, thus, does not require power tethering or off-board processing. As such, BlueFoot's sensory, computational and power-source outfit make it capable of performing tasks which require full autonomy.

The implementation of a legged robot which meets these general specification is inherently bottlenecked by several well-known shortcomings which plague legged robot design. These drawbacks can be summarized as follows: relatively low payload capacity, as leg joints are often subjected to substantial dynamic torque loading during gaiting; and higher power consumption due to a, typically, larger number of total actuators. Thus, a general-purpose, multi-legged system like the BlueFoot platform must ultimately achieve a balance between payload-carrying capacity (i.e. maximum joint-servo output torque); actual on-board payload; and on-board energy supply. It is desirable that the sensory and computational power; as well as overall mobility of a legged system are simultaneously maximized along with the aforementioned characteristics.

The design goals which have guided the implementation of the BlueFoot quadruped have been tailored to yield a system design which is both feature rich, computationally powerful, and exploits the natural dexterity and terrain handling of legged robotic systems. The design process followed to facilitate these goals consisted of four interdependent decision phases, which were as follows:

1. deciding what type of sensor/computational components would be included on the platform
2. deciding the intended runtime

3. deciding the robot's kinematic/structural configuration
4. deciding what type of servo actuators would be used.

Following the aforementioned design process, BlueFoot's sensor/computational payloads were planned first. BlueFoot was originally designed to incorporate an in-house designed AutoPilot unit and a high-duty computer unit, which were initially estimated to make up roughly 0.25 kg of the system's total weight and consume approximately 15 Watts of power during nominal operation. Additionally, BlueFoot was to be outfitted with up to two web cameras and a LIDAR unit. These sensors were, collectively, estimated to add an additional 0.35 kg and consume 3.5 Watts. The weight of all other payloads (*i.e.*, circuit board, wireless radios, cables) was estimated to make up roughly 0.50 kg of the robot's total weight. An additional 4 Watts was factored into the systems overall power requirement to account for the power consumption of on-board radios and losses due to voltage regulation, etc. A battery pack consisting of four parallel LIPO batteries was chosen to accommodate the total power requirements of all payloads (approximately 20 Watts), along with an additional 150 Watts predicted to be consumed by the robot's legs, so that the system could run for more than 30 minutes under normal operating conditions.

It was decided that each leg of the BlueFoot platform would have four degrees of freedom (*i.e.*, 4 servo actuators) so as to facilitate high overall dexterity for all-terrain navigation and a highly posable trunk. Having more actuators in series per leg meant that the robot's legs would be longer. As a result, the link lengths of each leg had to be smaller so as to minimize the static/dynamic torques which would be applied to each joint during gaiting. Thus, a compact bracketing system was selected for composing each legs. A commercially available servo-motor was then chosen to actuate each leg joint. The resulting leg configuration was estimated to yield approximately 2.5 kg of carrying capacity, making it adequate for supporting BlueFoot's 2 kg of on-board payloads (including the mass of the batteries) and an additional 0.1 kg contributed by its structural elements.

This chapter will outline the specifics of BlueFoot's implementation, resulting from the aforementioned design process, starting with the structural layout of the system. Next, major system payloads and the associated interfacing of major devices will be described. This section which will include details about BlueFoot's actuators, compu-

tational modules, and sensory mechanisms. Lastly, the system power routing, energy requirements, and runtime will be detailed.

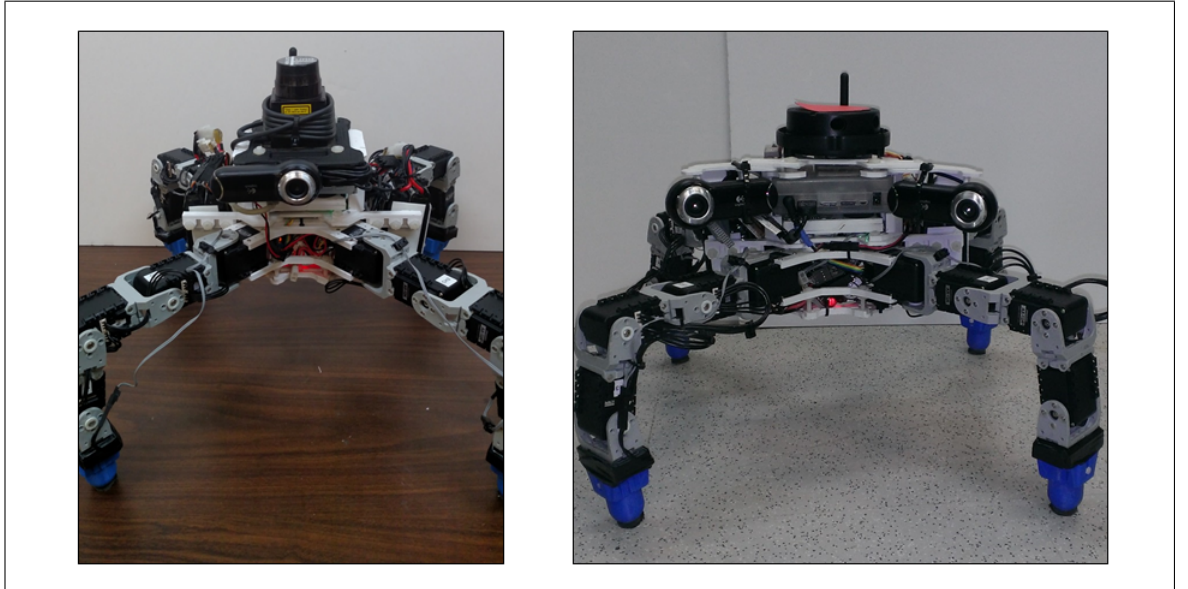


Figure 3: The BlueFoot Quadruped Robot: single-camera configuration (*left*); stereo-camera configuration (*right*).

## 2.2 Robot Structure

BlueFoot’s body is designed in a modular fashion and is comprised of mostly custom designed, 3D printed parts. The use of 3D printing as a fabrication method allowed for rapid design iterations in the early stages of system prototyping, and has kept the weight of the robot’s overall structure relatively low. Parts were mainly printed from both PLA and SLA plastics. BlueFoot’s overall weight (when fully outfitted) is 1.85 – 1.98 kg, depending on configuration.

The modularity of BlueFoot’s overall structure arises from the inherent design requirements associated with 3D printing and general design practices aimed at keeping the system reconfigurable for the incorporation of updated sensory and computational hardware. Moreover, parts are designed to fit future replacements while conforming to the constraints imposed by the 3D printing fabrication method, *i.e.*, particular part size and orientation requirements. Such constraints had to be met by each designed part to ensure print feasibility.

The BlueFoot platform has undergone several minor redesign phases since its inception. These redesigns were necessary to bring the BlueFoot platform to its final

structural and hardware state and were performed to accommodate changes in sensory/computational hardware. The sections that follow will mainly focus BlueFoot's final hardware configurations.

### 2.2.1 Main Body (Trunk) Design

BlueFoot's trunk consists of the three main sections: a lower module which interfaces the legs with the main body; a center chassis, designed to hold computational and battery payloads; and a top platform, which interfaces the system's vision sensors to the trunk. These sections will be referred to as the *Root* module, the *Main* module, and the *Head* module, respectively. The full trunk (not including sensor dimensions) fits within a 21.6 by 21.6 by 15.3 cm bounding box.

#### The Root Module

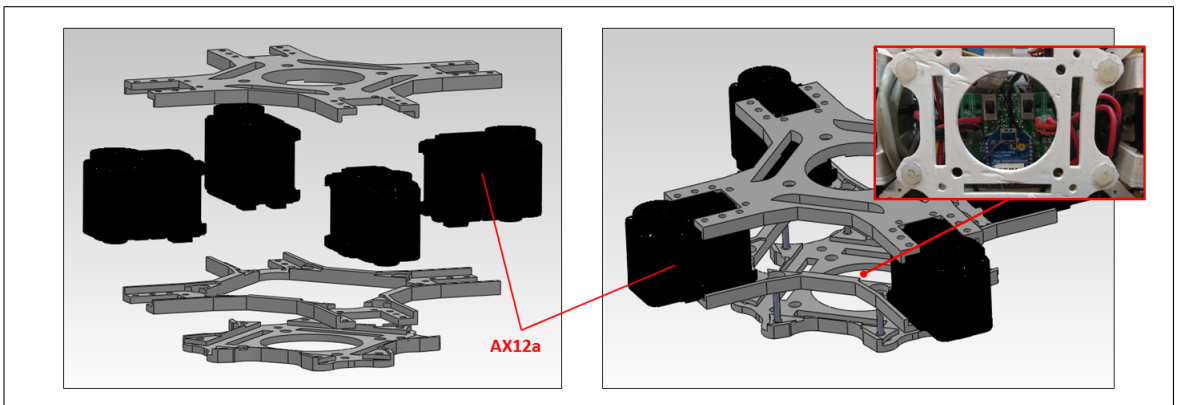


Figure 4: Root section of trunk. Call-out in top-right shows main-switch access through the bottom of the root module.

The Root module, consists of three plates, as shown in Figure 4. Each plate is designed with a central opening to allow for wired connections to pass to other trunk modules. Two such plates directly interface with four servos, which are mounted to four symmetric arms which extend from the center of each plate. These servos are the first joint (hip-joint) of each leg. Each servo mounts to the top a bottom plates via mounting holes located at the top and underside of each servo chassis. The assembly is mated with small steel bolts. A third, smaller plate is attached to the bottom of the module to provide more space for power components and associated wiring. This plate is attached to the bottom of the module via plastic standoffs. An opening in the middle

of this plate provides access to the system's main power switches, as well as a removable XBEE wireless radio unit.

## The Main Module

The Main module of BlueFoot's trunk includes compartments for an in-house designed AutoPilot unit and a main computer unit, an ODROID-XU. The Main module is designed such that the AutoPilot and ODROID-XU computer slide in and out of the body. The computer payloads are locked into position when the Head module is added to the assembly. The Main body section is designed to fit both computers when stacked upon one another, as depicted in Figure 5. The computer stack is positioned directly in the center of the module when inserted.

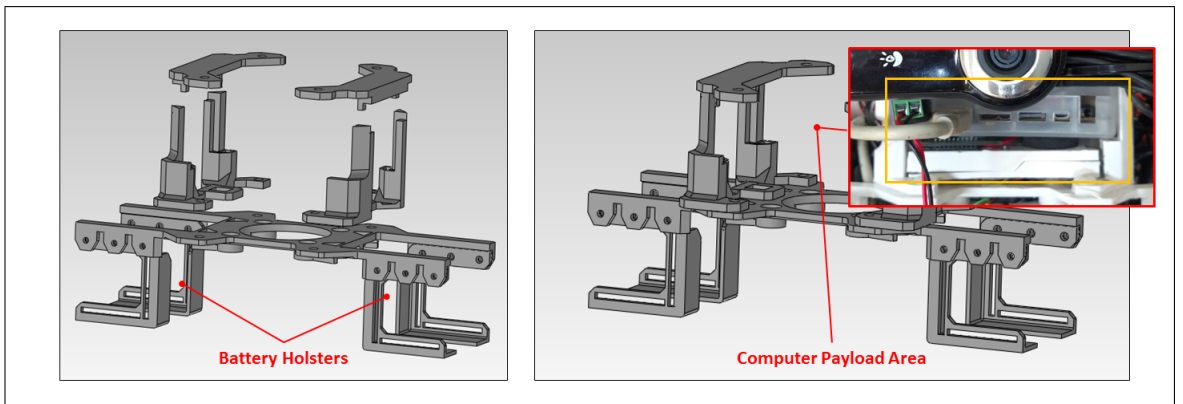


Figure 5: Main section of trunk. Call-out in the top-right shows how the ODROID-XU and AutoPilot computers fit within the module.

The Main module also includes two battery holsters, which hang over its left and right sides. The holsters align the battery packs with the center of Root module. This battery placement serves to lower the center of mass (COM) of the trunk. Doing so serves to lower the magnitude of dynamic torques imparted upon the leg servos during gaiting by decreasing the net moment due to gravity imparted upon the system when the body is oriented away from the direction of gravitational force. The entirety of the Main module is attached to the Root module through the battery holster sub-assembly by four plastic bolts.

## The Head Module

Two separate Head modules have been designed for the BlueFoot system : one of which features a stereo camera pair and a Piccolo LIDAR sensor (PLDS); and a

monocular design, which features a camera and a Hokuyo-URG LIDAR sensor, as shown in Figure 6. Each head module is attached to Main module via four plastic mounting screws. In the stereo-camera design, two adjustable wings are attached to either side of a top platform which hold cameras. These wings were designed to be adjustable to aid in stereo-camera configuration and calibration. The position of each camera on the trunk allows for a persistent field of view by each camera during mobilization. The PLDS unit is positioned such that the center of its rotating laser head is aligned to the center of the trunk.

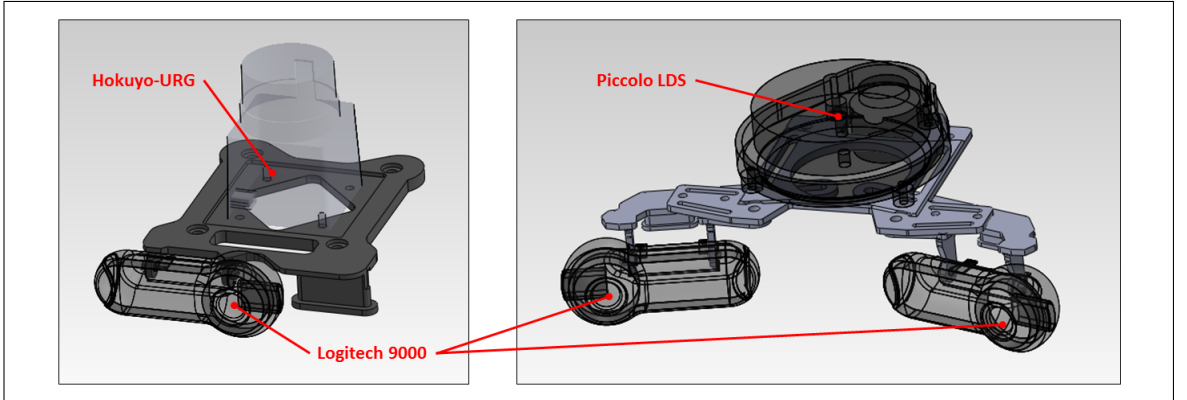


Figure 6: Head section of trunk. Monocular camera configuration with Hokuyo-URG (*left*); and Stereo configuration with PLDS (*right*).

In the monocular design, a single camera is mounted such that the lens of the camera is aligned to the sagittal plane of the trunk. This configuration is currently being used as BlueFoot’s *primary* head configuration and is mainly being used for 3D point-cloud building and surface reconstruction via 2D LIDAR scans. This is because the Hokuyo-URG laser scanner used in this configuration offers higher-resolution laser-scan outputs, which will be covered in more detail later in this chapter.

### 2.2.2 Leg Designs

Each of BlueFoot’s legs are identical and are comprised of four Dynamixel AX12a smart-servo actuators (see Figure 7). These actuators are connected via dedicated Dynamixel mounting brackets. Feet are attached to the ends of each leg which contain an embedded, two-state contact sensors. Each foot is designed with a spherical tip, which is rubberized to provide extra grip. The ankle joint of the platform has been added such that the platform can reconfigure its foot orientation while retaining a constant

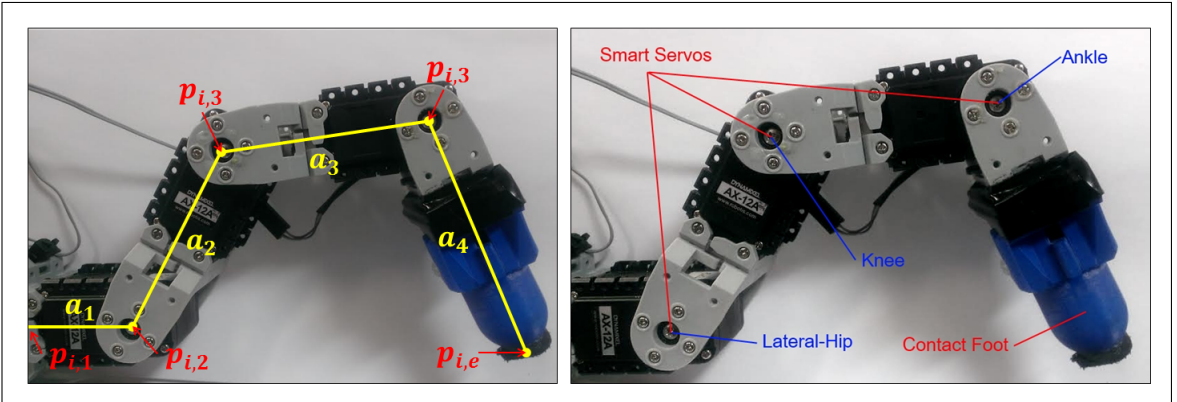


Figure 7: Closeup of BlueFoot’s leg. (*left*) shows effective link lengths and the location of defined joint positions.

spatial position during gaiting. Additionally, this configuration allows for a considerable amount of independent body re-orientation and repositioning. This capability extends itself to the stabilization and gimbalizing of vision sensors mounted on the upper body of the platform while the platform is in motion.

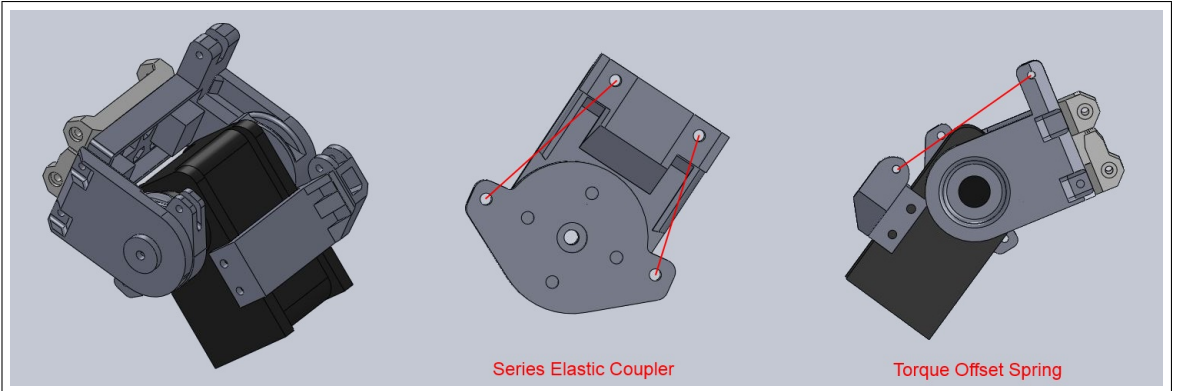


Figure 8: Series elastic brackets.

Though not kept in the system’s final design, some experimentation was performed with the incorporation of series elastic joints, which were designed to relieve joint impact during gaiting. Series elastic actuation was achieved by replacing bracket interfacing the first and second hip joints of each leg with an elastic-compliant mounting bracket. This bracket includes spring loaded member which was mounted to the horn of the second hip servo on each leg, as shown in Figure 8 and allowed the leg to deflect a small amount at the lateral hip (second joint).

Link lengths,  $a_1, a_2, a_3$  and  $a_4$ ; and offset from the center for the Root module to

the first joint of each leg,  $\nu$ , are defined in Table 1. These parameters are identical for each leg, and are corresponded with physical leg members labeled in Figure 7.

| Link  | Length, m |
|-------|-----------|
| $a_1$ | 0.06500   |
| $a_2$ | 0.06500   |
| $a_3$ | 0.06500   |
| $a_4$ | 0.06500   |
| $\nu$ | 0.09215   |

Table 1: Link and body-offset lengths for each leg.

### 2.3 Computational and Sensory Hardware

Major payloads on-board the BlueFoot robot are as follows:

- Dual processor AutoPilot unit with a 12-axis inertial measurement unit
- ODROID-XU Computer
- Logitech 9000 Web-cameras
- Hokuyo-URG / Piccolo LIDAR Units (configuration dependent)
- Two-state foot contact sensors (x4)
- Dynamixel AX12a Smart Serial Servos (x16)
- XBEE Wireless radio

Device selection has remained mostly consistent since the platform’s inception and initial design, with the exception of computing its main computing units. The AutoPilot unit was updated from an older model, and the ODROID-XU computer replaced a Beaglebone computer for the sake of improving overall computing power.

### 2.3.1 Device Descriptions

#### AutoPilot

A dual processor AutoPilot unit performs BlueFoot’s low-level gaiting and actuator control tasks, as well as handles communications with a computer running ground-station software. Given the set of low-level sensory and motor-handling tasks it performs, this module has been named the the “Lower Brain” (LB) of the system. The AutoPilot consists of two processing units: a TM4C and RM48 micro-controller (MCU), which operate at 80 MHz and 220 MHz, respectively. These processors communicate over a single UART line, which is used to transfer packeted data between the two processors using a unified inter-processor data transfer protocol, EXI. This protocol which will be described later in more detail. One UART of the RM48 MCU is also connected to an on-board computer, an ODROID-XU, through a USB-to-serial connection. The AutoPilot is powered via an external 12 V supply.

This AutoPilot unit includes a 12-axis inertial measurement unit (IMU) which consists of two, 3-axis accelerometers; one 3-axis rate gyro; and a 3-axis magnetometer unit. This sensor is used for acquiring angular rate data of BlueFoot’s trunk and estimating of trunk orientation states using an Extended Kalman Filter (EKF).

#### ODROID-XU

An ODROID-XU performs many of system’s high-level planning tasks, such as navigation, image processing and terrain reconstruction; and handles data data acquisition from both camera and LIDAR sensor units. Given that this unit performs mostly high-level planning tasks, it has been given the name “Upper Brain” (UB). This computer contains a 1.6 GHz, quad-core processor with 2 Gb of RAM. The ODROID-XU can be communicated with over WiFi via a USB WiFi antenna. Currently, SSH tunneling is used to start processes on the ODROID remotely and stream data. The ODROID-XU is powered via an external 5V connection.

#### Logitech 9000 Web Cameras

Logitech 9000 web cameras have been selected for creating a stereo camera pair, as well as for use in a single camera configuration. These cameras are high-definition web cameras and have a maximum frame rate of 30 fps and a max resolution of 1280 by 720. Cameras are currently read at a the max rate of 30 fps at a more conservative resolution of 640 by 480. These settings are adequate for image processing tasks and have been

chosen to reduce nominal data throughput. These cameras are interfaced with the UB (OROID-XU) over a USB connection.

### Laser Distance Sensors (PLDS and Hokuyo-URG)

The Piccolo Laser distance sensor (PLDS), which is used in BlueFoot's stereo-camera type configuration, is a 4 meter spinning-head laser range finder. The PLDS has a resolution of a point per degree and covers a range of 360 degrees. Ranging frames (which covers a full rotation) are acquired at a rate of 5 Hz, and are dispatched over a serial connection at 115200 baud. An FTDI break-out board is used to convert the sensor's raw serial output to USB protocol so that the sensor can be interfaced with the UB unit. The PLDS is powered via an external power 5 V source, which is regulated to a 3.3 V voltage level for powering the motor which spins the laser head, and 1.8 V for internal logic. Regulation is performed by an auxiliary power circuit.

The Hokuyo-URG Laser Distance sensor, which is used in BlueFoot's single-camera head configuration, has a range of 5.6 meters and an angular resolution of 0.38 degrees per point (628 points per scan). This scanner covers a total angular range of 240 degrees. Ranging frames are acquired at a rate of approximately 10 Hz and dispatched directly over a USB connection at 115200 baud. The unit is powered directly over USB.

### Foot Contact Sensors

Binary-state contact sensors are embedded in each foot. These contact sensors are essentially limit-switches which generate an active-low signal when the foot comes in contact with the ground. Each sensor is connected to ground and a GPIO pin on the TM4C MCU of the AutoPilot. A  $500\ \Omega$  is added in series with the limit-switch for the purpose of pin protection.

### Dynamixel AX12a Smart Serial Servos

BlueFoot uses 16 Dynamixel AX12a servo units (4 per leg). These servos are position-controlled and commanded over a daisy-chained, half-duplex serial bus (i.e. single wire) at a rate of 1 Mbps. These servos have a maximum holding torque of 1.618 N m and top speed of 306 degrees/s. The AX12s provide position, velocity and loading feedback, however velocity feedback is not used. Servo velocities are, instead, estimated in real time from position feedback because velocity readings provided by the AX12 is relatively noisy by comparison.

Commands are sent to the servos via an aggregate command packet which contains goal-position values for all servo units. Feedback is collected from each servo using individual data-request packets. Servos respond to each request with a response packet containing a corresponding feedback value. Given the number of servos in the network; communication overhead; and the one-wire communication configuration, servo updates are limited to a maximum update rate of 50 Hz over a half-duplex communication line. Gathering feedback over the half-duplex communication bus is particularly expensive because feedback requests require that the host processor wait after each dispatched for a response from each targeted servo. Moreover, each request/response cycle must finish to completion before a feedback request is made to another servo on the communication bus.

A dedicated circuit has been designed for use with these servos which converts a full-duplex serial line to a half-duplex AX12 bus. The circuit uses a two-state tri-state buffer which is switched via a general-purpose I/O line. This switching circuit is integrated into the system's main power switching and distribution board. Each servo is powered via an fused, software-switched 12 V supply line.

## XBEE Wireless Radio

An XBEE Wireless Radio, shown in Figure This could be the picture from before, is used for communication between the LB and an external computer ground-station. The radio is interfaced with the LB via 57600 baud serial connection. This radio has a range of outdoor range of 27 meters and a maximum one-way transfer-rate of 115200 bps. Transfer rates between the LB and ground station are currently being limited to 57600 bps to compensate for a lack of hardware flow-control, which is required for stable, two-way communication between two XBEE radios at maximum communication rates. However, the selected communication rate is more than adequate for transferring necessary control information to and from the system without the need for additional flow-control hardware.

This wireless endpoint is used currently used interchangeably with the ODROID-XU's wireless WiFi radio, but will soon be retired to simplify hardware design and increase the platform's data streaming capabilities by switching to a WiFi-based line of communication. Ground station software, as well as the system's internal command-routing and networking software, is designed in such a way to easily accommodate this change.

### 2.3.2 Device Networking

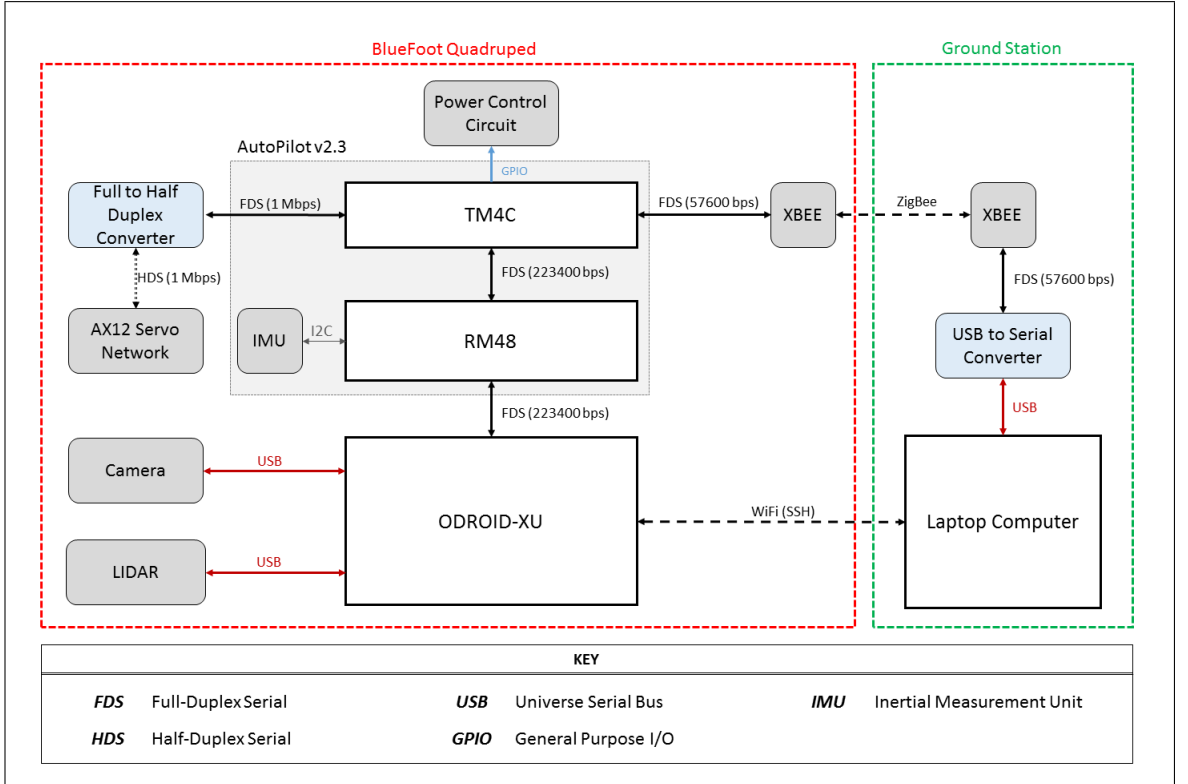


Figure 9: BlueFoot device networking diagram.

Figure 10 depicts how each major device is connected within the system and details the communication rates ( $f_{com}$ ) between networked devices. Accompanying specifications are detailed in Table 2, which summarizes all device communication pairs and their corresponding baud rates.

XBEE\* refers to the on-board XBEE module which communicates with the ground station.

| Port <sub>A</sub> | Source <sub>A</sub> | Port <sub>B</sub> | Source <sub>B</sub> | $f_{com}$ , kbps |
|-------------------|---------------------|-------------------|---------------------|------------------|
| UART0             | TM4C                | DIN/DOUT          | XBEE*               | 55.7             |
| UART2             | TM4C                | DIN+              | AX12 Net.           | 1000             |
| UART1             | TM4C                | LINSCI            | RM48                | 223.4            |
| SCI               | RM48                | USB (FTDI)        | ODROID-XU           | 223.4            |
| USB               | ODROID-XU           | DIN/DOUT          | LIDAR               | 115.2            |
| USB               | ODROID-XU           | USB               | Cameras             | No Spec.         |

Table 2: System communication port-pairs and corresponding data transfer rates

## 2.4 System Power

### 2.4.1 Power Routing

System power routing is handled via an integrated power switching and distribution board. This board includes physical, main power switches which connects external power to two main, internal 12 volt buses for computer power (Net-1) and motor power (Net-2), respectively. The board also regulates system input voltage to a 5 V bus for use with on-board ICs and 3.3 V bus for powering the XBEE radio. Regulated power and power the servo motors of each leg controlled via three, two-channel power-switching IC's, which are toggled using six digital I/O pins on the TM4C processor of the LB. These power-switching chips allow for software-controlled power configuration, and further, software controlled emergency power cutoff to the servo motors. System main power is supplied via four 12 V (3 cell), 2 Ah Lithium Polymer battery packs.

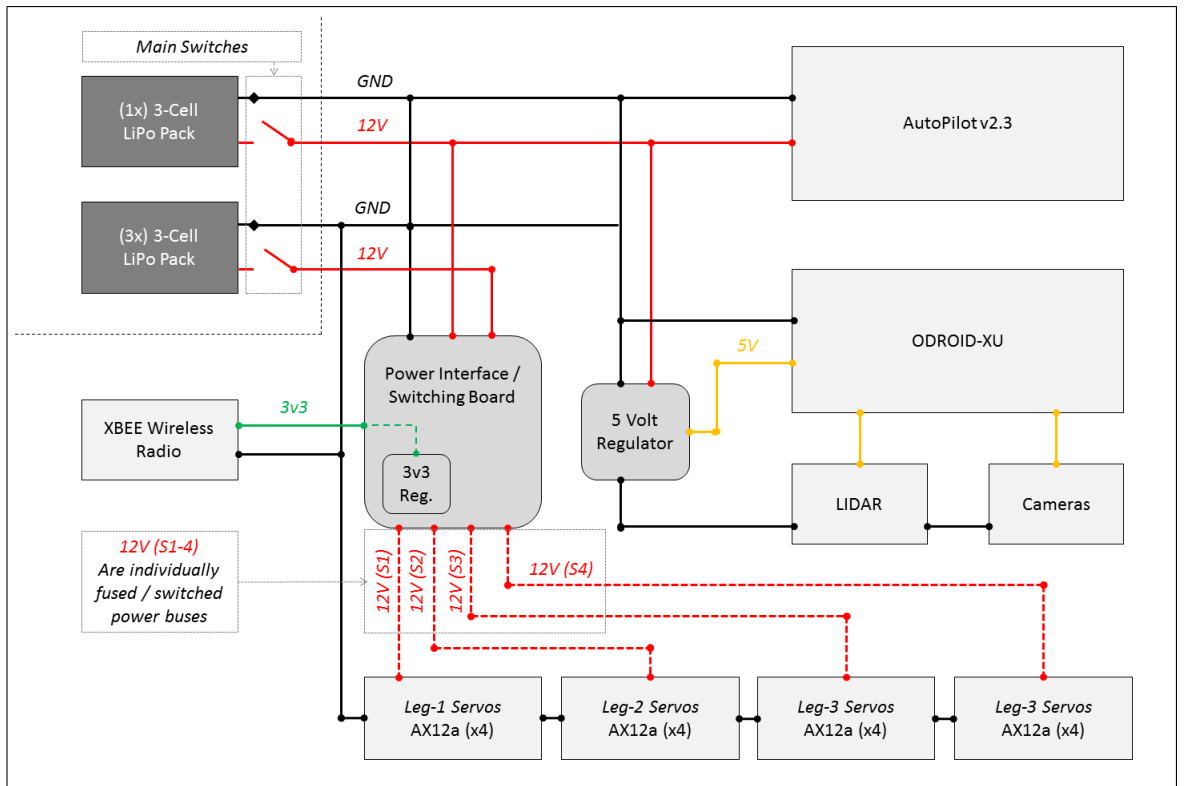


Figure 10: BlueFoot power routing.

### 2.4.2 Energy Requirements and Runtime

The power consumptions of BlueFoot’s component device’s are summarized in Table 3, which provides the operating voltage,  $V_{op}$ , and nominal current draw,  $I_{nom}$ , of each active, on-board component. Table 4 details battery specifications (output voltage and amp-hour rating) and BlueFoot’s estimated run-time under nominal operating conditions.

| Net                                 | Device                 | $V_{op}, V$         | $I_{nom}, A$   |
|-------------------------------------|------------------------|---------------------|----------------|
| 1                                   | AutoPilot (RM48, TM4C) | 12.0                | 0.40           |
| 1                                   | XBEE Radio             | 3.3                 | 0.25           |
| 1                                   | ODROID-XU              | 5.0                 | 2.0            |
| 1                                   | Logitech-9000          | 5.0                 | 0.1            |
| 1                                   | Hokuyo-URG             | 5.0                 | 0.5            |
| 2                                   | AX12a Servos (x16)     | 12.0                | 9.6 ( 0.6 ea.) |
| <b>Total Power Consumption</b>      |                        | 137.8250 W          |                |
| <b>Worst-Case Power Consumption</b> |                        | $\approx$ 200.000 W |                |

Table 3: Power consumption summary by device (for single-camera configuration).

| Net                       | Battery Pack      | $V_{out}, V$         | Rating, A.hr |
|---------------------------|-------------------|----------------------|--------------|
| 1                         | 3S LiPo Pack (x1) | 12.0                 | 2.0          |
| 2                         | 3S LiPo Pack (x3) | 12.0                 | 6.0          |
| <b>Average Runtime</b>    |                   | $\approx$ 41 minutes |              |
| <b>Worst-Case Runtime</b> |                   | $\approx$ 28 minutes |              |

Table 4: Battery power supply and estimated runtime summary.

## CHAPTER III

### Software

#### 3.1 System Software Architecture

BlueFoot is controlled using a multi-processor software architecture which incorporates several independent core programs. Each of these programs handles portions of system control in a cooperative fashion. Core programs are executed on physically separate operating units, allowing for low-level tasks, such as actuator command and feedback handling, battery monitoring, etc., to be decoupled from more computationally heavy tasks, such as high-level planning and navigation. With task-decoupling in mind, BlueFoot's software architecture is designed such that core programs could be readily offloaded to physically separate computing modules. Each of these control modules handles their own set of assigned tasks in independent control loops. Information is forwarded from each independent processor to update the overall BlueFoot software macro-system in an asynchronous fashion. System control tasks essential to BlueFoot's overall operation are divided into four main categories, which can be summarized as follows:

- *Low-Level Control* : power monitoring / switching, actuator command handling, communications routing, sensor data acquisition, script parsing and evaluation
- *Locomotion Control* : gait planning, gait adaptation, trunk pose adaptation
- *High-Level Control* : perception, motion planning, surface reconstruction, navigation, localization
- *Human-Operator Control* : joystick/keyboard commands, scripting commands

Low-level and locomotion control tasks are handled, exclusively, by the *Lower Brain* (LB), which designates a collection of software spanning over the RM48 and TM4C processors of the AutoPilot. High-level control tasks are handled by the Upper Brain (UB), which is a collection of software which runs on the ODROID-XU module. Lastly,

a human operator can interface with the BlueFoot robot wirelessly from a personal computer running ground-station software. The ground station communicates with the BlueFoot robot over wireless communication lines routed to the TM4C processor and the ODROID-XU computer. The ground-station interfaces with the ODROID-XU over an SSH connection. This wireless tunnel connection is mainly used for configuring runtime settings and collecting data stored on-board the robot.

Since this software architecture is distributed over several separate computational units, an integral part of this control architecture is an efficient, reconfigurable inter-processor communication protocol. Namely, interprocessor communication on board BlueFoot is performed using data packets transferred over serial lines. These data packets are formatted using an in-house designed binary-XML protocol, called EXI. This protocol facilitates a highly customizable packeting structure for asynchronous inter-module communication and utilizes robust packet-error checking routines. This section will detail BlueFoot’s interprocessor communication protocol, namely the composition of packets transferred between processor.

This section will also detail the specific software-level tasks handled by each of BlueFoot’s processor; the speed at which each core software element is run (update frequency); and what data must be communicated between individual software nodes during operation. Additionally, this section will describe the ground-station software and corresponding user-interface used to control the BlueFoot Quadruped and administer high-level commands.

### 3.1.1 System Task Allocation

Figure 11 depicts how core software and associated control elements are related within the BlueFoot software macro-system. This section will detail the tasks carried out by each major software module implemented on the BlueFoot quadruped.

#### TM4C (Lower Brain)

As previously mentioned, the TM4C processor on-board the AutoPilot module is responsible for a majority of the systems *Low-Level* tasks and can be viewed as a safety / communications routing co-processor. Within its main program loop, the TM4C polls the system’s main battery voltage via an ADC interface; handles communication (packet decoding) routines between the ground-station and the RM48 system nodes; and handles command dispatching and feedback polling with the system’s 16 servo actuators. The

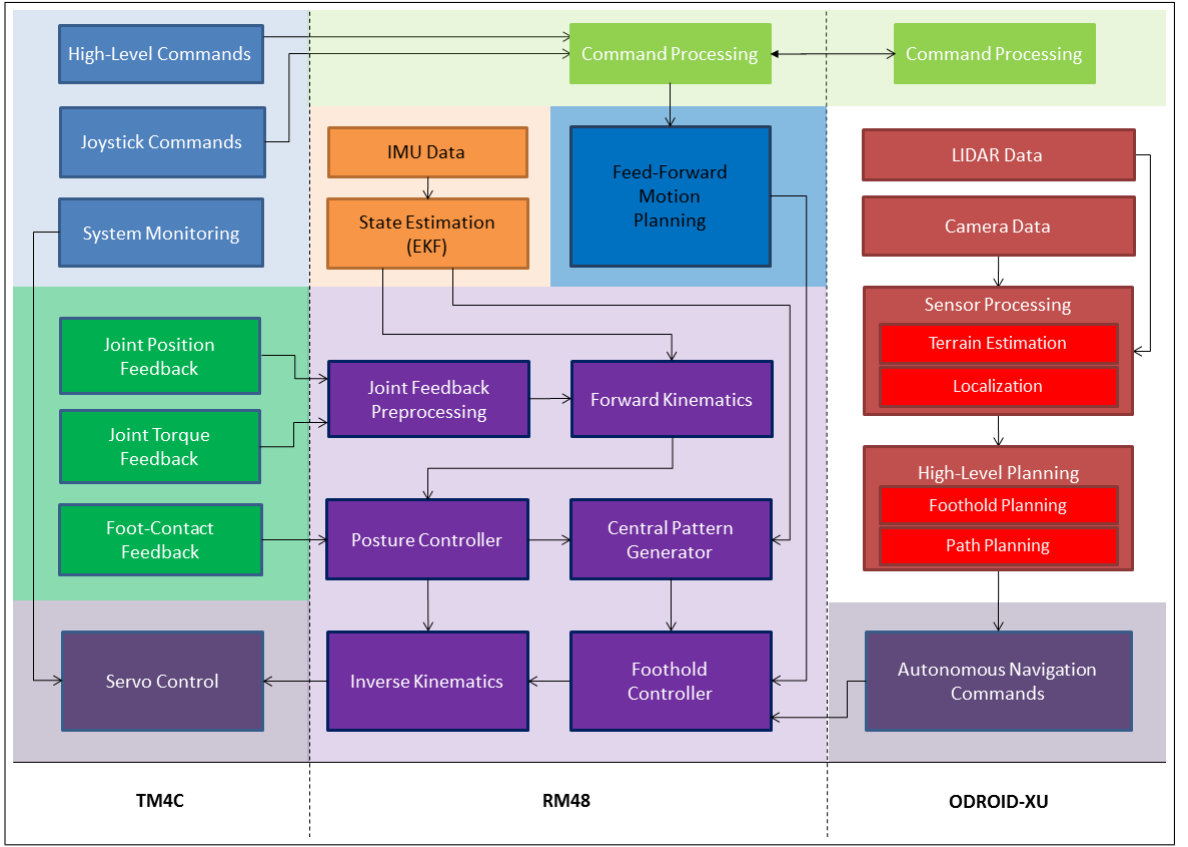


Figure 11: BlueFoot’s on-board processes / signals and their relationships.

TM4C is directly interfaced with two dual-channel power switching IC’s and is used to control the supply of power to each leg. Power is controlled by toggling general purpose IO pins in software. The state of these pins is administered as part of a periodic packet command / update packet sent from the ground-station. Since the TM4C has this control over the system’s actuators (which consume most of the system’s power) and battery monitoring capabilities, it runs a safety routine which is responsible for halting motor activity and cutting system power on low-battery or power-fault conditions, as well as during unexpected breaks in communication with the ground-station.

As previously mentioned, the TM4C handles communication routing between system processing modules; as well as with the controllers on-board each smart-servo. Administering servo commands and collecting servo feedback is the TM4C’s highest priority task. This process, which involves both commanding and requesting feedback from each servo, is relatively expensive and limits the TM4C’s main-loop frequency to roughly 50 Hz. Thus, it is particularly important that this task is offloaded to this processor. Other safety and communication-related tasks are much less expensive, by

comparison, and allow the servo actuators to be updated quickly as possible without encumbering other system control operations.

### RM48 (Lower Brain)

The RM48 is responsible for several *Low-Level* tasks, including IMU polling and handling communication with the TM4C and ODROID-XU. Each set of collected IMU data is passed along to an Extended Kalman Filter (EKF) routine, which is used to estimate that orientation of the BlueFoot’s trunk.

The RM48’s primary function is to carry out motion control and gait-planning tasks. To achieve this, the RM48 handles a state machine which switches between planned motion execution and trajectory control; and a Central Pattern Generator (CPG) based gaiting controller, which will be discussed in more detail in Chapter V. Additional functions for body and posture (position and orientation) control, including trunk control procedures and gait-stabilization routines are run in tandem with the aforementioned gait-control task.

Motion and gait controls, which are performed in the robot task-space, are converted into joint-space reference angles,  $q^r$ , via an inverse kinematics (IK) routine. The IK routine is executed at all times when the legs are engaged for the purpose of issuing servo position commands. The RM48 also maintains BlueFoot’s forward kinematic model, which is used to estimate the position of each foot relative to the trunk. This model relies on the EKF-generated trunk orientation estimate,  $\hat{\theta}_b$ , and joint position feedback,  $q$ . BlueFoot’s inverse and forward kinematics models will be detailed in Chapter IV. The RM48 runs its full control loop at approximatively 100 Hz (twice the speed of the TM4C control loop) to facilitate higher integration stability when updating gait related controller dynamics, dynamic motion controls, and task-space reference trajectories.

Lastly, the RM48 handles an on-board scripting engine (based on the MIT Squirrel scripting language), which interprets lexical commands. This scripting engine is capable of handling a large number of high-level commands and is complex enough to handle function and class definitions in real time [47]. The scripting engine is currently being used to evaluate BlueFoot’s core user-command set, ranging from simple state toggling and parameter modification, to the prescription of user-specified way-points for navigation, among other high-level command items. Scripting commands are passed from the ground station, via a text-input terminal, and routed through the TM4C to the RM48 where they are finally evaluated.

## **ODROID-XU (Upper Brain)**

The ODROID-XU runs software upon the Debian (Linux) operating system distribution “Jessie.” The use of an Linux operating system extends itself to a number of conveniences, such as to ability to run several tasks in parallel threads. Inbuilt USB-serial drivers are used to acquire data from USB-interfaced vision sensors. Namely, the ORDOID handles the acquisition of camera data and controlling camera frame-rate; as well as the acquisition of LIDAR data. The OROID uses these sensor inputs to perform several navigation-related tasks. These tasks will be described in more detail in Chapter VI.

The ODROID-XU utilizes 2D-LIDAR scans (frames) and trunk-pose estimates to form organized 3D point clouds. These point-clouds are further processed to reconstruct 3D terrain surfaces and height-maps, which are then used for step-planning. LIDAR and camera data is utilized in a potential fields-based navigation routine. Image processing and image feature detection runs as a separate process on the ODROID. In particular, the open-source libraries OpenCV (Open Computer Vision Library), OpenPCL (Open Point-Cloud Library), and Boost are used heavily in the software developed to carry out the aforementioned tasks [45, 48, 49]. Collectively, software written for this platform was generated using a mixture of C++ and Python.

As previously mentioned, the ODROID-XU can handle a limited set user-commands on its own, which are administered directly to the ODROID-XU from an SSH terminal on the ground-station computer. These commands include core-program start-ups and runtime configurators. Essentially, the ODROID’s software core is designed as a completely independent software module which replaces the roll of a human director, as it handles the bulk of the systems high-level planning and navigation tasks. Moreover, if the ODROID-XU is removed from the BlueFoot system, the system can still be operated via remote-control heading commands provided from human operator using BlueFoot’s ground-station joystick control inputs.

### **3.1.2 Inter-processor Communication**

This section will detail the contents of the data packets transferred between processors, which is summarized in Figure 12. System directives, generated by a human operator who interacts with the robot via a graphical user interface and joystick controller, originate from a ground-station computer. Update packets which are sent from the ground-station to the BlueFoot robot (TM4C) are composed as shown in Table 5:

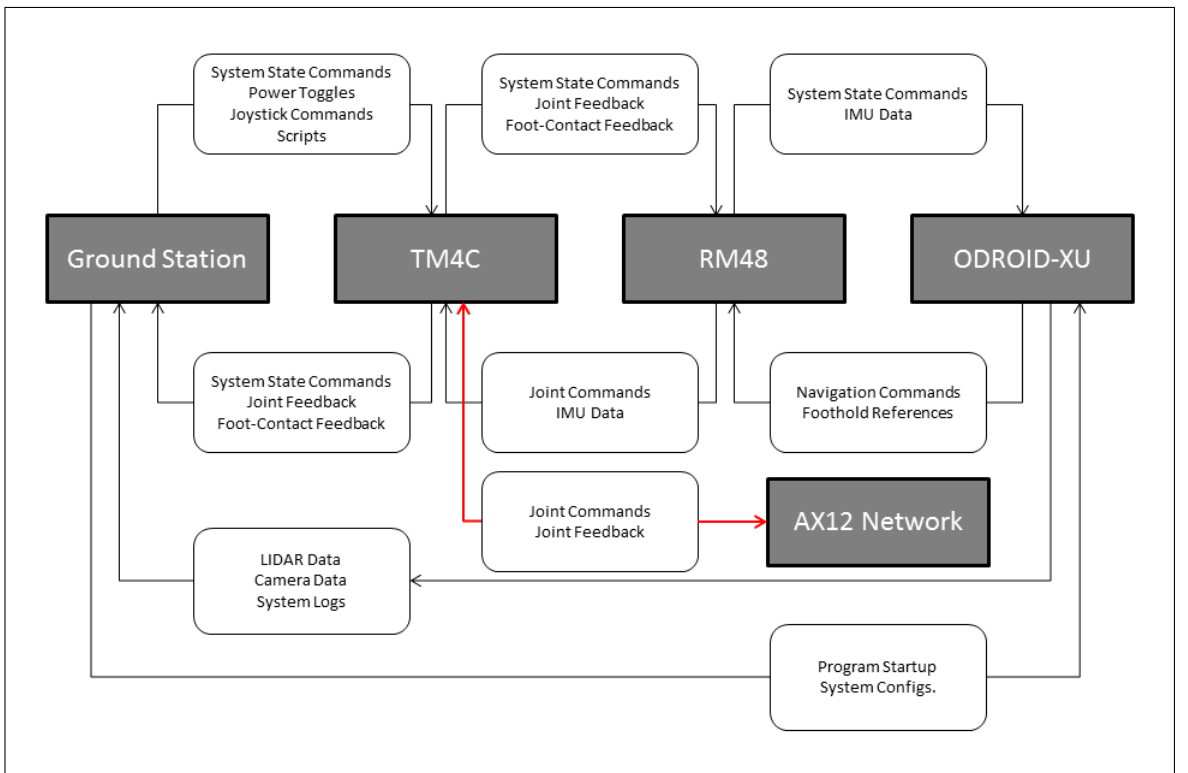


Figure 12: Communication flow between processors on the BlueFoot Platform.

| <i>32-bits</i>  | <i>8-bits</i> | <i>8-bits</i> | <i>16-bits</i> | <i>16-bits</i> |
|-----------------|---------------|---------------|----------------|----------------|
| HEADER          | Master-Tog.   | Power-Tog.    | Unused         | Network Info   |
| <i>Variable</i> |               |               |                |                |
| Scripts         |               |               |                |                |

Table 5: Structure of the packets sent from Ground-Station to TM4C.

Every packet issued has a 4-byte (32-bit) header, which is added as part of the EXI protocol. As part of the internal system protocol, every packet contains a “Master Status Vector”, which is comprised of a fixed length, 7-byte sequence of essential system information and control states. The “Master Toggles” section (first 8-bits after header) enumerates major systems states, including *On-line*, *Standby*, *Off-line* and *Suspended* system state designations. The next 8-bits are used to toggle on-board power, namely the power supplied to each leg. The remaining 32-bits are used for specifying battery voltage (8-bits), power-fault states (8-bits); generic binary feedback toggles (8-bits) used to store foot contact information; and system networking information (16-bits). The last section of this packet contains scripting commands, which vary in length. Forward velocity and

turning rate commands (gathered from a joy-stick control input) are administered in the form of scripted commands.

Packets sent from the TM4C to the Ground-station contain status items which are maintained on-board the robot, and appear as shown in Table 6: The *Joint Pos.*

| <i>32-bits</i>   | <i>8-bits</i> | <i>8-bits</i> | <i>8-bits</i> | <i>16-bits</i> |
|------------------|---------------|---------------|---------------|----------------|
| HEADER           | Master-Tog.   | Unused        | Foot-Contacts | Network Info   |
| <i>2048-bits</i> |               |               |               |                |
| Joint Pos. FB    |               |               |               |                |

Table 6: Structure of the packets sent from the TM4C to the Ground-Station.

*FB* (joint position feedback) element is composed of 32-bytes corresponding to the joint position feedback from each actuator. To avoid redundancy, the structure of the packets communicated from the TM4C to the RM48 and vice-versa will not be depicted explicitly. These packets contain a 7-byte master status vector with only the *Master-Toggle* and *Network Info* fields populated. The TM4C sends the same joint feedback information to the RM48 as it does the Ground Station. For packets sent from the TM4C to the RM48, this field is replaced by a 32-byte sequence of joint-position commands.

Packets sent from the RM48 to the ODROID-XU contain additional fields which contain dynamical-state information used in planning on the ODROID. State information is sent in the form of vectors with single precision floating-point (32-bit) elements. Such information includes trunk orientation estimates, angular rate, and global position (generated from open-loop command integration); and four foot-position estimates, each of which are represented as a separate 3-element vectors. These packets have a structure which is depicted in Table 7. Packets sent from the ODROID-XU to the RM48 contain

| <i>32-bits</i> | <i>8-bits</i>  | <i>8-bits</i>   | <i>8-bits</i>   | <i>16-bits</i> |
|----------------|----------------|-----------------|-----------------|----------------|
| HEADER         | Master-Tog.    | Unused          | Foot-Contacts   | Network Info   |
| <i>96-bits</i> | <i>96-bits</i> | <i>328-bits</i> | <i>328-bits</i> |                |
| Orientation    | Angular Rate   | Trunk Pos.      | Foot Positions  |                |

Table 7: Structure of the packets sent from the RM48 to the ODROID.

command items, such as forward velocity, turning rate and trunk-pose commands, as

well as foothold-references and corrected global trunk position estimates. These packets are constructed as shown in Table 8 :

| <i>32-bits</i> | <i>8-bits</i>  | <i>8-bits</i>  | <i>8-bits</i>   | <i>16-bits</i> |
|----------------|----------------|----------------|-----------------|----------------|
| HEADER         | Master-Tog.    | Unused         | Unused          | Network Info   |
| <i>32-bits</i> | <i>32-bits</i> | <i>96-bits</i> | <i>328-bits</i> | <i>96-bits</i> |
| Velocity       | Turning Rate   | Trunk Pose     | Footholds.      | Trunk Pos.     |

Table 8: Structure of the packets sent from the ODROID-XU to the RM48.

### 3.2 Ground Station

Ground-station software used for controlling the BlueFoot platform is written in C++ using an open-source graphical user interface design library called *wxWidgets* [50]. *wxWidgets* is used, primarily, for the ground-station’s front-end design. Namely, the ground-station code is designed such that its UI design is reconfigurable. This is made possible by an XML-based design configurator, which can be used to change the look and location of buttons and panels which make up the UI, without having to modify the ground-station back-end software.

The back-end portion of the ground-station software handles interrupts generated by user inputs, such as button presses and text input. *wxWidgets* make the process of associating functional callbacks to use input events relatively easy. Additionally, *wxWidgets* provides an interface for collecting joystick inputs, which are interpreted and sent to the BlueFoot as scripting commands. *Boost*, a C++ utility library, is utilized to handle socket and serial-port IO controls. This library is particularly important handling serial-IO ports on the ground station computer, which are used in communicating with the robot over a wireless radio connection.

The ground station is composed of several main sections of UI which provide interfaces for administering system master-state, operating-state and power toggling; providing system commands; and scripting. Ground station commands are sent to the robot in order to modify operating states and administer manual navigation commands. Updates from the ground-station are sent to the platform rate of 25 Hz using the XBEE radio module. BlueFoot replies to each ground-station update with a packet of internal configurations, as shown in Table 6, which is then used to check that system updates and commands have been received and that the system is live.

Namely, BlueFoot sends the following particles of system information back to the ground-station:

- battery voltage levels
- power fault conditions
- foot contact feedback
- and joint position feedback.

This data is used to update several key portions of the UI. Battery levels are used to update a battery meter, which indicates the current system voltage level. Additionally, a dynamic text box displays the system's power-fault state to the user. Joint position and foot-contact information is used to update a visualization of the robot in real time. Joint positions, foot-contact states and battery levels are time-stamped and automatically logged during each ground-station session.

## CHAPTER IV

### System Modeling

#### 4.1 Kinematic Model

The kinematic model of the BlueFoot platform is paramount for trajectory planning, localization, and adaptation in the robot task-space. In particular, inverse position and velocity solutions are used to prescribe joint-space commands from particular foot trajectories planned in the world coordinate frame. Additionally, BlueFoot’s forward kinematic model is utilized to estimate the position of each foot using the position and orientation of the trunk; and joint position feedback. This section will describe BlueFoot’s forward and inverse kinematic models, as well as how these models are used in motion planning and control tasks.

##### 4.1.1 Forward Position Kinematics

To formulate the kinematics model, a set of coordinate systems have been defined and are described by Figure 13. Note that the frame  $O_0$  represents the world coordinate frame; and  $O_b$  is the coordinate frame, centered at  $p_b$  attached to the platform and is always aligned with  $O_0$ .  $O_b$  represents a body frame rigidly attached to the center of the trunk. The orientation and position of the trunk are defined by vectors of  $\theta_b \in \mathcal{R}^3$  and  $p_b \in \mathcal{R}^3$ , which relate the frame  $O_b$  to the world frame  $O_0$ . Coordinate frames  $O_{i,0}$  are attached to the first joint of each  $i^{th}$  leg. The  $j^{th}$  joint position of each  $i^{th}$  leg is represented by the points  $p_{i,j}$  in the frame  $O_0$ . These spatial locations are generated from a combination of the body orientation,  $\theta_b$ , and joint positions for each  $i^{th}$  leg,  $q_i = [q_{i,1}, q_{i,2}, q_{i,3}, q_{i,4}]^T$ .  $q_{i,1}$  represents the position of the hip-joint (joint closest to the center platform), which rotates in the direction of the transverse body plane. The joint variables  $q_{i,2}, q_{i,3}$  and  $q_{i,4}$  represent the lateral-hip, knee and ankle joint rotations, respectively.

The coordinate transformation between world coordinate frame,  $O_0$ , and the zeroth Denavit-Hartenberg (DH) coordinate frame of leg  $i$ ,  $O_{i,0}$  (located at the origin of joint-1),

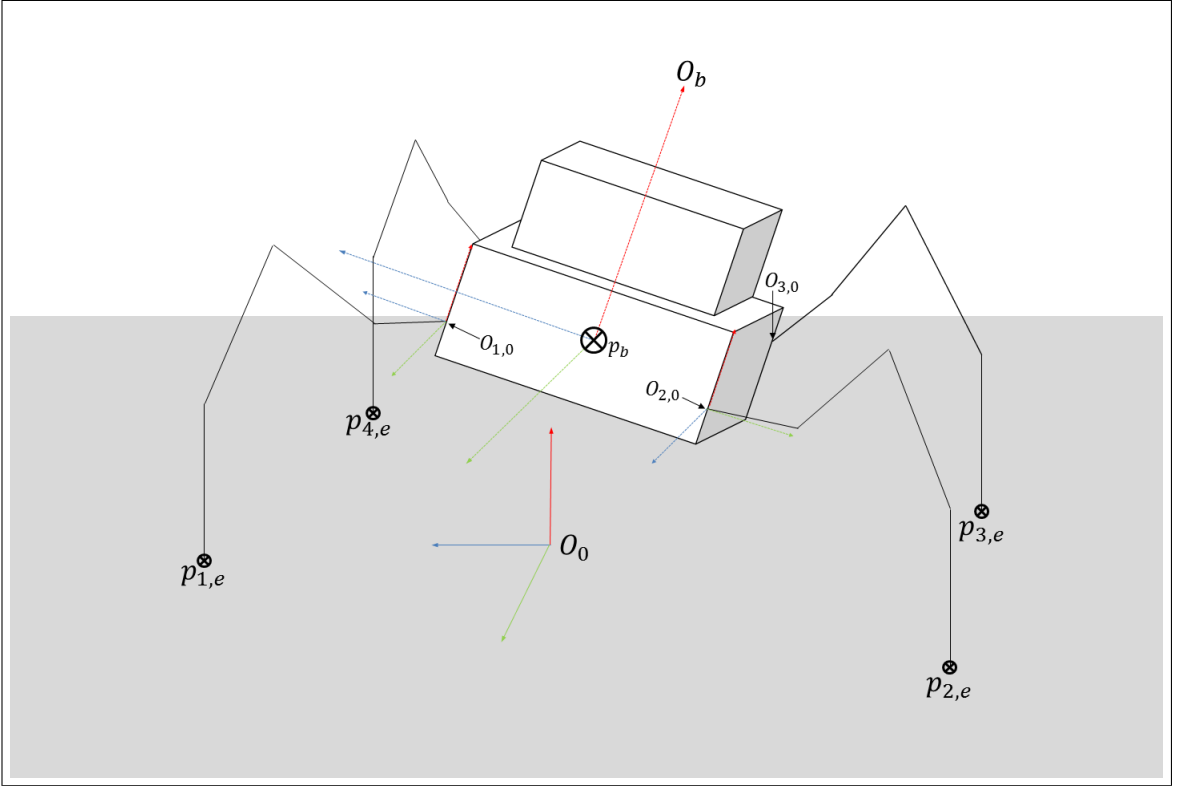


Figure 13: A visualization of BlueFoot’s coordinate frame configuration.

is given by

$$H_0^{i,0} = \left[ \begin{array}{c|c} R_{zyx}(\theta_b)R_z(\sigma_i) & R_{zyx}(\theta_b)\nu + p_b \\ \hline 0 & 1 \end{array} \right] \quad (4.1)$$

where  $\sigma_i \equiv \frac{\pi}{2}(i-1) + \frac{\pi}{4}$  and  $\nu \equiv R_z(\sigma_i)\beta$  with  $\beta$  defining an offset from  $O_b$  to where the first joint of each leg is attached to the body.  $R_{zyx}$  represents a rotation associated with the pitch (x-axis), roll (y-axis), and yaw (z-axis) angles of the main body about the platform frame,  $\theta_b$ .  $R_z$  represents a rotation about the (z-axis) of the frame  $O_b$ .

A transformation from the zeroth DH frame of the to the  $(j+1)^{th}$  joint of leg  $i$  is described, in general, by

$$H_{i,j}^{i,0} = \left[ \begin{array}{c|c} R_{i,j}^{i,0} & p_{i,j}^{i,0} \\ \hline 0 & 1 \end{array} \right]. \quad (4.2)$$

The kinematics of each leg are identical. Thus, the transformations  $H_{i,j}^{i,0}$  are of the same form and are derived by the DH parameters given by Table 9. Actual values for the link lengths  $a_{1-4}$  and body-offset,  $\nu$ , are provided in Table 1.

Using these DH parameters, the transformations  $H_{i,1}^{i,0}$ ,  $H_{i,2}^{i,0}$ ,  $H_{i,3}^{i,0}$ , and  $H_{i,4}^{i,0}$  can be computed explicitly as follows:

| Link | $a_i$ | $\alpha_i$ | $d_i$ | $\theta_i$  |
|------|-------|------------|-------|-------------|
| 1    | $a_1$ | $\pi/2$    | 0     | $q_{i,1}^*$ |
| 2    | $a_2$ | 0          | 0     | $q_{i,2}^*$ |
| 3    | $a_3$ | 0          | 0     | $q_{i,3}^*$ |
| 4    | $a_4$ | 0          | 0     | $q_{i,4}^*$ |

Table 9: DH parameters for all legs.

$$H_{i,1}^{i,0} = \left[ \begin{array}{ccc|c} c_{1,i} & 0 & s_{1,i} & c_{1,i}a_{1,i} \\ s_{1,i} & 0 & -c_{1,i} & s_{1,i}a_{1,i} \\ 0 & 1 & 0 & 0 \\ \hline 0 & 0 & 0 & 1 \end{array} \right] \quad (4.3)$$

$$H_{i,2}^{i,0} = \left[ \begin{array}{ccc|c} c_{1,i}c_{2,i} & -c_{1,i}s_{2,i} & s_{1,i} & c_{1,i}(a_{1,i} + a_2c_{2,i}) \\ s_{1,i}c_{2,i} & -s_{1,i}s_{2,i} & -c_{1,i} & s_{1,i}(a_{1,i} + a_2c_{2,i}) \\ s_{2,i} & c_{2,i} & 0 & a_2s_{2,i} \\ \hline 0 & 0 & 0 & 1 \end{array} \right] \quad (4.4)$$

$$H_{i,3}^{i,0} = \left[ \begin{array}{ccc|c} c_{1,i}c_{23,i} & -c_{1,i}s_{23,i} & s_{1,i} & c_{1,i}(a_{1,i} + a_2c_{2,i} + a_3c_{23,i}) \\ s_{1,i}c_{23,i} & -s_{1,i}s_{23,i} & -c_{1,i} & s_{1,i}(a_{1,i} + a_2c_{2,i} + a_3c_{23,i}) \\ s_{23,i} & c_{23,i} & 0 & a_2s_{2,i} + a_3s_{23,i} \\ \hline 0 & 0 & 0 & 1 \end{array} \right] \quad (4.5)$$

$$H_{i,4}^{i,0} = \left[ \begin{array}{ccc|c} c_{1,i}c_{234,i} & -c_{1,i}s_{234,i} & s_{1,i} & c_{1,i}(a_{1,i} + a_2c_{2,i} + a_3c_{23,i} + a_4c_{234,i}) \\ s_{1,i}c_{234,i} & -s_{1,i}s_{234,i} & -c_{1,i} & s_{1,i}(a_{1,i} + a_2c_{2,i} + a_3c_{23,i} + a_4c_{234,i}) \\ s_{234,i} & c_{234,i} & 0 & a_2s_{2,i} + a_3s_{23,i} + a_4s_{234,i} \\ \hline 0 & 0 & 0 & 1 \end{array} \right] \quad (4.6)$$

A summary of abbreviations for trigonometric terms in (4.3)-(4.6) is included in Appendix C.

The position of joint 1 of leg  $i$  in  $O_0$ ,  $p_{i,1}$  may now be computed with respect to frame  $O_0$  by:

$$p_{i,1} \equiv E_p H_0^{i,0} e_p. \quad (4.7)$$

where

$$E_p = [I_{3 \times 3}, 0_{3 \times 1}]$$

$$e_p = [0_{1 \times 3}, 1]^T.$$

The position of joints 2-4 of leg  $i$ , may now be computed with respect to frame  $O_0$  by:

$$p_{i,j} \equiv E_p H_0^{i,0} H_{i,(j-1)}^{i,0} e_p. \quad \forall j \in \{2, 3, 4\} \quad (4.8)$$

Finally, the position of the end-effector (foot) of  $i^{th}$  leg.  $p_{i,e}$ , is achieved as follows:

$$p_{i,e} \equiv E_p H_0^{i,0} H_{i,4}^{i,0} e_p. \quad (4.9)$$

As a previously mentioned, BlueFoot's forward kinematic solution is used most prevalently in the estimating the position of each foot. Given estimates for body position and orientation,  $\hat{p}_b$  and  $\hat{\theta}_b$ , a foot position estimate is explicitly define as a random variable:

$$\hat{p}_{i,e} = p_{i,e} + \Delta p_{i,e} \quad (4.10)$$

where  $\Delta p_{i,e}$  is a random error which arises from variations due to noise in sensed joint positions, as well as error in the estimates  $\hat{p}_b$  and  $\hat{\theta}_b$ .

### A Note about foot localization in the robot-relative frame, $O_b'$

Using the previously defined forward kinematics model and the relationships defined in (4.8) and (4.9), the position of each joint and foot can be computed assuming the  $p_b$  and  $\theta_b$  are known (or can be estimated) in the frame  $O_0$ . Provided inertial feedback, trunk orientation,  $\theta_b$ , can be estimated by the use of an Extended Kalman Filter (EKF).  $p_b$ , however, requires more sophisticated localization measures, such as a Simultaneous Localization and Mapping (SLAM) scheme or absolute positioning via overhead camera or GPS. In lieu of an implementation for such a localization routine, it is convenient to generate foot position estimates in a *robot-relative* frame,  $O_b'$ . This frame is not rigidly attached to the robot but moves along with the robot in  $O_0$  according to the commanded translational velocity,  $v^r$ , and turning rate.  $\omega^r$ , administered to navigate the system. These values will be described in more detail in Chapters V and VI. Moreover, this frame has its own position relative to  $O_0$ , defined by the translation  $p_0^{b'}$ .  $O_b'$  is constantly aligned to  $O_0$ , with respect to rotation, making the rotation matrix which relates  $O_b'$  to  $O_0$  the identity matrix.

In this frame, the trunk position is regarded as an offset from the origin of  $O_{b'}$ ,  $p_b^{b'}$ . Since there is zero rotation between  $O_0$  and  $O_{b'}$ , the trunk rotation vector  $\theta_b^{b'}$  is directly equivalent to  $\theta_b$  in  $O_0$ . Using these translation and rotation definitions in place of their world frame counterparts, the robot-relative joint and foot-positions,  $p_{i,j}^{b'}$  and  $p_{i,e}^{b'}$  of each  $i^{th}$  leg can be computed by defining a transformation from the robot relative frame to the first DH-frame for each leg, as follows:

$$H_{b'}^{i,0} = \left[ \begin{array}{c|c} R_{zyx}(\theta_b)R_z(\sigma_i) & R_{zyx}(\theta_b)\nu + p_b^{b'} \\ \hline 0 & 1 \end{array} \right] \quad (4.11)$$

which follows the same definitions in (4.1). The transformation defined in (4.11) is used as a direct replacement for the matrix  $H_0^{i,0}$  in (4.8) and (4.9) in computing the corresponding positions,  $p_{i,j}^{b'}$  and  $p_{i,e}^{b'}$ . Knowledge of these positions is useful for planning foot and body-placement which depend directly on the location relative foot and body positions, but do not necessarily depend on the position of the robot in the world coordinate frame.

#### 4.1.2 Inverse Position Kinematics

A foot configuration is specified by its coordinates  $p_e$  and an ankle orientation,  $\gamma_i$ , which represents a rotation about the axis of rotation of the second joint (lateral hip). Given a desired platform configuration,  $\{p_b, \theta_b\}$ , and desired  $i^{th}$  foot configuration,  $\{p_{i,e}, \gamma_i\}$ , the inverse kinematics solution for each  $i^{th}$  leg,  $q_i$ , is derived to be:

$$\begin{aligned} q_{i,1} &= \cos(i\pi) \left( \frac{\pi}{4} - \psi_i \right) \\ q_{i,2} &= \tan^{-1} \left( \frac{\zeta_{i,z}}{\sqrt{\zeta_{i,x}^2 + \zeta_{i,y}^2}} \right) \mp \cos^{-1} \left( \frac{a_3^2 - a_2^2 - \|\zeta_i\|^2}{2a_2 \|\zeta_i\|} \right) \pm \pi \\ q_{i,3} &= \mp \cos^{-1} \frac{\|\zeta\|^2 - a_2^2 - a_3^2}{2a_2 a_3} \\ q_{i,4} &= \gamma_i - q_{i,2} - q_{i,3} \end{aligned} \quad (4.12)$$

where

$$\begin{aligned}
p_{i,e}^{i,0} &= E_p (H_{i,k}^0)^{-1} \begin{bmatrix} p_{i,e} \\ 1 \end{bmatrix} \\
\psi_i &\equiv \tan^{-1} \left( \frac{[p_{i,e}^{i,0}]_y}{[p_{i,e}^{i,0}]_x} \right) \\
\zeta_{i,x} &\equiv [p_{i,e}^{i,0}]_y \sin(\psi_i) + [p_{i,e}^{i,0}]_x \cos(\psi_i) - a_4 \cos(\gamma_i) - a_1 \\
\zeta_{i,y} &\equiv [p_{i,e}^{i,0}]_y \cos(\psi_i) - [p_{i,e}^{i,0}]_x \sin(\psi_i) \\
\zeta_{i,z} &\equiv [p_{i,e}^{i,0}]_z - a_4 \sin(\gamma_i).
\end{aligned} \tag{4.13}$$

Here,  $p_{i,e}^{i,0}$  represents the position of each  $i^{th}$  foot with respect to the zeroth DH frame of each  $i^{th}$  leg; and  $[p_{i,e}^{i,0}]_x$ ,  $[p_{i,e}^{i,0}]_y$  and  $[p_{i,e}^{i,0}]_z$  represent the  $x$ ,  $y$ , and  $z$  axis coordinates of the vector  $p_{i,e}^{i,0}$ . The selection matrix  $E_p$  is the same as in (4.7)-(4.9).

It is important to note that the ankle specification,  $\gamma_i$ , adds extra constraints on the system kinematics and, thus, reduces the number of inverse kinematics solutions per foot position to two.

#### 4.1.3 Range of Motion

The range of articulation of BlueFoot's main body has been characterized with respect to a set of imposed joint limits (see Table 10) and has been performed with all feet fixed in a default stance (see Table 12). These limits have been selected according to the range of feasible angular position outputs of inverse position kinematics solution. It

| Joint Var. | $\theta_{i,1}$ , rad | $\theta_{i,2}$ , rad | $\theta_{i,3}$ , rad | $\theta_{i,4}$ , rad |
|------------|----------------------|----------------------|----------------------|----------------------|
| Max Range  | $45^\circ$           | $90^\circ$           | $90^\circ$           | $90^\circ$           |
| Min Range  | $-45^\circ$          | $-90^\circ$          | $-90^\circ$          | $-90^\circ$          |

Table 10: Imposed joint limits.

should be noted that the imposed joint limits are soft limits that have been chosen because of the typical range of motion executed by each joint during locomotion. Physical joint limits are tabulated in Table 11.

Figures 14 depicts the maximum pitch and roll and region of planar motion that the main body can reach while in the default stance. The blue shaded region of each figure (labeled *Region of Failure*) depicts points at which joint positions exceed the imposed

| Joint Var. | $q_{i,1}$ , rad | $q_{i,2}$ , rad | $q_{i,3}$ , rad | $q_{i,4}$ , rad |
|------------|-----------------|-----------------|-----------------|-----------------|
| Max Range  | $82^\circ$      | $102^\circ$     | $102^\circ$     | $102^\circ$     |
| Min Range  | $-69^\circ$     | $-102^\circ$    | $-102^\circ$    | $-102^\circ$    |

Table 11: Physical joint limits.

|       | $p_b^{b'}$ | $p_{1,e}^{b'}$ | $p_{2,e}^{b'}$ | $p_{3,e}^{b'}$ | $p_{4,e}^{b'}$ |
|-------|------------|----------------|----------------|----------------|----------------|
| x (m) | *          | 0.165          | -0.165         | -0.165         | 0.165          |
| y (m) | *          | 0.165          | 0.165          | -0.165         | -0.165         |
| z (m) | 0.115      | 0              | 0              | 0              | 0              |

Table 12: Locations for the platform and feet when in the default stance, written with respect to the frame  $O_{b'}$ .

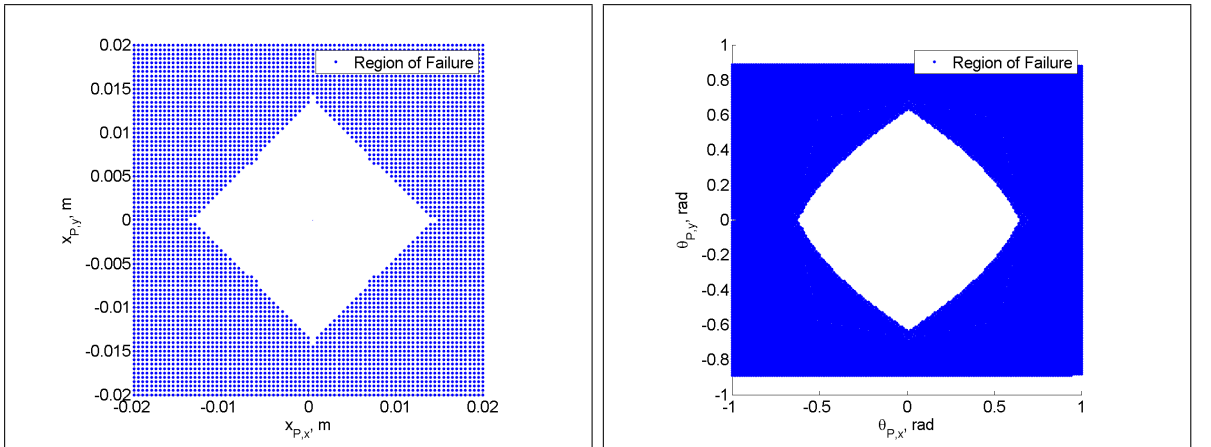


Figure 14: Range of motion for body's planar position (*left*) and body pitch and roll (*right*) while in the default stance.

limits. It can be seen from Figures 14 that the platform can achieve a maximum pitch and roll of  $\pm 37^\circ$  and a total displacement of  $\pm 1.4$  cm along the  $x$  and  $y$ -axis of  $O_{b'}$ .

#### 4.1.4 Velocity Kinematics

Using the DH-coordinate transformation,  $H_{i,4}^{i,0}$ , the velocity kinematics of each  $i^{th}$  leg are derived as the Jacobian  $J_{i,e}^{i,0} \in \mathcal{R}^{6 \times 4}$  where

$$\dot{x}_{i,e}^{i,0} = J_{i,e}^{i,0} \dot{q}_i \quad (4.14)$$

with  $\dot{x}_{i,e}^{i,0} \in \mathcal{R}^6$  being stacked vector of translational and rotational velocities,  $\dot{p}_{i,e}^{i,0} \in \mathcal{R}^3$  and  $\dot{\theta}_{i,e}^{i,0} \in \mathcal{R}^3$ , respectively, of each  $i^{th}$  foot with respect to frame  $O_{i,0}$ . The matrix  $J_{i,e}^{i,0}$  is defined explicitly in Appendix A.

Assuming the translational and rotational velocity of the trunk,  $\dot{p}_b$  and  $\dot{\theta}_b$ , respectively; and the translational and rotational of each  $i^{th}$  foot,  $\dot{p}_{i,e} \in \mathcal{R}^3$  and  $\dot{\theta}_{i,e} \in \mathcal{R}^3$ , respectively, are known, the translation velocity of each  $i^{th}$  foot can be written with respect to frame  $O_{i,0}$  by:

$$\dot{p}_{i,e}^{i,0} \equiv (R_{i,0}^0)^T (\dot{p}_{i,e} - \dot{p}_b - S(\dot{\theta}_b) (p_{i,e} - p_b - R_{i,0}^0 \vec{o}_\nu)) \quad (4.15)$$

where  $\vec{o}_\nu = [\nu, 0, 0]^T$ ,  $R_{i,0}^0$  is the rotation-matrix component of the transformation  $H_{i,0}^0$  defined in (4.1), and  $S(*)$  is a skew-symmetric matrix operator, which takes a  $3 \times 1$  vector input. The corresponding rotational velocity of each  $i^{th}$  foot can be computed with respect to  $O_{i,0}$  by:

$$\Theta^{i,0} \equiv (R_{i,0}^0)^T S(\dot{\theta}_{i,e} - \dot{\theta}_b) R_{i,0}^0 = S(\dot{\theta}_{i,e}^{i,0}) \quad (4.16)$$

where the rotational velocity of each foot, described by  $\dot{\theta}_{i,e}^{i,0}$ , is recovered by:

$$\dot{\theta}_{i,e}^{i,0} \equiv [-\Theta_{1,2}^{i,0}, \Theta_{1,3}^{i,0}, -\Theta_{2,3}^{i,0}]^T \quad (4.17)$$

with  $\Theta_{j,k}^{i,0}$  being the  $k^{th}$  element in the  $j^{th}$  row of the skew symmetric matrix  $\Theta_{j,k}^{i,0}$  which results from (4.16).

Joint velocities required to attain  $\dot{x}_{i,e}^{i,0}$  can be computed using  $J_{i,e}^{i,0}$ . However, since each of BlueFoot's of legs has 4 degrees of freedom,  $J_{i,e}^{i,0}$  is rank deficient and  $\dot{q}_i$  cannot be obtained by direct inversion. Instead,  $\dot{q}_i$  can be approximated from  $\dot{x}_{i,e}^{i,0}$  by a weighted, Penrose-Moore psuedo-inverse of  $J_{i,e}^{i,0}$ , which is defined as follows:

$$\begin{aligned} \dot{q}_i &\approx [J_{i,e}^{i,0}]_{\Lambda_j}^\dagger \dot{x}_{i,e}^{i,0} \\ \dot{q}_i &\approx \left( (J_{i,e}^{i,0})^T J_{i,e}^{i,0} + \Lambda_J \right)^{-1} (J_{i,e}^{i,0})^T \dot{x}_{i,e}^{i,0} \end{aligned} \quad (4.18)$$

where  $\Lambda_J$  is a strictly positive-definite weighting matrix that is typically chosen to have

$$\det(\Lambda_J) \ll 1.$$

The operator  $[*]_{\Lambda_j}^\dagger$  defines a weighted pseudo-inversion off a matrix argument  $(*)$  given a positive-definite weighting matrix  $\Lambda_j$ . A weighted pseudo-inversion is chosen over direct psuedo-inversion to avoid a non-smooth set of solutions  $\dot{q}_i$ . Degenerate solutions for  $\dot{q}_i$  exist at particular manipulator configurations where  $\left( (J_{i,e}^{i,0})^T J_{i,e}^{i,0} \right)$  is non-invertible.

## 4.2 Dynamical Model

### 4.2.1 System State Vector and General-Form Dynamics

The dynamical model of the BlueFoot platform is treated a general, free-floating body with four ridged legs, each of which have four degrees of freedom. This system is fully described by the state vector  $z \equiv [\eta^T, \dot{\eta}^T]^T \in \mathcal{R}^{44}$  and its dynamics are:

$$M(\eta)\ddot{\eta} + C(\eta, \dot{\eta})\dot{\eta} + G(\eta) + \Delta H = \tau + J^T(\eta)f_{ext} \quad (4.19)$$

where  $M(\eta)$ ,  $C(\eta, \dot{\eta})$ ,  $G(\eta)$  and  $J(\eta)$  represent the system mass matrix, Coriolis matrix, gravity matrix and Jacobian, respectively [51].  $\Delta H$  has been included as a lump term to account for dynamical uncertainties, such as friction or unmodeled coupling effects. Additionally,  $f_{ext} = [f_{1,ext}^T, f_{2,ext}^T, f_{3,ext}^T, f_{4,ext}^T]^T \in \mathcal{R}^{24}$  represents a stacked vector of force-wrenches,  $f_{i,ext} \in \mathcal{R}^6$ , applied to the system through each  $i^{th}$  foot. The state vector,  $\eta$ , can be partitioned as follows:  $\eta = [p_b^T, \theta_b^T, q^T]^T$  with  $p_b \in \mathcal{R}^3$  and  $\theta_b \in \mathcal{R}^3$  representing the position and orientation, respectively, of the quadruped's trunk in an arbitrarily placed world coordinate frame, and  $q \in \mathcal{R}^{16}$  is a vector of joint variables,  $m$  of which are contributed by each leg.  $\tau \in \mathcal{R}^{22}$  represents a vector of generalized torque inputs and takes the form  $\tau = [0_{1x6}, \tau_q^T]^T$  where  $\tau_q$  represents a set of torque inputs to each joint. It is important to note that the states we are most interested in controlling,  $p_b$  and  $\theta_b$ , are not directly actuated, and must be controlled via composite leg joint motions.

BlueFoot's dynamics, from (4.19), can be realized in a general, compact, state-space form by:

$$\begin{aligned} \dot{z}_1 &= z_2 \\ \dot{z}_2 &= M^{-1}(z_1)(\tau + \Phi(z_1, z_2, f_{ext})) \\ \Phi(z_1, z_2, f_{ext}) &= J^T(z_1)f_{ext} - C(z_1, z_2)z_2 - G(z_1) - \Delta H \end{aligned} \quad (4.20)$$

where  $z_1 = \eta$  and  $z_2 = \dot{\eta}$ . The notation  $\Phi(z_1, z_2, f_{ext})$  is introduced for convenience as a composite dynamical term. This term will be referred to, simply, as  $\Phi$  in the sections that follow. The system dynamics are also considered in an approximate, discrete-time (first-order) form as follows:

$$\begin{aligned} z_{1,k+1} &= z_{1,k} + (e_{1,k}^{\Delta_s} + z_{2,k})\Delta_s \\ z_{2,k+1} &= z_{2,k} + M_{1,k}^{-1}(e_{2,k}^{\Delta_s} + \tau_k + \Phi_k)\Delta_s \\ t &= \Delta_s k \end{aligned} \quad (4.21)$$

where  $M_{1,k} = M(z_{1,k})$  and  $\Delta_s \equiv (f_s)^{-1}$  with  $f_s$  defining a uniform sampling frequency in Hz. The terms  $e_{1,k}^{\Delta_s}$  and  $e_{2,k}^{\Delta_s}$  are used to explicitly account for system discretization errors, which vary with respect to the step-size,  $\Delta_s$ .

#### 4.2.2 Joint-Servo Dynamics

The motor dynamics driving each joint need to be considered for use in control design since the input to BlueFoot’s servo motors at each joint is a reference position command. In model-based control schemes to follow, a simple model of the motor dynamics will be utilized. Moreover, servos are considered as simple torque generators of the following form:

$$\tau_q = k_s(q^r - q) \quad (4.22)$$

where  $k_s > 0$  is a constant, scalar gain and  $q^r$  is a joint position reference. The servos being utilized to drive the leg joints of the BlueFoot quadruped have high-gain position feedback which allows us to model the motors, simply, as a static block which transform reference trajectories to torque outputs. All of these servos are identical, and thus have identical gains. One could instead consider the full motor dynamics for computing reference positions given a desired torque. The simple model stated above was adequate for achieving desired results with all proposed control schemes which use this torque-generator model.

#### 4.2.3 Single Leg Dynamics

The dynamics of each independent leg (with each base-frame fixed) can be derived in closed form using a Lagrangian formulated using the total potential and kinetic energy. Here, the dynamics of each leg is formulated via a minimization of energy. Masses  $m_{i,j}$  along each  $i^{th}$  leg are taken to be centered at each  $j^{th}$  joint. These dynamics have been included as auxiliary matter in Appendix B using the previously defined notations.

### 4.3 BlueFoot Simulator

The BlueFoot platform is comprised of 17 rigid bodies, 16 of which are linkages between joints; and a main platform. Since each limb is formed from four revolute joints, the system has a total of 22 DOF, 16 of which are actuated. The main platform’s configuration is generated through particular configurations of the legs. Furthermore, because each linkage is constrained to a rotation about a single axis, the rigid-body dynamic model of the BlueFoot quadruped is represented by 44 states. These states

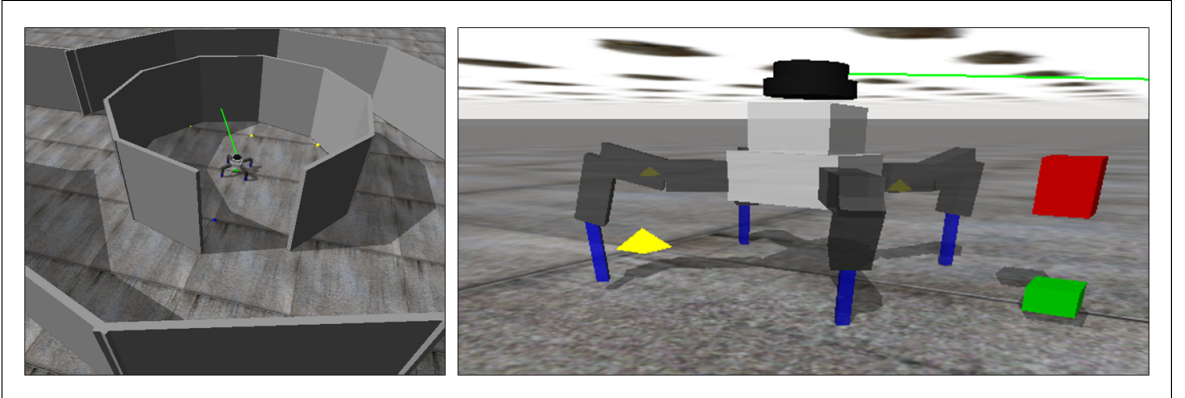


Figure 15: Visualization of the BlueFoot simulator.

represent the position and velocity of each joint,  $q_i$  and  $\dot{q}_i$ , respectively. Additionally, foot contact states are represented by binary scalars,  $\mu_i \in (0, 1)$ , which describes whether the foot is not in contact or in contact, respectively.

The dynamics of this system are somewhat complex because the quadruped’s legs continuously make and break contact with the ground during gaiting. Additionally, the surface attributes and contact effects may vary significantly during gaiting and for various environments. A numerical dynamics engine, Open Dynamics Engine (ODE) [52], has been utilized to implement a dynamics simulator for the BlueFoot platform. The simulator allows for various reconfigurations of environmental parameters, such as joint-friction, body-contact friction, and physical obstacles. Additionally, this simulation environment is implemented with a variety of geometric collision solvers and an efficient collision search method.

The simulator’s numerical engine, based on ODE, is updated at 1000 Hz to attain high-fidelity, especially during contact phases, which require higher-than-normal integration stability to achieve reasonable simulation accuracy. The input to the simulator is the desired main body configuration (i.e., position and orientation); desired foot placements; and desired ankle orientations, from which an inverse kinematic model is solved to attain all the desired joint configurations for the legs. Servos at each joint have built-in, tunable proportional controllers that effectively render them as ideal torque generators responding to the command input, as depicted in (4.22). To mimic the behavior of the system, the commands to each joint motor are updated at 50 Hz, which matches the update rates at which the actual robot serves the P-controllers at each joint with reference positions. This rate has been chosen to account for the speed of

inter-processor communications, and is adequate given the operating bandwidth of the robot.

The BlueFoot simulator utilizes a dynamical model of the platform which consists of purely rectangular bodies. To match the dynamics of the true system, the individual mass and inertia parameters of each rigid body have been generated using a 3D model analysis software. This software takes into account geometric irregularities and variation of materials when computing the inertia of each body. The simulator also contains IMU and LIDAR sensor models for gathering feedback from the simulated environment. Each sensor is modeled with appropriate measurement noise so as to more closely match the performances of the actual IMU and LIDAR sensors on-board the BlueFoot platform.

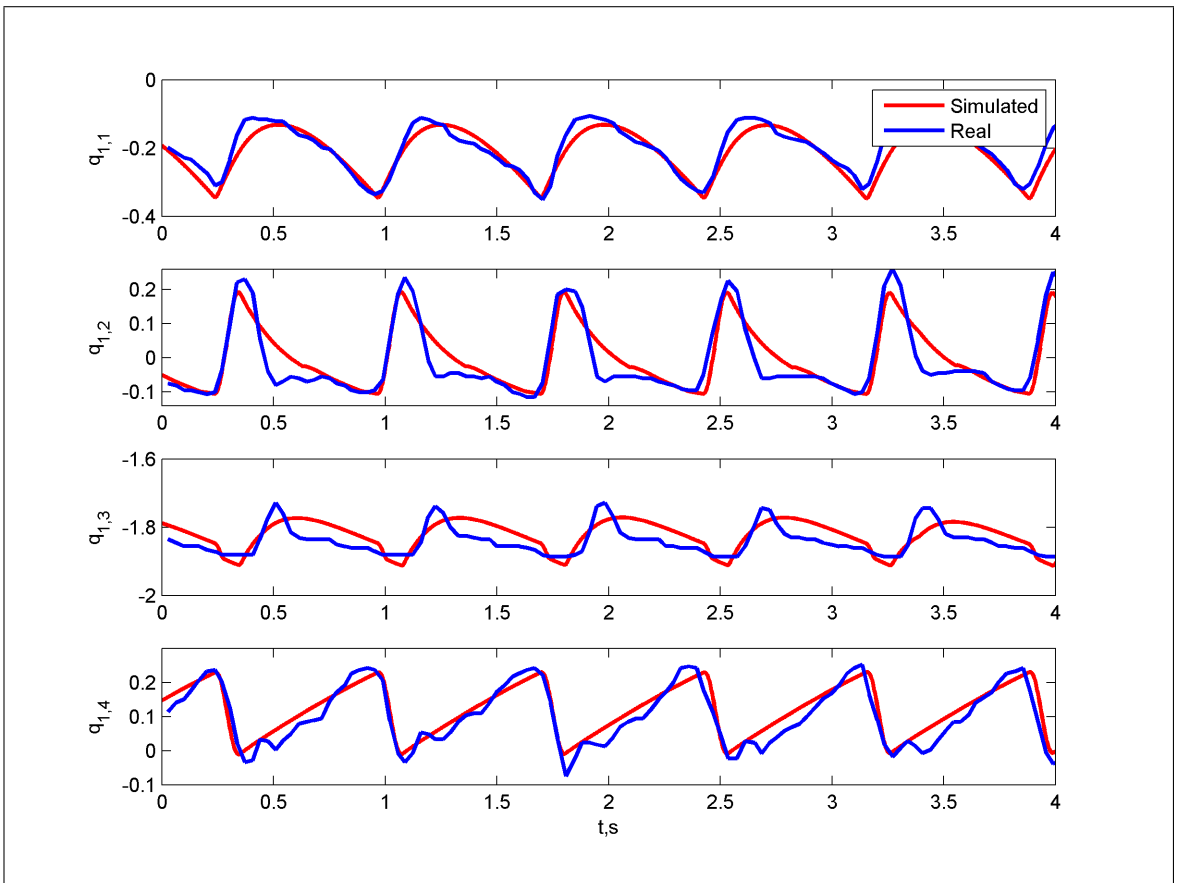


Figure 16: Joint position comparison between the simulated and real quadruped while performing a gait which achieves a forward velocity of  $60 \frac{mm}{s}$

Careful, manual tuning was performed on simulated robot parameters, including joint update gains, joint-friction and surface-friction model coefficients to achieve closer matches between simulated results and the actual robot motions. A performance com-

parison can be seen in 16, which shows joint position outputs for all joints of the front-right leg of the actual and simulated robot while performing a forward gait at 0.060 m/s. It can be seen in that the simulator provides and approximate representation true system performance within some margin of error. The discrepancies between the two data sets can be seen to usually occur at the minima of each series when the robot makes contact with the ground after a step. These differences can be attributed to ground-contact model inaccuracies. Work is still left to be done in improving the simulator's contact model, but this is more the fault of the simulation software libraries being used, namely in its low-order contact models. These contact models are very simplistic for the sake of simulation speed. Contact models could certainly be improved such that they more closely matches the effects of real-world surfaces. Additionally, discrepancies could also be attributed to the low-order joint model being used to represent the system's servo motors at each joint, described in (4.22). This model neglects the effects of higher-order frictional effects which modify the rotation profile at each joint. All of the other simulated leg joints exhibited similar results to the actual motions.

Despite these discrepancies, this simulation platform has proven to be adequate for use in testing gaiting and control algorithms which have been implemented on the real system. Moreover, all motion control algorithms which were first developed in this simulated environment have been ported to the real robot platform and performed in a highly comparable manner.

The simulator has also been utilized to model BlueFoot's on-board LIDAR unit for use in testing navigation and terrain mapping algorithms and associated motion routines. Laser hits are modeled as force-less collisions between a ray-type geometry, used to represent the laser beam of the LIDAR, and environmental elements. Because the ray geometry can penetrate environmental elements in multiple places, or even multiple elements within the environment at a single instance, some post processing is performed on collision point returned by the simulator such that the point of intersection *closest* to the robot is taken as a laser-beam hit. Additionally, sensor realism is imposed by limiting the data access frequency to buffered laser data to a rate of 10 Hz, which matches the scan rate of BlueFoot's on-board LIDAR. The angular velocity of the spinning laser head and the maximum depth of each laser beam hit are corrupted by zero-mean Gaussian random noise to match actual sensor performance.

## CHAPTER V

### Gaiting and Gait-Stability Control

#### 5.1 Overview

Legged robotic systems have long employed motion controllers based on limit cycle oscillators and, more recently, Central Pattern Generators (CPGs) for the purpose of generating bio-mimetic gaits [11, 13, 15–17, 53–56]. Since these motion control methods are open-loop motion planners (*i.e.*, not inherently formulated to incorporate feedback) they do not perform any active system stabilization on their own accord. As a result, implementations involving these locomotion methods often require auxiliary control mechanisms which provide gait stability. Fixed point methods, which include considerations of the system’s zero-moment point (ZMP) and center of gravity (COG), are utilized in the design of stable oscillator driven gaits. These methods are summarized in [5].

Developments in CPG-based gait controllers have led to the incorporation of “reflexive” feedback mechanisms aimed at correcting foot-placement during gaiting on uneven terrain or various surfaces. One such approach involves active compliance to each leg by directly modifying CPG oscillators units through feedback-driven modulations. In [6, 17], a CPG for each leg is modified by a neural oscillator with one tuning parameter.

This chapter will detail a similar, reflex-adaptive CPG gait generation method which utilizes IMU feedback to modify CPG limit-cycle parameters. Additionally, this section will present related motion-control methods implemented on the BlueFoot platform which aid in gait stabilization, including a virtual force-based foot placement planner and a ZMP-based body placement controller; as well as a learning-based control technique used to level BlueFoot’s trunk during gaiting.

#### 5.2 Central Pattern Generator (CPG) Based Gaiting

A central pattern generator (CPG), which includes a reflexive mechanism using sensory feedback, is utilized as the core of the robot’s gait generation algorithm. As previously introduced, CPGs are a form of neural oscillator network which mimic bi-

ological mechanisms for repetitive motor tasks [13, 54]. CPGs commonly consist of a network of multi-state unit-oscillators. These unit-oscillators are coupled such that the motion of one oscillator drives or attenuates the motion of other oscillators it is connected to, creating phase-locked limit cycles.

In this context, the limit-cycles generated with a CPG will be utilized to drive a quadruped walking gait by mapping oscillator outputs to foot position controls. CPGs are widely used in this way as they provide a compact method for prescribing rhythmic gaits with variable stepping sequences [15, 57, 58]. CPG-driven gait controllers are convenient as they allow for continuous transitioning between gaiting patterns through the modification of oscillator coupling. Reflexes are built into the oscillators which use IMU measurements to modulate the CPGs unit oscillators, as will be outlined later in this section.

The CPG implemented on BlueFoot consists of four modified two-state Hopf Oscillators connected through a coupling matrix  $K$ . The states of each  $i^{th}$  unit Hopf Oscillator are designated by the pair  $\{y_{1,i}, y_{2,i}\}$ . These oscillator states are stacked into the vectors  $y_1 \in \mathcal{R}^4$  and  $y_2 \in \mathcal{R}^4$ , which are composed as follows:

$$\begin{aligned} y_1 &= [y_{1,1}, y_{1,2}, y_{1,3}, y_{1,4}]^T \\ y_2 &= [y_{2,1}, y_{2,2}, y_{2,3}, y_{2,4}]^T \end{aligned}$$

The oscillator output vector  $y_2$ , parameterizes the trajectories of each  $i^{th}$  foot. The resulting reflexive CPG system, written with respect to the stacked-state vectors  $y_1$  and  $y_2$ , is described by

$$\begin{aligned} \dot{y}_1 &= A_1 (\Psi_M M(y_1, y_2) - \Gamma) y_1 + \Psi_\omega W y_2 \\ \dot{y}_2 &= A_2 (\Psi_M M(y_1, y_2) - \Gamma) y_2 - \Psi_\omega W y_1 + K y_2 \end{aligned} \quad (5.1)$$

where  $M(y_1, y_2) \in \mathcal{R}^{4 \times 4}$  is defined as

$$M(y_1, y_2) = \begin{bmatrix} y_{1,1}^2 + y_{2,1}^2 & 0 & 0 & 0 \\ 0 & y_{1,2}^2 + y_{2,2}^2 & 0 & 0 \\ 0 & 0 & y_{1,3}^2 + y_{2,3}^2 & 0 \\ 0 & 0 & 0 & y_{1,4}^2 + y_{2,4}^2 \end{bmatrix},$$

$A_1, A_2, \Psi_M, \Psi_\omega \in \mathcal{R}^{4 \times 4}$  are constant oscillator gain matrices; and  $\Gamma$  and  $W$  are diagonal

matrices, defined by

$$\Gamma = \begin{bmatrix} \gamma_1 & 0 & 0 & 0 \\ 0 & \gamma_2 & 0 & 0 \\ 0 & 0 & \gamma_3 & 0 \\ 0 & 0 & 0 & \gamma_4 \end{bmatrix}, \quad W = \begin{bmatrix} \omega_1 & 0 & 0 & 0 \\ 0 & \omega_2 & 0 & 0 \\ 0 & 0 & \omega_3 & 0 \\ 0 & 0 & 0 & \omega_4 \end{bmatrix},$$

which define the peak-to-peak output amplitude,  $\gamma_i$ , and frequency,  $\omega_i$ , of each  $i^{th}$  unit oscillator in the CPG network. A more specific design of the matrix  $W$ , with respect to a gait frequency parameter,  $\omega_s$ , is provided in (5.5).

### 5.2.1 Reflexive Gait Adaptations

Feedback signals are incorporated into the CPG through the frequency modulation matrix  $\Psi_\omega$  and amplitude modulation matrix  $\Psi_M$ . These modulation parameters are generated using state estimates of the platform's orientation and angular rate. The platform orientation state-estimate,  $\hat{\theta}_b$ , is supplied to the controller from an Extended Kalman Filter utilizing inertial measurement and magnetometer feedback (which are separately calibrated). The platform's angular rate is output by an angular rate-gyro sensor.

Feedback-based corrections to the CPG aid in tracking a specified body orientation  $\theta_b^r$  during gaiting. To achieve higher system velocities, it is often necessary to perform a gait wherein multiple legs leave contact with the ground. Configurations such as these would cause a quadruped robot to tip in the direction of the non-planted legs, thus disturbing  $\theta_b$ . These disturbances are counteracted, in part, by adjusting the CPG such that the amount of torque applied on the main body by legs in flight is actively limited. This is done by adjusting stepping height and time-of-flight according to a measure of disturbance (essentially, the amount and rate of tipping). These adjustments have been formulated to mimic reflexive behaviors that might be performed by a biological system.

When the robot's body begins to fall in particular direction (*i.e.*, is disturbed by legs in-flight during gaiting), the disturbance signal

$$\dot{\epsilon}_\theta = R_{z_b} \left( \frac{\pi}{2} \right) \left( \dot{\hat{\theta}}_b - \dot{\theta}_b^r \right) \quad (5.2)$$

is non-zero.  $\dot{\epsilon}_\theta$  represents a measure of translational drift recovered from gyroscopic sensor measurements.  $R_{z_b} \frac{\pi}{2}$  represents a rotation by  $\frac{\pi}{2}$  about the z-axis of the body

frame  $O_b$ .  $\dot{\epsilon}_\theta$  is mapped to the parameters  $\Psi_\omega$  and  $\Psi_M$  by

$$\begin{aligned}\psi_i &= \text{sig}(w_i v_i - w_i c_i) \mu_i \\ \Psi_\omega &= I + A_\omega \text{diag}(\psi_i) \\ \Psi_M &= I - A_\mu \text{diag}(\psi_i)\end{aligned}\quad (5.3)$$

where

$$\begin{aligned}v_i &= \|\dot{\epsilon}_\theta\| \left( 1 + \frac{\Delta x_i}{\|\Delta x_i\|}^T \frac{\dot{\epsilon}_\theta}{\|\dot{\epsilon}_\theta\|} \right) \\ \Delta x_i &= p_{i,e} - p_b\end{aligned}\quad (5.4)$$

with  $\{w_i, c_i\} \in \mathcal{R}$  and  $\{A_\mu, A_\omega\} \in \mathcal{R}^{4 \times 4}$  being tunable gains.  $\mu_i$  is used to represent the contact state of each  $i^{th}$  foot, and takes on a value of  $\mu_i = 1$  when a foot is in contact and  $\mu_i = 0$  when it is not.  $\text{sig}(\cdot)$  represents the standard sigmoid step function which takes a scalar argument  $(\cdot)$ . The signal  $v_i$  represents a projection of  $\dot{\epsilon}_\theta$  into the unit-vector emanating from  $p_b$  to each  $i^{th}$  foot. This projection delegates the level of adjustment to each  $i^{th}$  oscillator as a result of  $\dot{\epsilon}_\theta$ . Finally,  $\text{diag}(\psi_i) \in \mathcal{R}^{4 \times 4}$  defines a diagonal matrix whose  $i^{th}$  diagonal element is  $\psi_i \forall i \in \{1, 2, 3, 4\}$ .

Adjusting  $\Psi_\omega$  by the method delineated in (5.3) serves to shorten the stepping period of a leg in-flight given greater values of  $\dot{\epsilon}_\theta$ . Likewise,  $\Psi_M$  is adjusted to decrease the height of each foot in-flight. The frequency of a full gaiting cycle is prescribed via  $\omega_s$  and duty-factor  $\alpha \in [0, 1]$  [16]. The matrix  $W$  is formed from  $\omega_s$  and  $\alpha$  as follows:

$$W = \omega_s \alpha \begin{bmatrix} \frac{1}{1+e^{\zeta y_{2,1}}} & 0 & 0 \\ 0 & \ddots & 0 \\ 0 & 0 & \frac{1}{1+e^{\zeta y_{2,4}}} \end{bmatrix} + \omega_s(1-\alpha) \begin{bmatrix} \frac{1}{1+e^{-\zeta y_{2,1}}} & 0 & 0 \\ 0 & \ddots & 0 \\ 0 & 0 & \frac{1}{1+e^{-\zeta y_{2,4}}}\end{bmatrix} \quad (5.5)$$

and  $\zeta$  being a sensitivity tuning parameter. A linear mapping between commanded platform velocity,  $v^r$ , and  $\omega_s$  is prescribed such that stepping-cycle frequency is adjusted proportionally with respect to the desired velocity and turning rate of the system, as follows:

$$\omega_s = a_v v^r + a_\omega \|\omega^r\| \quad (5.6)$$

where  $a_v$  and  $a_\omega$  are scalar gains. In BlueFoot's CPG implementation, the coupling matrix  $K$  takes on the values  $k_{i,j} \in [-1, 1]$ . Each element of the coupling matrix,  $k_{i,j}$ , is utilized to adjust the phase offsets between the unit-oscillators. Furthermore, setting  $k_{i,j} = 1$  causes the  $j^{th}$  oscillator to attract the  $i^{th}$  oscillator towards a positive peak, and vice-versa. Setting  $k_{i,j} = 0$  effectively disconnects  $i^{th}$  and  $j^{th}$  oscillators.

Figures 17 and 18 depict the CPG output,  $y_2$ , and corresponding unit-oscillator phase portraits of the oscillator dynamics, given by (5.1) with the feedback mechanism given in (5.3) used during simulations of BlueFoot’s default two-pace trotting and four-pace walking gaits, respectively. The associated  $K$  matrix prescribing this gaiting pattern is a modified version of  $K$  for a 2-pace trot gait presented in [12], since this generates a more effective and fluid gait when applied to BlueFoot’s gait controller

$$K \equiv \begin{bmatrix} 0 & -1 & 1 & -0.5 \\ -1 & 0 & -0.5 & 1 \\ -1 & -0.5 & 0 & -1 \\ -0.5 & 1 & -1 & 0 \end{bmatrix}. \quad (5.7)$$

A comparable four-pace *walking* gait can be achieved by a slight sign modifications on the elements of (5.7), which yields (5.8) as follows:

$$K \equiv \begin{bmatrix} 0 & -1 & 1 & -0.5 \\ -1 & 0 & -0.5 & 1 \\ -1 & 0.5 & 0 & -1 \\ 0.5 & -1 & -1 & 0 \end{bmatrix}. \quad (5.8)$$

Figure 19 shows the change in output state patterns during a transition from a four-paced to a two-paced gait. Figure 20 shows joint angle feedback from the actual robot platform during the execution of a CPG driven gait which achieves a ground-speed of  $65 \frac{mm}{s}$ .

### 5.3 Foot Placement Control

A foot placement controller has been implemented which utilizes CPG outputs (defined in equation (5.1)) in concert with a virtual-force controller. This controller is designed such that each foothold of the robot tracks the foot positions of a virtual robot generated through a model reference. The virtual robot is described by the foot positions,  $\tilde{p}_{i,e}$ , a virtual reference configuration corresponding to the return-position,  $\tilde{p}_c$ , and orientation,  $\tilde{\theta}_c$ , of the main body in  $O_0$ . The robot follows the foot placement of the virtual robot to achieve a commanded ground speed  $v^r > 0$  in a unit-vector direction

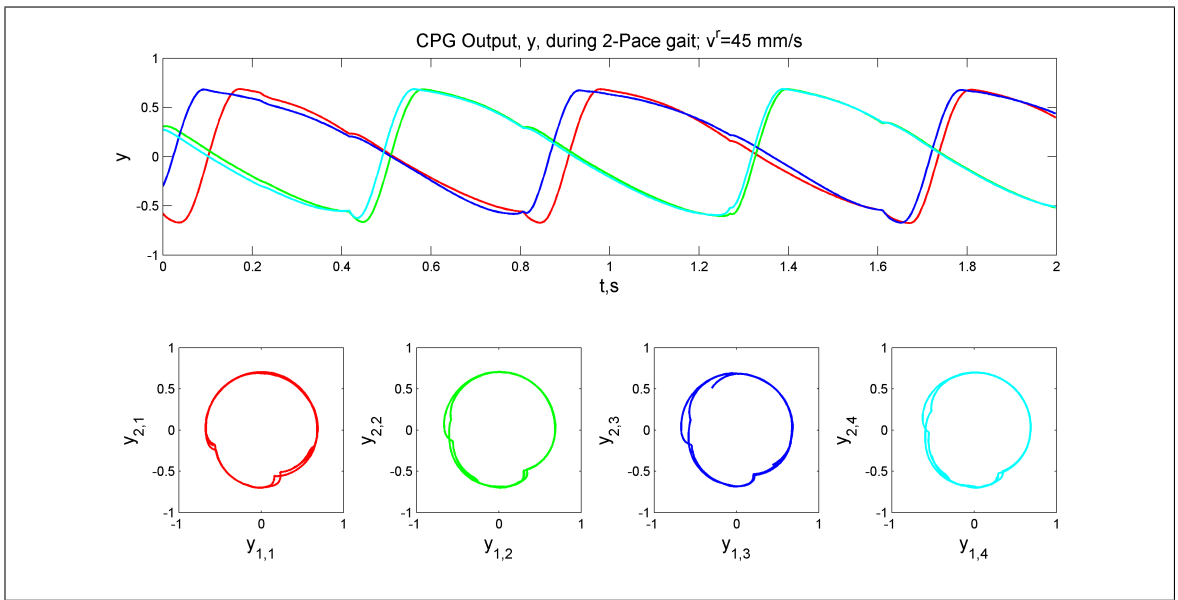


Figure 17: CPG output and phase plots for a two-paced gait over two gait cycles.

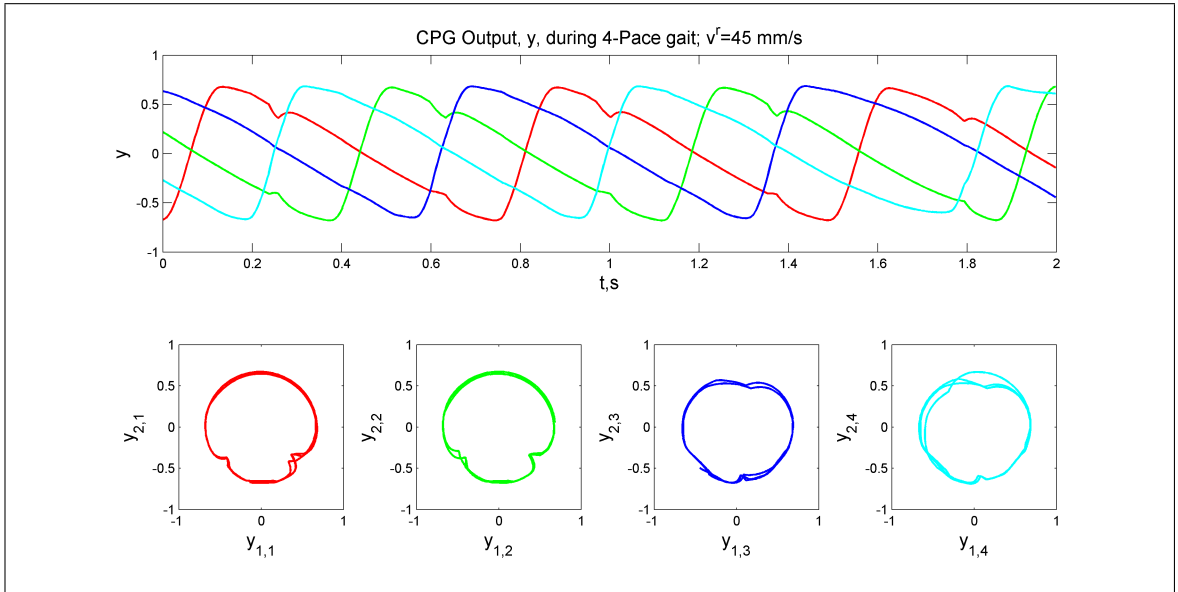


Figure 18: CPG output and phase plots for a four-paced gait over two gait cycles.

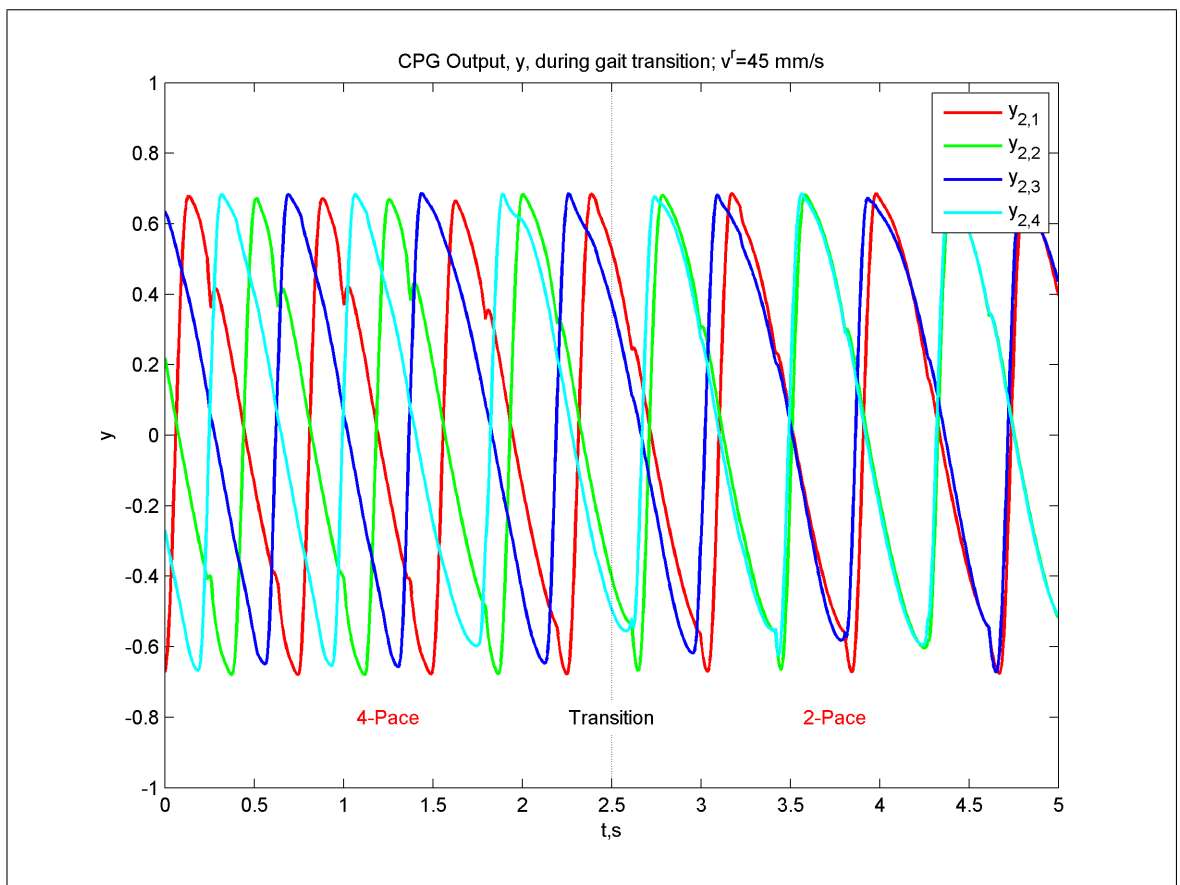


Figure 19: CPG output transition during four-pace to two-pace gait switch.

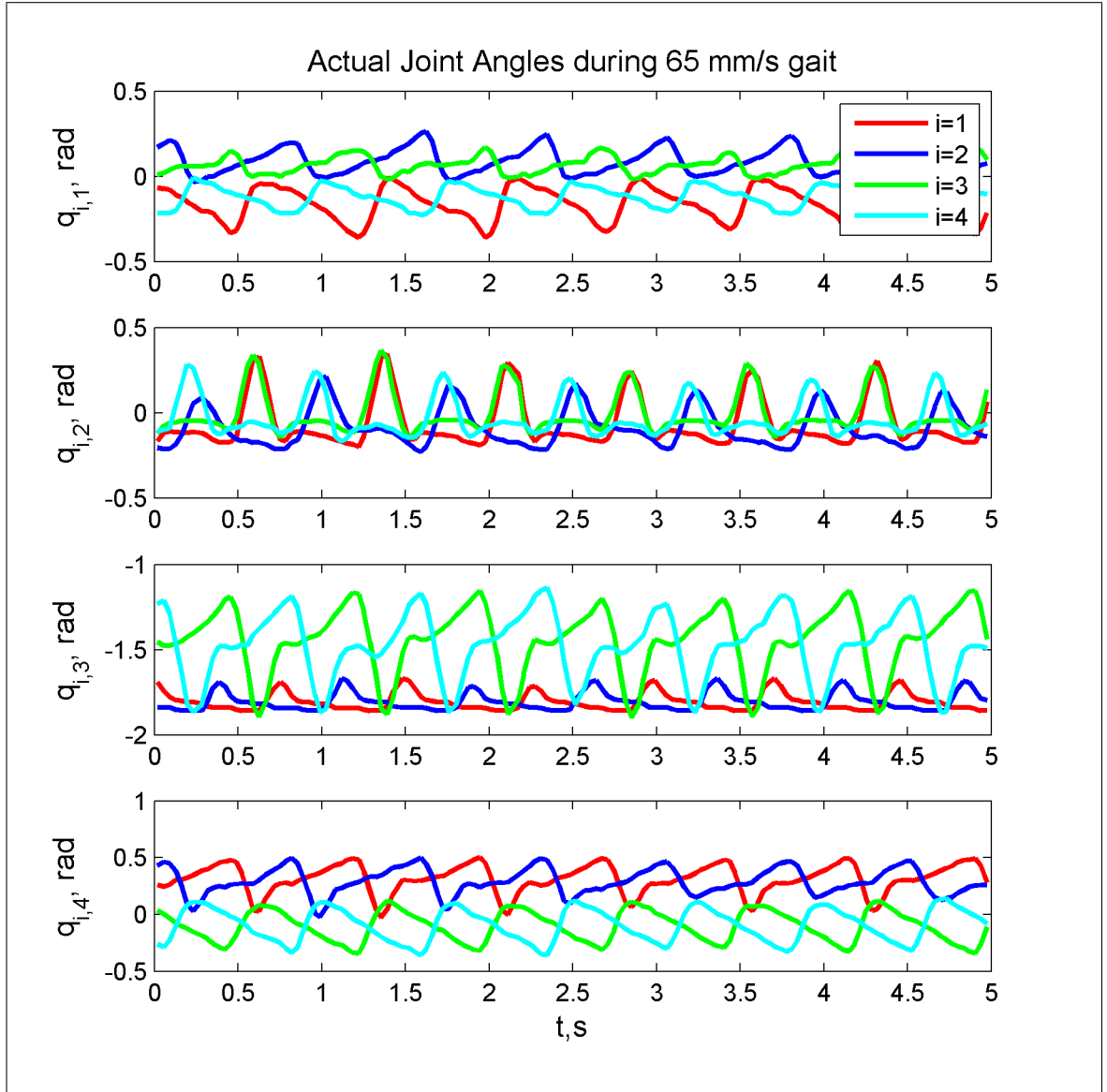


Figure 20: Real joint angles during a gait at  $65 \frac{mm}{s}$ .

$\vec{u}^r \in \mathcal{R}^3$ ; and turning velocity  $\omega^r \in \mathcal{R}$ . Each virtual point is updated by:

$$\begin{aligned}\dot{\tilde{\theta}}_c &= \omega^r \\ \dot{\tilde{p}}_c &= v^r \vec{u}^r \\ \dot{\tilde{p}}_{i,e} &= v^r \vec{u}^r + S(\omega^r \vec{h}_b) \tilde{R}_b (\tilde{p}_{i,e} - \tilde{p}_c)\end{aligned}\quad (5.9)$$

where  $\vec{h}_b$  is a unit vector that is orthogonal and pointed outward from the surface beneath the robot and  $S(\omega^r \vec{h}_b) \in \mathcal{R}^{3 \times 3}$  forms a skew-symmetric matrix from the vector argument  $\omega^r \vec{h}_b$ . The virtual foothold dynamics progress the target footholds at a commanded translational (forward) and rotational velocity,  $v^r$  and  $\omega^r$ , respectively. The robot follows the virtual model at nearly the same velocities with minimal lag so long as system bandwidth is not exceeded. Using this virtual-foothold method is convenient as it allows for foot-placement planning to be independent of foot-trajectory planning. For example, terrain adaptation can be incorporated by modifying the location of virtual foot positions such that they conform to an upcoming surface. The robot's gait will then track these adaptations without any explicit modification of foot trajectories. In the event of contact with unperceived terrain, virtual-foothold positions will reset with respect to an estimated point of contact for each  $i^{th}$  contacting foot (see Algorithm 2). In Algorithm 2,  $y_{2,i} > 0$  indicates that the  $i^{th}$  foot is in flight, as per the definition of the foot-height controller to be defined in (5.12). The foot-position estimate  $\hat{p}_{i,e}$  is defined in (4.10).

---

**Algorithm 2** Virtual foothold reset routine.

---

```

for all  $i$  in  $i = \{1, \dots, 4\}$  do
  if  $y_{2,i} > 0$  and  $\mu_i = 1$  then
     $\tilde{p}_{i,e} = \hat{p}_{i,e}$ 
  end if
end for
```

---

The full foothold controller represented by

$$\dot{p}_{i,e} = \dot{\tilde{p}}_{i,e}^v + \dot{\tilde{p}}_{i,e}^y, \quad i = \{1, \dots, 4\} \quad (5.10)$$

is a composite of a foot-repositioning and step-height controller which are formulated in terms of the dynamics of the signals  $\dot{\tilde{p}}_{i,e}^v$  and  $\dot{\tilde{p}}_{i,e}^y$ , respectively. Each foot is treated as a point mass attracted to their corresponding virtual foothold by an over-damped

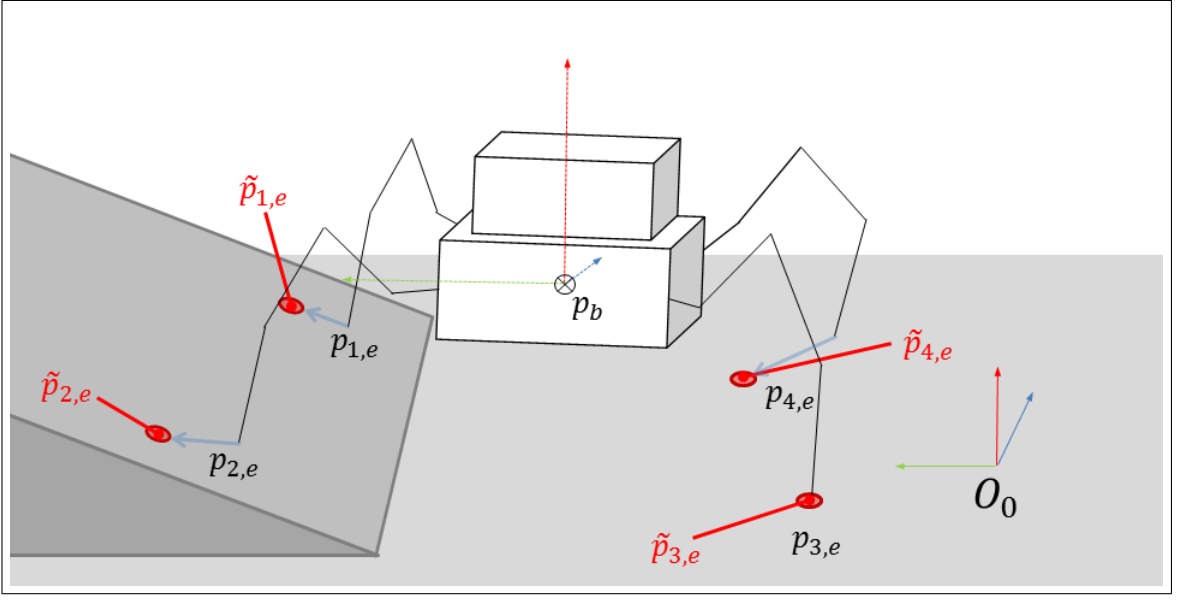


Figure 21: Virtual foothold representation. Blue arrows represent an attractive “force” between the feet and their corresponding virtual foothold.

mass-attractor system.  $\dot{\tilde{p}}_{i,e}^v$  is defined by

$$\dot{\tilde{p}}_{i,e}^v = \frac{1}{m_i} \int^t P_{\vec{h}_i} (F_{s,i} - b_c \dot{p}_{i,e} + F_{\epsilon,i}) d\tau \quad (5.11)$$

where

$$\begin{aligned} F_{s,i} &= k_c \mu_i (\tilde{p}_i - p_{i,e}) U(y_{2,i}) \\ F_{\epsilon,i} &= a_\epsilon \dot{\epsilon}_\theta U(y_{2,i}) \end{aligned}$$

with  $k_c, b_c, a_\epsilon, m_i \in \mathcal{R}$ .  $k_c$  and  $b_c$  represent attraction and viscous damping constants for the virtual force system.  $P_{\vec{h}_i}(\cdot)$  projects the sum of forces,  $(\cdot)$ , onto the surface beneath the  $i^{th}$  foot orthogonal to  $\vec{h}_i$ .  $U(y_{2,i})$  is a standard unit step function. The force  $F_{\epsilon,i}$  is a compensatory force to adjust for the inertial disturbance,  $\dot{\epsilon}_\theta$ . For instance, if the robot was pushed from the side of its body, this force would induce a side-stepping motion in attempt to catch the robot from falling in the direction of the push. Because of  $U(y_{2,i})$ ,  $F_{s,i}$  and  $F_{\epsilon,i}$  are nonzero only when  $y_{2,i}$  is positive.

The controller component  $\dot{\tilde{p}}_{i,e}^y$  is defined from the CPG output signal  $\dot{y}_{2,i}$ . The height of each step is made proportional to the magnitude of desired platform velocity.

$$\dot{\tilde{p}}_{i,e}^y = (\alpha_v v^r g + \alpha_\omega \|\omega^r\|) \dot{y}_{2,i} \vec{h}_i \quad (5.12)$$

where  $\alpha_v$  and  $\alpha_\omega$  are scalar weighting parameters. Scaling step height relative to command parameters  $v^r$  and  $\omega^r$  has been seen in experimental studies to be more effective than using a fixed step-height for all gait configurations. Figures 22 and 23 show stepping patterns generated using the aggregate virtual-force foothold controller and CPG motion outputs during two and four-paced gaits, respectively, which achieve a forward velocity of  $v^r = 40 \frac{mm}{s}$ . The sequence of foot contacts made during each gait is enumerated in each figure. Red, green, blue, and cyan dots represent contacts made by the front-right, front-left, back-left and back-right feet, respectively.

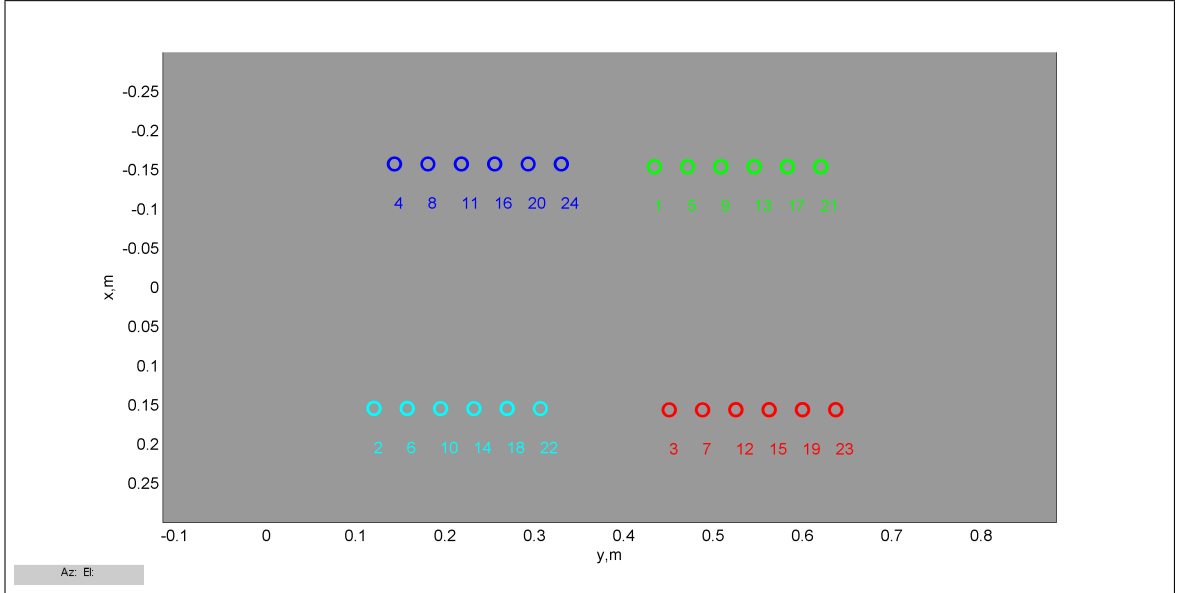


Figure 22: Stepping pattern generated using virtual-force foothold controller during two-pace gait sequence at  $v^r = 40 \frac{mm}{s}$ .

#### 5.4 ZMP Based Trunk-Placement Control

A modified Zero-Moment-Point (ZMP) based controller is utilized in positioning BlueFoot’s body during gaiting. In this context, the ZMP of the system is a set of state values for which the net-torque exerted upon the system, about the COG, is zero [59, 60]. Unlike [61, 62], which address ZMP-based control by considering the robot’s body as point-mass with massless limbs, this method takes into account the torque contribution of each non-supporting leg. Each leg in flight is considered as a series of point masses whose locations are computed using joint position feedback and trunk orientation estimates, in concert with robot’s forward kinematic model.

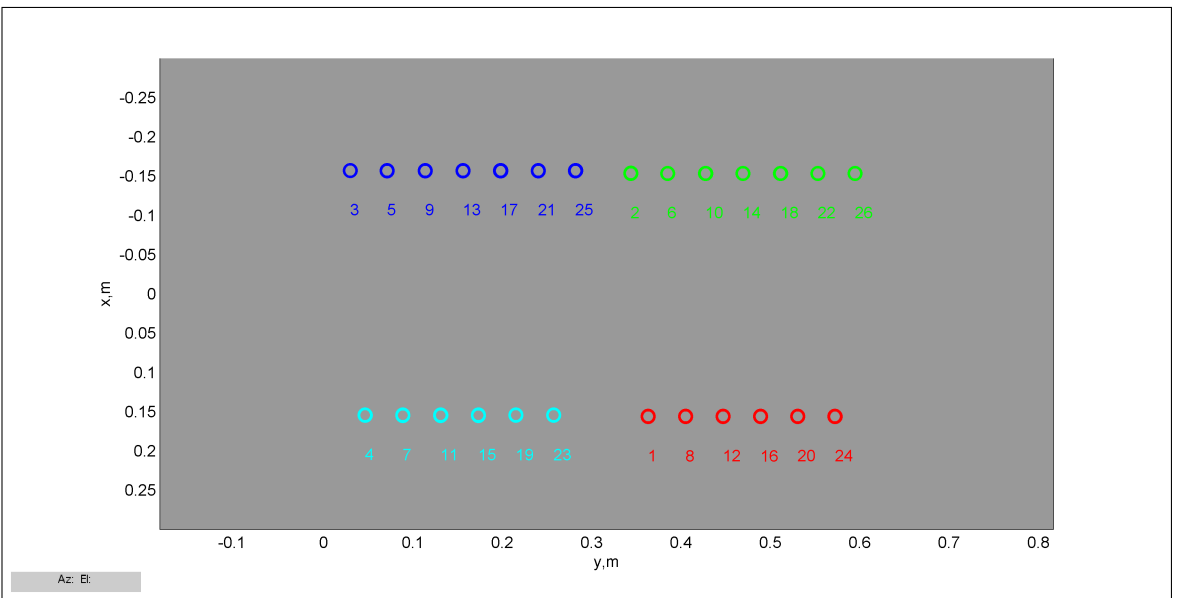


Figure 23: Stepping pattern generated using virtual-force foothold controller during four-pace gait sequence at  $v^r = 40 \frac{mm}{s}$ .

The ZMP approach is used to first calculate static ZMP configurations (*i.e.*,  $\ddot{p}_{COG} \approx 0$ ) at each time instance. The distance between the robot's COG and associated ZMP is incrementally minimized on-line by treating the ZMP as a mass-attractor and “pulling” a reference body position,  $p_b^{b',r}$ , towards the ZMP point at each update. This differs from approaches similar to [62] because these routines feature off-line, trunk trajectory design which aim to minimize deviations between the robot's COG and ZMP by creating an appropriate limit-cycle motion for the robot's trunk. These approaches typically utilize simplified, linearized models of the actual system about marginally-stable equilibrium points. To realize an adjustment of the robot's COG, towards the ZMP, BlueFoot's trunk position is modified during the execution of a gait. The trunk is controlled (and not individual feet) as it contributes most of the system's total mass and, thus, has the greatest influence over the location of the platform's COG. Restricting adjustments to the trunks translational states allow pre-planned foot trajectories to remain unmodified by the ZMP-control module during gait execution, thus decoupling foot-placement and body-placement control.

To incrementally compute the static ZMP of the platform, a measure of net-moment on the body of the platform must be known. The net-moment due to gravitational forces,  $\tau_{net}$ , is approximated using the locations of each link and joints as point-mass

loads. Hence,  $\tau_{net}$  is calculated as follows:

$$\tau_{net} = \left( \bar{p}_b^{b'} - \hat{p}_{COG}^{b'} \right) \times (\vec{g} m_b) + \tau_{legs} \quad (5.13)$$

where

$$\begin{aligned} \tau_{legs} &= \sum_{i=1}^4 (1 - \mu_i) \left( m_{i,e} p_{i,e}^{b'} + \sum_{j=1}^4 (m_{i,j}^J d_{i,j}^J + m_{i,j}^L d_{i,j}^L) \right) \times \vec{g} \\ d_{i,j}^J &= p_{i,j}^{b'} - \hat{p}_{COG}^{b'} \\ d_{i,j}^L &= \begin{cases} 0.5 (p_{i,j+1}^{b'} - p_{i,j}^{b'}) + p_{i,j}^{b'} - \hat{p}_{COG}^{b'} & \text{if } j < 4 \\ 0.5 (p_{i,e}^{b'} - p_{i,j}^{b'}) + p_{i,j}^{b'} - \hat{p}_{COG}^{b'} & \text{if } j = 4 \end{cases} \end{aligned}$$

with  $m_b$ ,  $m_{i,j}^J$ ,  $m_{i,j}^L$ ,  $m_{i,e}$  represent the mass of the main body; the mass of each joint; the mass of each link; the mass of each foot, respectively.  $\mu_i$  is included in the above formulation such that only stepping (non-contacting) legs contribute to  $\tau_{legs}$ . It should be noted that the superscript  $b'$  denotes that each particle considered in this controller is defined with respect to the robot-relative frame  $O_{b'}$  defined in Section 4.1. This allows the control routine to be performed without explicit knowledge of robot's absolute position in  $O_0$ . The estimated center of gravity in  $O_{b'}$ ,  $\hat{p}_{COG}^{b'}$ , is generated as follows:

$$\begin{aligned} \hat{p}_{COG}^{b'} &= \frac{1}{m_T} \left( m_b p_b^{b'} + \sum_{i=1}^4 \left( m_{i,e} p_{i,e}^{b'} + \sum_{j=1}^4 (m_{i,j}^J p_{i,j}^{b'} + m_{i,j}^L p_{i,j}^{b',L}) \right) \right) \\ p_{i,j}^{b'} &= \begin{cases} 0.5 (p_{i,j+1}^{b'} - p_{i,j}^{b'}) + p_{i,j}^{b'} & \text{if } j < 4 \\ 0.5 (p_{i,e}^{b'} - p_{i,j}^{b'}) + p_{i,j}^{b'} & \text{if } j = 4 \end{cases} \end{aligned} \quad (5.14)$$

where

$$m_T = m_b + \sum_{i=1}^4 \left( m_{i,e} + \sum_{j=1}^4 (m_{i,j}^J + m_{i,j}^L) \right) \quad (5.15)$$

Here, the the local COG of each linkage,  $p_{i,j}^{b'}$ , is assumed to be at the midpoint along the length of each link, half-way between two successive joints. Setting  $\tau_{net} = 0$ , (5.13) is manipulated to a derived solution for the ZMP as follows:

$$p_{ZMP}^{b'} = R_{zp} \left( \frac{\pi}{2} \right) \left( \frac{\|g\|}{m_b} \right) \tau_{legs} + \hat{p}_{COG}^{b'}. \quad (5.16)$$

Using  $p_{ZMP}^{b'}$ , the platform's posture is then updated using a virtual-force controller. Moreover,  $p_b^{b'}$  is to be controlled through  $p_b^r$  such that it is smoothly attracted to  $p_{ZMP}$ . The controller is given by

$$\dot{p}_b^r = P_{\vec{h}_i} \left( K_Z (p_{ZMP}^{b'} - p_b^{b'}) + K_F \frac{F_r}{m_b} \right) \quad (5.17)$$

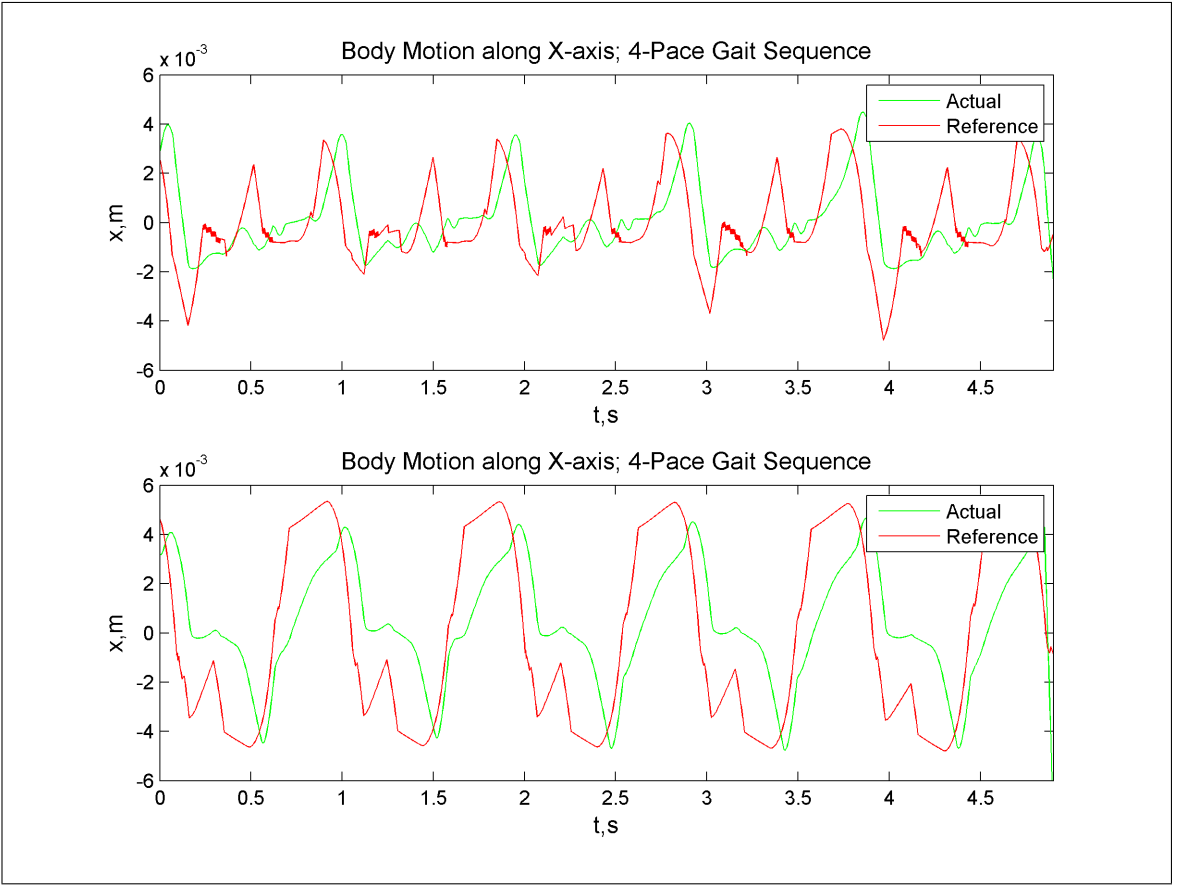


Figure 24: Body motion generated using ZMP controller during two-pace (*top*) and four-pace (*bottom*) gaiting sequence.

where

$$\begin{aligned}
 F_r &= \sum_{i=1}^4 e^{(k_l r_i^-)} + e^{(k_l r_i^+)} \\
 r_i^+ &= \|p_{i,e}^{b'} - p_b^{b'}\| - r_{max} \\
 r_i^- &= r_{min} - \|p_{i,e}^{b'} - p_b^{b'}\|
 \end{aligned}$$

and  $K_Z, K_F, K_c, K_\epsilon, k_l > 0$  and  $p_b^{b',r}$  is the reference body velocity.  $F_r$  is a boundary force added to ensure that the workspace of each manipulator, defined by the radii  $r_{min}$  and  $r_{max}$ , is not exceeded when the body is repositioned.  $k_l$  is picked to be adequately large such that this force is nearly zero when the body and foot positions comply with the local workspace of each leg, and large when the workspace is nearly compromised, forcing the placement of the body to comply with each leg workspace. Figure 24 shows a trajectory for the trunk position reference,  $p_b^{b',r}$ , and actual body trajectory,  $p_b^{b'}$  generated using

the aforementioned ZMP-based body-placement controller during a gait which achieves a forward velocity of  $v^r = 40 \frac{mm}{s}$ . Here, results are shown for the  $x$ -axis motion of the body. This is because during forward motion, the most significant alterations to the location of the body are seen along the  $x$ -axis.

## 5.5 Trunk Leveling via NARX-Network Learning Approach

Suppressing disturbances which enter a quadruped system during gaiting is a matter which requires special handling, given the the dynamical complexity of both the robot and its interactions with the environment. This complexity can be handled, in part, by a learning-based approach. This section will focus on the formulation of a learning controller used to reject disturbances from the orientation states of the trunk of a legged robot. Disturbance rejection from the trunk sub-system of a legged platform has practical significance when carrying a payload (such as cameras, optical systems, armaments, etc.) rigidly fixed to their main body. Disturbances are imparted upon the trunk during gaiting in two main ways:

1. instantaneous changes in force distribution when feet make and break contact with the ground
2. under-actuation that occurs during certain dynamic gaits. During dynamic gaits, such as trot gaits, the state of contact between the feet and the ground is changed often so as to prevent the walking robot from tipping past a recoverable configuration.

Additionally, these gaits feature the utilization of two or fewer legs to support the trunk at any given time, causing the system to enter an under-actuated state where the body is free to rock about the planted feet, as shown in Figure 25. To achieve disturbance rejection on the trunk orientation and to attain a fixed orientation, experimentation has been performed using a control methodology which utilizes a Nonlinear Autoregressive Neural Network with Exogenous inputs (NARX-NN) as part of an active compensation mechanism. The network is used to estimate the system dynamics and, further, predict periodic disturbances in an on-line fashion. The compensator is utilized to modify referential joint trajectories by way of a weighted sum between the original joint trajectories generated by the gaiting mechanism and a reference correction signal generated by the compensator.

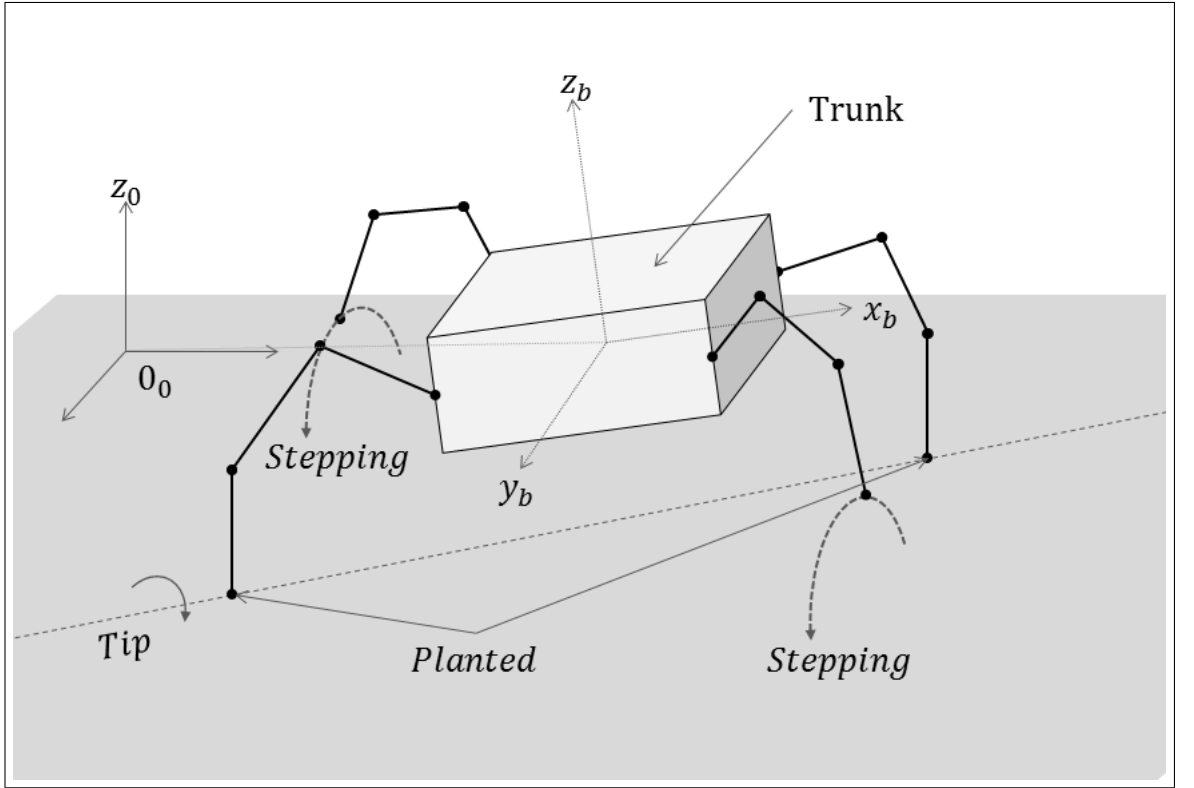


Figure 25: Quadruped tipping about planted feet.

### 5.5.1 NARX-Neural Network

Using a NARX-NN (introduced in Chapter I), the dynamical estimate  $\hat{\Phi}_k$  is generated as a prediction of the sampled system dynamics,  $\hat{\psi}_{k+1}$ . The relationship between  $\hat{\Phi}_k$  and the network prediction  $\hat{\psi}_{k+1}$  will be made clear in the description of the network training signal given in (5.19). The general input-output relationship of the NARX-NN predictor,  $\mathcal{N}$ , is described as follows:

$$\begin{aligned}\hat{\psi}_{k+1} &= \mathcal{N}(\hat{\Psi}_k^N, U_k^N) \\ \hat{\Psi}_k^N &= [\hat{\psi}_k, \hat{\psi}_{k-1}, \dots, \hat{\psi}_{k-N+1}] \\ U_k^N &= [u_k, u_{k-1}, \dots, u_{k-N+1}]\end{aligned}\tag{5.18}$$

where  $U_k^N$  and  $\hat{\Psi}_k^N$  are collections of  $N$  most recent samples of the network inputs,  $u_k$ , and the network output,  $\hat{\psi}_k$ , respectively. The NARX-NN input,  $u_k$ , represents a tuple  $u_k = (z_{1,k}, z_{2,k}, f_{ext,k})$  whose components are the arguments of  $\Phi$  at time instant  $k$ .

### 5.5.2 NARX-NN Training Regimen

The NARX-NN training signal is formulated to estimate  $\Phi_k$  from the system dynamics. By (4.21), it can be seen that  $\Phi_k$  can be estimated if  $z_{2,k+1}$  can be predicted. We consider the following target network prediction output,  $\psi_{k+1}$ , defined by:

$$\psi_{k+1} = \tau_k - \hat{M}_{1,k}(z_{2,k+1} - z_{2,k})\Delta_s^{-1} = \Phi_k - e_{2,k}^{\Delta_s}. \quad (5.19)$$

This training signal formulation assumes that  $\hat{M}_{1,k}$  represents  $M_{1,k}$  exactly, which is likely not the case given the system's complexity. In the absence of a well-modeled  $\hat{M}_{1,k}$ , a constant symmetric  $\hat{M}_{nom}$  will be picked such that  $\hat{M}_{1,k} = \hat{M}_{nom} \forall k$ .  $\hat{M}_{nom}$  has the following structure:

$$\hat{M}_{nom} = \begin{bmatrix} \hat{M}_{bb} & \hat{M}_{bq} \\ \hat{M}_{qb} & \hat{M}_{qq} \end{bmatrix} \quad (5.20)$$

where  $\hat{M}_{bb} \in \mathcal{R}^{6 \times 6}$ ,  $\hat{M}_{bq} = \hat{M}_{qb}^T \in \mathcal{R}^{6 \times 16}$ , and  $\hat{M}_{qq} \in \mathcal{R}^{16 \times 16}$ . It is particularly important that  $\hat{M}_{bq} \neq 0$  to reflect some degree of coupling between the joint states  $q$  and the trunk states  $p_b$  and  $\theta_b$ . In general, if  $\hat{M}_{nom}$  should be selected to reflect the *average* system mass matrix over the range of configurations,  $z_1$ , seen during gaiting. This approximation has shown to be adequate from our results, and depends on the assumption that changes in  $\hat{M}_{1,k}$  are small over the subset of state  $z_1$  experiences during a periodic gaiting sequence. Future improvements of this controller involve the formulation of a separate estimator for  $M(z_1)$ , or a control / learning scheme with no direct dependence on  $M(z_1)$ .

Since  $\hat{\psi}_{k+1}$  is non-causal, training is performed one time-step after a prediction is made using the input-output pair  $\hat{\psi}_k$  and  $\{\Psi_{k-1}^N, U_{k-1}^N\}$ . Note that  $\hat{\psi}_k$  can be calculated directly using (5.19) where all component signals are time-delayed by one time-step. Training can then be described by:

$$\psi_k \xrightarrow{BP(\gamma^{lr})} \mathcal{N}(\Psi_{k-1}^N, U_{k-1}^N) \quad (5.21)$$

where  $\gamma_{min}^{lr} < \gamma^{lr} < \gamma_{max}^{lr}$  is a learning rate adapted using a *bold-driver* update routine. Bold-driver learning-rate adaptation is a heuristic method for speeding up the rate of convergence of back-propagation training regimes [63, 64]. This  $\gamma^{lr}$  update law is parameterized by  $\beta \in (0, 1)$  and  $\zeta \in (0, 1)$  which are selected to specify the amount by which  $\gamma^{lr}$  increases or decreases per update, and  $\gamma_{min}^{lr}$  and  $\gamma_{max}^{lr}$  which are used to saturate  $\gamma^{lr}$ . The bold-driver scheme utilizes the current and previous mean-squared

network output error values ( $MSE_k$  and  $MSE_{k-1}$ , respectively) to adjust  $\gamma^{lr}$  as follows:

$$\gamma^{lr} \leftarrow \begin{cases} \gamma^{lr}(1 - \beta) & \text{if } MSE_k > MSE_{k-1} \\ \gamma^{lr}(1 + \zeta\beta), & \text{otherwise.} \end{cases} \quad (5.22)$$

Since network training is being performed on-line as an incremental routine, the effective mean-squared NARX-NN output error is low-passed by a factor  $\lambda \in (0, 1)$ . This update technique has been selected to ensure that outliers presented during training do not affect network learning updates as significantly as “nominal” training pairs. Network output error,  $e_{\mathcal{N},k}$ , and its associated MSE values are calculated after each prediction by:

$$\begin{aligned} e_{\mathcal{N},k} &= \hat{\psi}_k - \psi_k \\ MSE_k &\leftarrow \lambda \|e_{\mathcal{N},k}\|_2^2 + MSE_{k-1}(1 - \lambda). \end{aligned} \quad (5.23)$$

### 5.5.3 Compensator Output

The control scheme is first presented with respect to the servo input torques,  $\tau_{q,k}$ , and formulated to achieve a level trunk characterized by  $\theta_b = 0$ ,  $\dot{\theta}_b = 0$ . To formulate this controller, the dynamical sub-system which corresponds to the un-actuated trunk orientation states is isolated by:

$$\ddot{\theta}_b = \Gamma_1 M^{-1}(z_1)(\Gamma_2 \tau_q + \Phi) \quad (5.24)$$

where

$$\begin{aligned} \Gamma_1 &= [0_{3 \times 3}, I_{3 \times 3}, 0_{3 \times 16}] \\ \Gamma_2 &= [0_{16 \times 6}, I_{16 \times 16}]^T \end{aligned}$$

and  $\Gamma_2 \tau_q$  is equivalent to the original system input,  $\tau$ . In order to enforce a level platform with zero angular velocity, we seek a  $\tau_q$  which emulates the proportional-derivative (P.D.) control law:

$$\ddot{\theta}_b = -K_b \theta_b - K_d \dot{\theta}_b \quad (5.25)$$

where  $K_b$  and  $K_d$  are constant gain matrices. Using this P.D. law and (5.24), we propose a least-squares solution for  $\tau_q$  by:

$$\tau_q \approx -[\Gamma_1 M^{-1}(z_1) \Gamma_2]^\dagger \Gamma_1 M^{-1}(z_1)(\Phi + K_b \theta_b + K_d \dot{\theta}_b) \quad (5.26)$$

where  $[*]^\dagger$  denotes the Penrose-Moore pseudo-inverse of  $[*]$ . Replacing all dynamical terms with their associated discrete-time equivalents, and  $\Phi$  by the NARX-NN output  $\hat{\Phi}_k = \hat{\psi}_{k+1}$ , we apply (5.26) to arrive at the following required joint torque estimate:

$$\hat{\tau}_{q,k} = -\left[\Gamma_1 \hat{M}_{1,k}^{-1} \Gamma_2\right]^\dagger \Gamma_1 \hat{M}_{1,k}^{-1} (\hat{\psi}_{k+1} + K_b \theta_{b,k} + K_d \dot{\theta}_{b,k}) \quad (5.27)$$

where  $\theta_{b,k}$  and  $\dot{\theta}_{b,k}$  are samples of angular trunk position and rate, respectively.

Using the joint controller dynamics presented in (4.22) and the estimate  $\hat{\tau}_{q,k}$ , we can formulate a reference-trajectory correction which is used to alter the joint reference positions,  $q_k^r$ . Moreover, the corrected reference position,  $q_{1,k}^{r,*}$  is generated such that the estimated output torque  $\hat{\tau}_{q,k}$  is attained by each joint controller. This joint-reference compensator output is defined using (5.27) as follows:

$$q_{1,k}^{r,*} = k_s^{-1}(\hat{\tau}_{q,k}) + q_{1,k}. \quad (5.28)$$

The correction signal,  $q_k^{r,*}$ , is combined with the original gaiting trajectory signal,  $q_k^r$ , as a weighted sum to form a compensated joint control reference signal,  $\tilde{q}_k^r$ , defined by:

$$\tilde{q}_k^r \leftarrow (1 - \alpha)q_k^r + \alpha(q_k^{r,*}) \quad (5.29)$$

where  $\alpha \in (0, 1)$  is a uniform mixing parameter. The parameter  $\alpha$  must be tuned with respect to the stability margins of the gait being compensated. The resultant  $\tilde{q}_k^r$  is then applied to each joint controller in place of the original reference signal,  $q_k^r$ , generated by the gait controller. Selection of the parameter  $\alpha$  is crucial for achieving good performance.

#### 5.5.4 NARX-NN Implementation

The NARX-NN was implemented as a collection of C code functions. These functions make use of the Fast Artificial Neural Network (FANN) library, which provides structures and interfaces for implementing fully-configurable, feed-forward neural networks natively implemented in C [65]. This library was selected for the implementation of the feed-forward portion of the NARX network for its speed and flexibility.

#### 5.5.5 NARX-NN Compensator Results

The NARX-NN compensator has been tested, exclusively, in simulation and has been applied to the quadruped as it executes a stable CPG-driven trot gait depicted in Figure 25. In these trials, gaiting frequency is adjusted accordingly to achieve

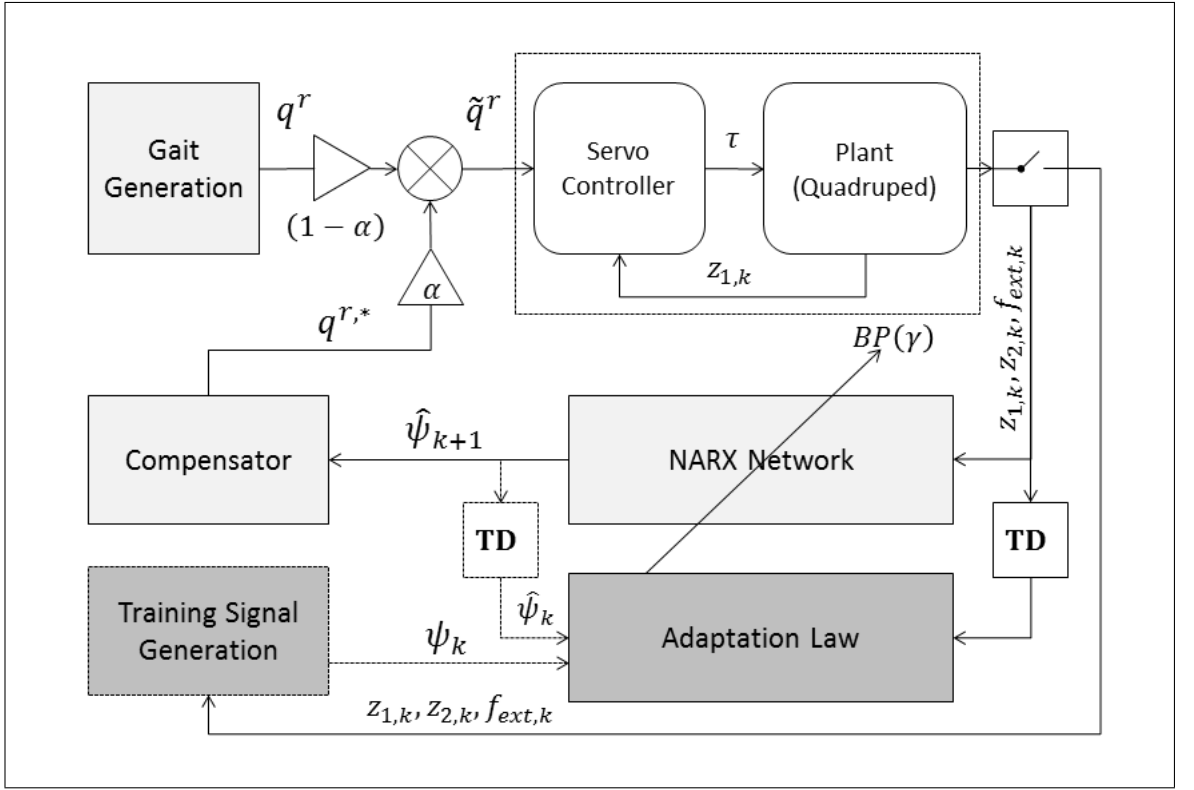


Figure 26: Full system diagram with NARX-NN compensator mechanism.

particular forward speeds. NARX-NN parameters are fixed for all trials with learning-rate parameters set to  $\beta = 0.0001$ ,  $\zeta = 0.0005$  and  $\lambda = 0.01$ . The NARX-Network is configured with two hidden layers containing 50 neurons each. Each input and hidden-layer neuron is modeled using a symmetric sigmoid activation function. Output layer neurons are modeled using linear activation functions to avoid output-scaling saturation issues. Figure 27 exemplifies the convergence of the NARX-NN prediction error when the platform executes a gait at  $100 \frac{mm}{s}$  with  $\alpha = 0.35$ .

Contact forces,  $f_{i,ext}$ , are handled in the simulated implementation as they would be on the real BlueFoot platform. This handling method accounts for the absence of true force-torque sensors on each of BlueFoot's feet and, instead, makes use of the system's binary foot-contact sensors, in conjunction with the IMU. Although contact forces on each foot are accessible in simulation, the force at each foot is estimated using a combination of trunk 3-axis accelerometers and foot contact data. Assuming a rigid system and a uniform distribution of forces to each planted foot, a rough estimate of

the force applied to each  $i^{th}$  planted foot,  $\hat{f}_i$ , can be generated by:

$$\hat{f}_i = m_T \mu_i (\ddot{p}_b - \vec{g}) / \sum_{j=1}^4 \mu_j \quad (5.30)$$

where  $m_T$  represents the total system mass;  $\mu_i \in \{0, 1\}$  is the contact state of the  $i^{th}$  foot (a value  $\mu_i = 1$  represents contact);  $\vec{g}$  is the gravity vector; and  $\ddot{p}_b$  is the trunk acceleration in the world frame. Ideally, the measurement of  $f_i$  would be obtained via a 3-axis force-torque sensor placed at each foot.

All simulated trials are performed over a period of 60 seconds each. During the first 10 seconds of each simulation, the robot moves from sitting position to a standing position and initiates walking. During each simulation period, the NARX-NN compensator is activated (not training) and deactivated (training) every 10 seconds. Figures 28, 29 and 30 depict an initial set of simulation results showing the effect of varying the mixing parameter  $\alpha \in \{0.125, 0.25, 0.35\}$ . For all such trials, the robot performs a trot-gait which achieves a forward speed of  $60 \frac{mm}{s}$ . It is expected that as  $\alpha$  increases, the compensator will have greater authority over trunk stabilization. From these results, we observe that for all  $\alpha$ , disturbance magnitude is decreased to some extent. However, for smaller  $\alpha$ , the compensator is less effectual due to the fact that it has less authority over joint reference signals. From the results in Figure 29, it is shown that the compensator improves pitch stability by more than roughly 50% and roll stability by more than 60%. Figure 31 shows the compensator's performance at higher gaiting speeds of  $80 \frac{mm}{s}$  and  $100 \frac{mm}{s}$ . Here the controller improves both pitch and roll by nearly 50% and 40% of the uncompensated signal magnitude, respectively.

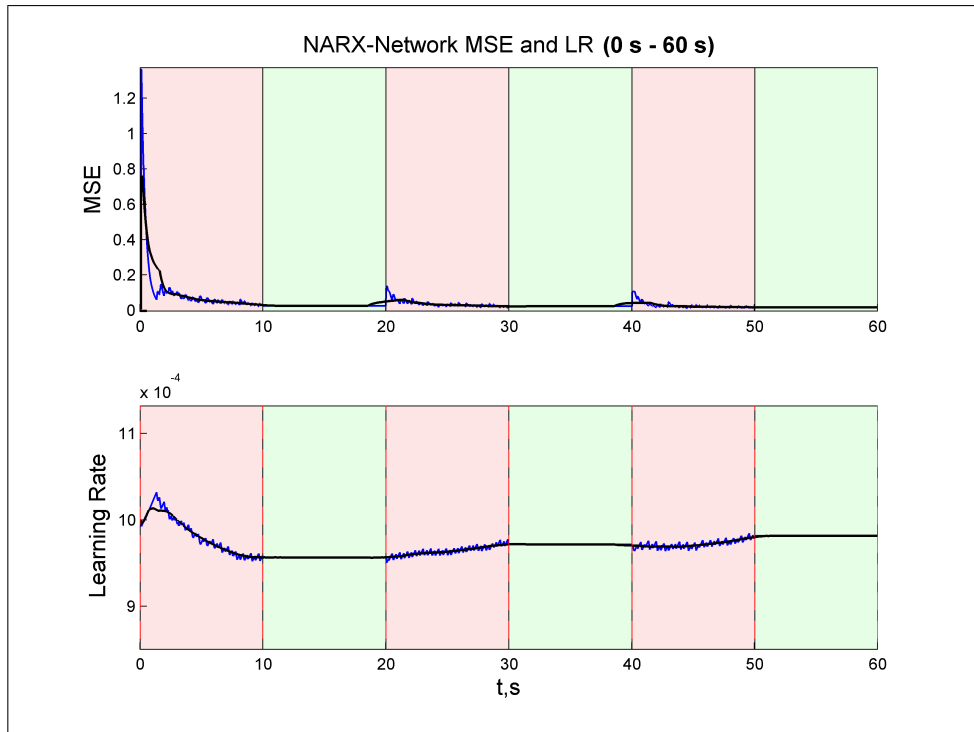


Figure 27: NARX Network MSE convergence for trial shown in Figure 32

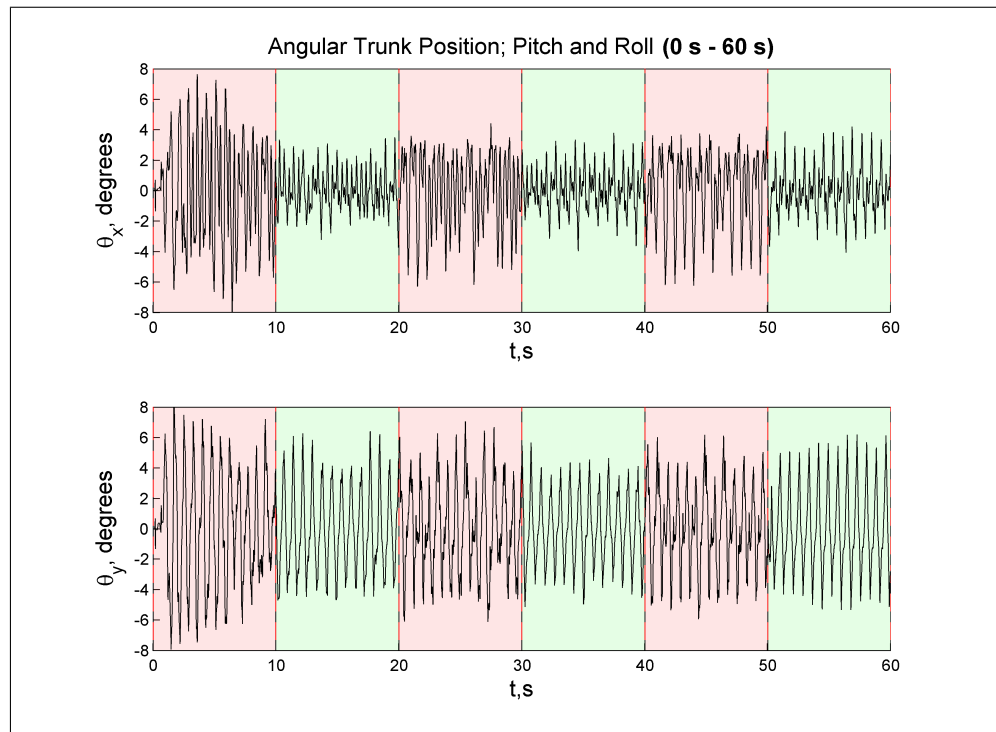


Figure 28: Trunk orientation during  $60 \frac{mm}{s}$  gait with  $\alpha = 0.125$ .

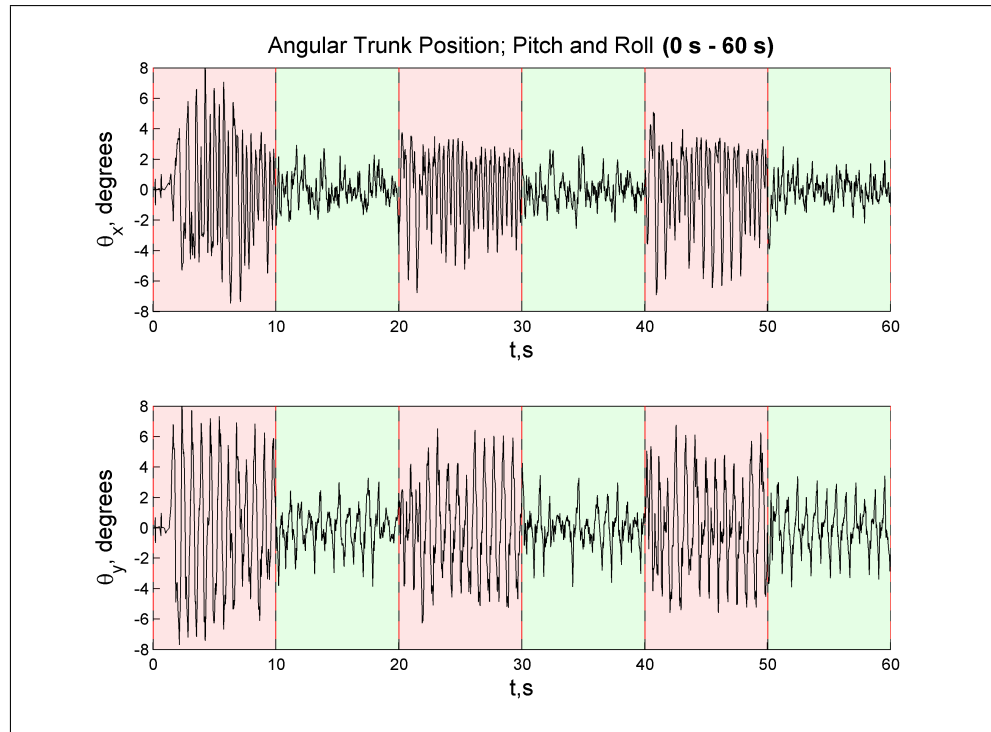


Figure 29: Trunk orientation during  $60 \frac{\text{mm}}{\text{s}}$  gait with  $\alpha = 0.250$ .

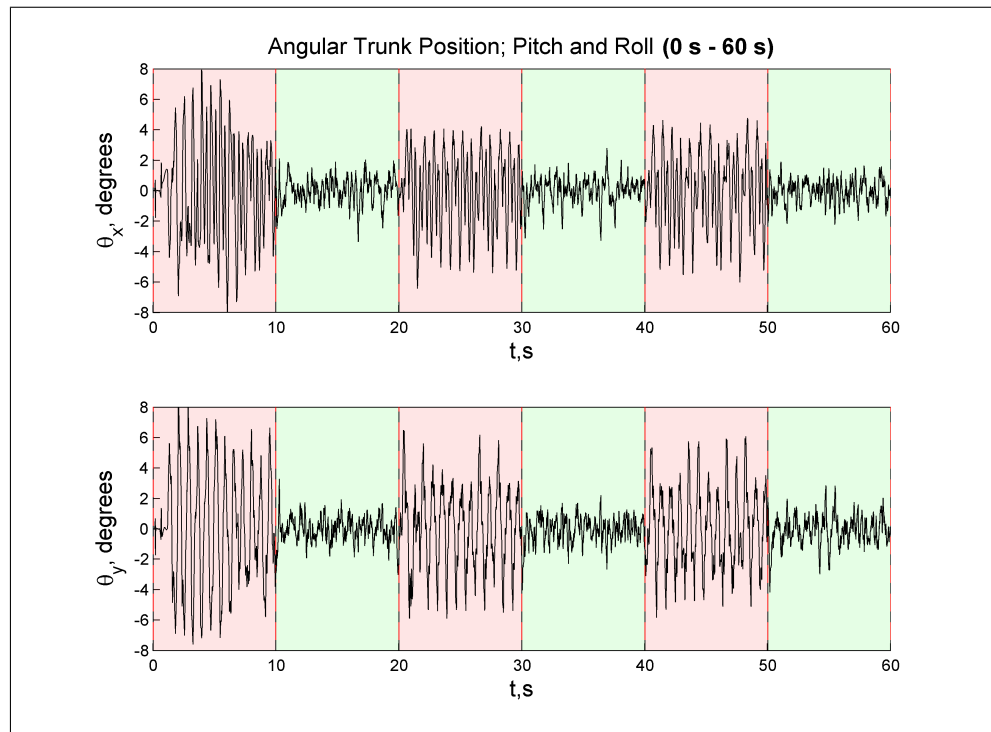


Figure 30: Trunk orientation during  $60 \frac{\text{mm}}{\text{s}}$  gait with  $\alpha = 0.350$ .

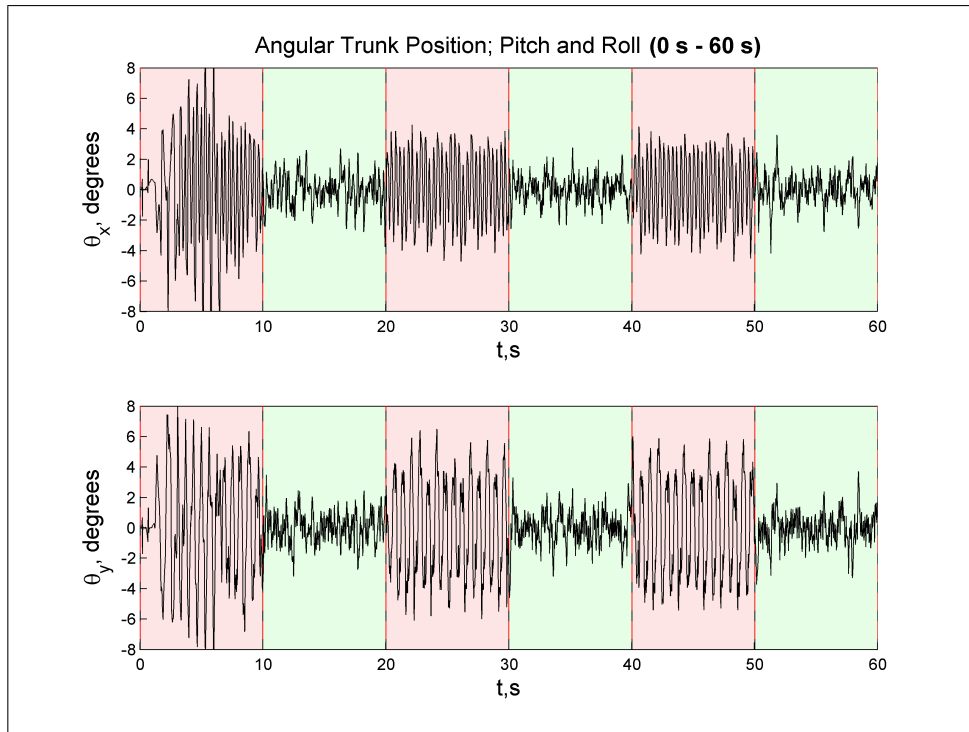


Figure 31: Trunk orientation during  $80 \frac{\text{mm}}{\text{s}}$  gait with mixing parameter set to  $\alpha = 0.35$

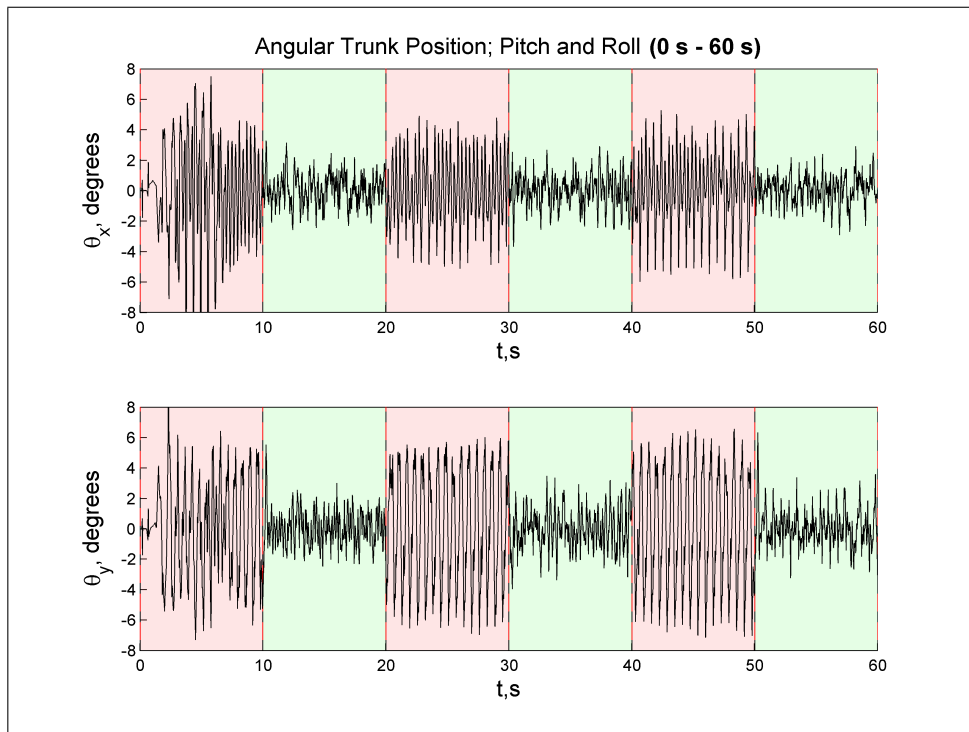


Figure 32: Trunk orientation during  $100 \frac{\text{mm}}{\text{s}}$  gait with  $\alpha = 0.35$

## CHAPTER VI

### Perception and Navigation

#### 6.1 Flatland navigation and goal (feature) tracking

The BlueFoot robot is operated using a hybrid, potential-field control scheme for obstacle avoidance during navigation over flatland. Camera-based feature tracking has been incorporated into this navigation scheme to allow for dynamic object tracking and aid in the aversion of local minima. This hybrid navigation routine administers commands to the robot's gaiting controller using two main parameters,  $v^r$  and  $\omega^r$ , which represent forward velocity and turning rate of the platform with respect to the robot's trunk frame  $O_b$ . An explanation of how these parameters are used to influence BlueFoot's gait control and foot-placement is covered in Section 5.3. During navigation, the pitch of the trunk,  $\theta_{b,x}$  is also controlled via its respective reference signal,  $\theta_{b,x}^r$ , using an outer-loop proportional control scheme. Control over trunk pitch allows for additional articulation of the LIDAR and camera sensors mounted to BlueFoot's head (trunk) while tracking features. Trunk articulation control is also paramount for composing 3D point clouds from LIDAR scans, as will be described later in this chapter.

Namely, BlueFoot's primary navigation mechanism fuses navigation reference commands generated from two separate control laws: a LIDAR-based potential-fields controller; and a camera-based visual servoing controller. The collective navigation law is used as a *wandering* mechanism which would normally be employed as a first-level measure during situations where the robot has no information about its environment (*i.e.*, environmental map data, or knowledge of landmark locations) *a priori*. This section will first describe the potential-fields portion of BlueFoot's navigation algorithm, which utilizes only LIDAR sensor data. The efficacy of this navigation mechanism will be supported with results from simulated trials. The incorporation of processed camera data will then be detailed to complete the description of the full navigation controller. Associated results will be presented from a real-world trial.

### 6.1.1 LIDAR-based Potential-Fields Algorithm

The potential-fields portion of BlueFoot’s navigation routines takes planar LIDAR scans as an input and generates a set of navigation outputs,  $\vec{u}_L^r \in \mathcal{R}^3$ , which represents a direction of travel relative to the LIDAR frame,  $O_L$ , and  $P_L$ , which represents a total positive (attractive) potential. Each point from a LIDAR scan is mapped to a corresponding scalar *potential* which is used to influence the commanded direction of travel. Given a LIDAR scan,  $S^L$ , with 2D scan points,  $x_i^L \in S^L$ , relative to the LIDAR’s local coordinate frame  $O_L$ , command elements are generated using a potential function  $\{f(x) : \mathcal{R}^3 \rightarrow \mathcal{R}^1\}$ , and a biasing function,  $\{g_\psi(x) : \mathcal{R}^3 \rightarrow \mathcal{R}^1\}$ , as follows:

$$\begin{aligned}\vec{u}_L^r &= \sum_{x_i^L \in S} g_\psi(x_i^L) f(x_i^L) \frac{x_i^L}{\|x_i^L\|} \\ P_L &= \alpha_p \sum_{x_i^L \in S^L} g_\psi(x_i^L) f(x_i^L) U(f(x_i^L))\end{aligned}\quad (6.1)$$

A piecewise potential function, defined in (6.2), is used in BlueFoot’s navigation scheme. This function is designed to repel the platform from objects which are closer to the robot than some minimum distance,  $d_{min}$ , and attract the robot toward objects which are further away. The form of this potential function was guided by several candidate force-field functions presented in [42]. Without explicitly directing the robot towards known goals, the intention of (6.2) is to draw the robot towards long apertures, such as corridors or openings, and away from close-by obstructions. It is written as follows:

$$\begin{aligned}\Delta d &\equiv \|x\| - d_{min} \\ f(x) &= \begin{cases} -\lambda_{c,1} (\Delta d)^2 & \text{if } \Delta d < 0 \\ (\Delta d) \left(1 - e^{-\lambda_{c,2}(\Delta d)^2}\right) & \text{else} \end{cases}\end{aligned}\quad (6.2)$$

where  $\lambda_{c,1} > 0$  and  $\lambda_{c,2} > 0$  are tuning parameters used to specify the output range and sensitivity of the potential function output with respect to  $\Delta d$ , respectively. It can be observed that this potential function exhibits  $f(x) < 0$  when  $\|x\| < d_{min}$  and vice-versa, thus achieving the desired attractive and repulsive characteristics. Namely, this potential function attracts the robot to points which are generally much further away from the robot, and applies *strong* repulsive forces only when obstacles come within close range of the platform. These characteristics offer a higher propensity for exploration when the area being navigated is very spacious (with few obstacles in view),

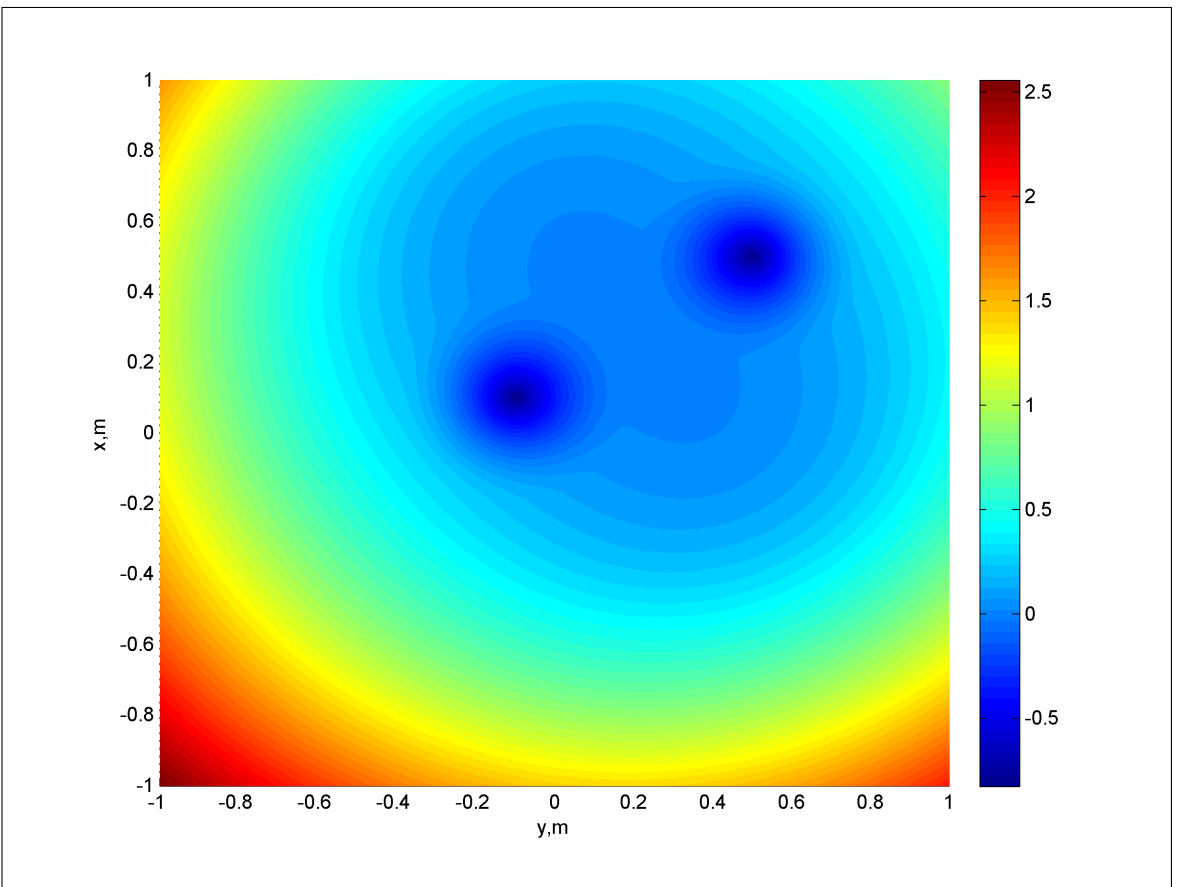


Figure 33: Potential-field around environmental obstacles.

while incurring tighter navigation around obstacles which are nearby. Moreover, the robot will tend not to make needless deviations in open spaces if potential obstructions are well out of range.

Figure 33 shows a visualization of the potential field,  $f(x)$ , generated around two cylindrical obstacles (located at  $(0.5, 0.1)$  m and  $(0.1, -0.1)$  m) in a 2-by-2 meter area about the robot. It is important to note the largely negative potential values around the neighborhood of each obstacle, which result in repulsive force contributions.

The biasing function  $g_\psi(x)$  is used to weight the effect of individual scan points with respect to their relative angular location about the  $z$ -axis of  $O_L$ .  $g_\psi(x)$  is parametrized by  $\psi > 0$ , which defines a symmetric angular window. In (6.1),  $g_\psi(x)$  is selected as

follows:

$$\begin{aligned}\text{ang}(x) &= \tan^{-1} \left( \frac{[x]_x}{[x]_y} \right) \\ g_\psi(x) &= \begin{cases} \left( 1 - \left\| \frac{\text{ang}(x)}{\psi} \right\| \right)^{\alpha_g} & \text{ang}(x) < \psi \\ 0 & \text{otherwise.} \end{cases}\end{aligned}\quad (6.3)$$

where  $[x]_x$  and  $[x]_y$  are the  $x$ -axis and  $y$ -axis coordinates of the vector argument  $x \in \mathcal{R}^3$ ; and  $\alpha_g \leq 1$  such that  $g_\psi(x)$  is concave with respect to  $\alpha_g$ . This function is used to give priority to points which fall forward of the robot and within the aforementioned angular window (of width  $2\psi$ ) centered at the  $y$ -axis which emanates from  $O_L$ . To note: the  $y$ -axis of the frame  $O_L$  always points in the direction of the robot's forward heading and emanates from the front of the LIDAR head. The reasoning for incorporating  $g_\psi(x)$  is as follows: if the robot is heading forward and detects close-by obstructions at its sides (*i.e.*, at some angular location with an angular magnitude that is greater than or equal to  $\|\frac{\pi}{2}\|$ ), it is not necessary to perform maneuvers to avoid these obstacles as they will not impede upon the robot's immediate forward motion, so long as they are sufficiently far from the robot's immediate workspace. The same is true for obstacles which are behind the robot, which will be completely disregarded according to the definition of  $g_\psi(x)$  provided above. Only if the robot faces an obstacle which is directly ahead of it should it turn away to avert a potential collision. Thus, the parameter  $\alpha_g$  in  $g_\psi(x)$  is tuned to adjust the amount to which points are “ignored” with respect to their angular distance from the front of the LIDAR head.

Finally, outputs of the potential field algorithm are mapped into forward and turning rate commands,  $v_L^r$  and  $\omega_L^r$ , respectively, by the following control scheme:

$$\begin{aligned}\theta_L^r &= \tan^{-1} \left( \frac{[\vec{u}_L^r]_x}{[\vec{u}_L^r]_y} \right) \\ \dot{v}_L^r &= \beta_v (P_L + v_{L,min}^r - v_L^r) \\ \dot{\omega}_L^r &= \beta_\omega \left( \left( \frac{\omega_L^{r,max}}{\pi} \right) (\theta_L^r - \theta_{b,z}) - \omega_L^r \right)\end{aligned}\quad (6.4)$$

where  $\beta_v$  and  $\beta_\omega$  are proportional-gain tuning parameters;  $v_{L,min}^r > 0$  is a small, minimum velocity used to prevent the robot from getting stuck in local minima; and  $\theta_{b,z}$  is the robot's yaw in  $O_0$ . The parameters  $\beta_v$  and  $\beta_\omega$  can be viewed as *update-inertias*, as they directly effect the influence of immediate commands on the overall forward velocity and turning rate of the robot. Furthermore, these gains can be used to low-pass updates

to navigation parameters so as to remove jitter caused by degenerate LIDAR scans or sensor noise.

### 6.1.2 Simulated Potential-Fields Navigation Results

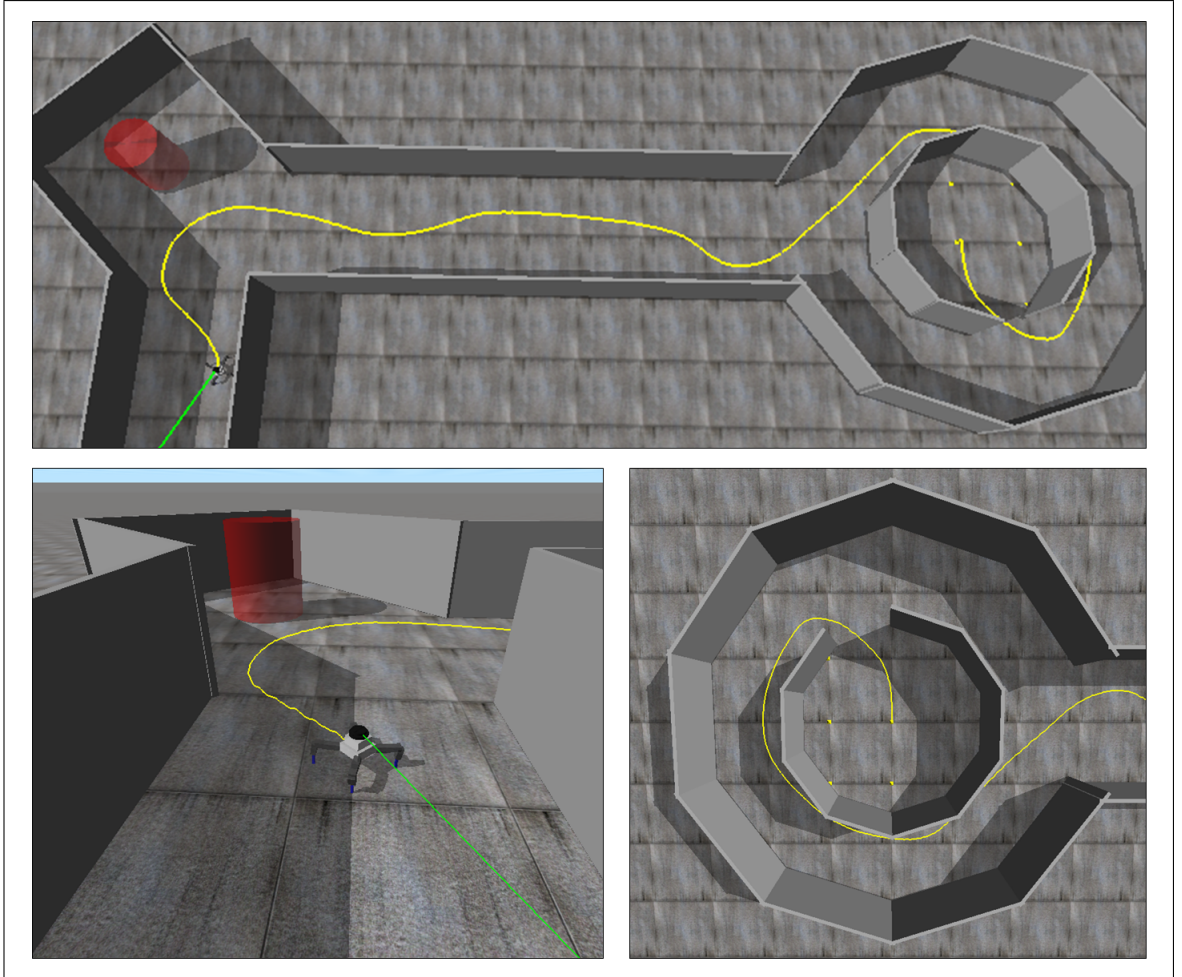


Figure 34: Path (shown in yellow) taken by robot through a simulated set of rooms and halls using the LIDAR-based potential-fields navigation scheme.

Figure 34 shows the path resulting from a simulated trial in which the BlueFoot robot autonomously wandered through an environment, consisting of a room and several long corridors, using the described potential-fields mechanism. The simulated robot's trajectory is marked in yellow and shows that the robot was able to successfully navigate its immediate environment while avoiding collisions with the surrounding walls. Notably, the simulated robot naturally avoided smaller out-cove regions, which were mostly filled by cylindrical obstacles. This is because these regions had overwhelmingly

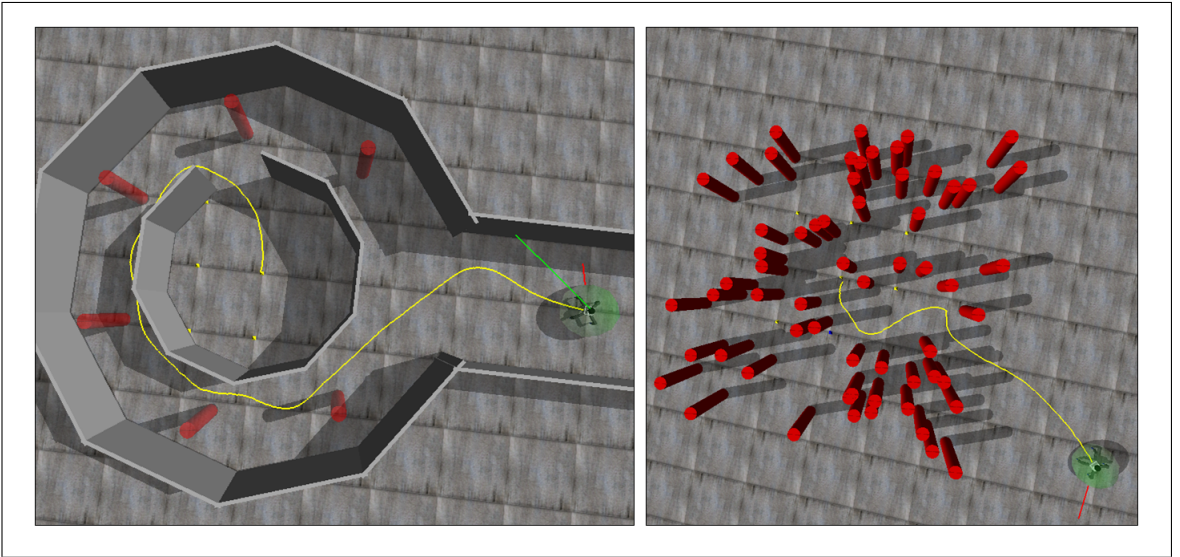


Figure 35: Path (shown in yellow) taken by robot through a simulated set of rooms and obstacles.

lower potential relative to the longer corridor regions which were detected in the same immediate LIDAR frames. A second set of results is shown in Figure 35 which highlights the robot’s performance in environments additional obstacles. Likewise, the robot exhibits the desired obstacle-aversion performance using the potential-fields algorithm described. In both simulated trials, navigation parameters are set as follows:  $\alpha_g = 0.25$ ,  $\psi = \frac{\pi}{2}$ ,  $d_{min} = 0.5$  m,  $\lambda_{c,1} = 0.1$ ,  $\lambda_{c,2} = 10.0$ ,  $v_{L,min}^r = 0.010 \frac{\text{mm}}{\text{s}}$   $\omega_{L,max}^r = 0.400 \frac{\text{rad}}{\text{s}}$  and  $\beta_v = \beta_\omega = 0.1$ .

### 6.1.3 Incorporation of Camera-based Feature Tracking

Camera-based goal tracking is used in conjunction with the aforementioned potential-fields navigation scheme to move the platform through an environment while dynamically tracking targets which come into view of its camera. In this case, targets take the form of features extracted from acquired images. The robot is guided towards these features using a visual-serving approach.

Trackable camera features can be generated in a variety of ways. For the purpose of BlueFoot’s navigation, objects with distinct shapes or color have been chosen for tracking so that shape and blob detection algorithms can be employed to detect the relative positions of these features in BlueFoot’s camera view. Namely, Hough Transform-based shape detection algorithms and color-blob detection algorithms from the Open Computer Vision library (OpenCV) are employed for the purpose of feature detection [48].

Once detected, points representing the centers of each feature, relative to the 2D camera frame, are mapped into forward velocity and turning rate commands. These commands are used to control the robot such that the center of the detected feature is aligned with the center of each image fame. These camera-based commands are then mixed with the outputs of the potential-fields controller as a weighted sum to form a hybrid navigation control law.

The visual-servoing approach to be described is agnostic of the type of feature being tracked. Namely, this approach relies on the relative position of the center of each feature, represented as a pixel-position,  $p_{Im} = [u, v]^T \in \mathbb{Z}^2$  in the 2D image frame,  $O_{Im}$ , and a relative size,  $r$ , measured in pixels. In the case of circular features, for example,  $r$  represents the radius of the detected circle. For color-blob features,  $r$  represents the radius of a circle which fully inscribes the colored object.

For the purpose of target tracking, it is desired that the robot's forward speed be controlled proportionally to the robot's relative closeness to the object of interest. A measure of closeness is determined from the value  $r$  associated with a particular feature. Namely, it is desired that the robot stops when it becomes *close enough* to the target object, and faster towards the feature when it is in sight, but further away. This control law is imposed to prevent the robot from crashing into the target being tracked. The position of a feature's center is used to control the robot's turning rate, as well as the commanded pitch of the robot's trunk,  $\theta_{b,x}^r$ . Trunk articulation important during feature tracking routing as it aids in keeping the tracked-target objects centered in the image frame. Provided that the target is moving slower than the what the system can track, this will ensure the target remains in sight at all times.

A separate set of navigation commands,  $v_C^r$  and  $\omega_C^r$ ; and an additional body-pitching command,  $\theta_{b,x}^r$ , are generated from an extracted feature location,  $p_{Im} = [u, v]^T$  (in the image frame  $O_{Im}$ ) as follows:

$$\begin{aligned} v_C^r &= v_C^{r,max} \left( 1 - e^{-c_r(r-r_{min})^2} \right) \\ \omega_C^r &= \omega_C^{r,max} \left( \frac{w_{Im} - 2u}{w_{Im}} \right) \\ \theta_{b,x}^r &= \theta_{b,x}^{r,max} \left( \frac{2v - h_{Im}}{h_{Im}} \right) \end{aligned} \quad (6.5)$$

where  $v_C^{r,max}$ ,  $\omega_C^{r,max}$  and  $\theta_{b,x}^{r,max}$  are the maximum magnitudes of forward velocity, turning rate, and body-pitching commands, respectively;  $c_r$  is a sensitivity parameter;  $r_{min}$  defines a minimum feature size which will result in the administration of a zero velocity

command,  $v_C^{r,\max} = 0$ , to the platform; and  $w_{Im}$  and  $h_{Im}$  define the width and height, respectively, of the image being processed. Having now established a formulation for how a single, distinct, feature is used to guide the platform towards a target, a means of fusing the LIDAR-based command signals and the camera-based command signals will be defined.

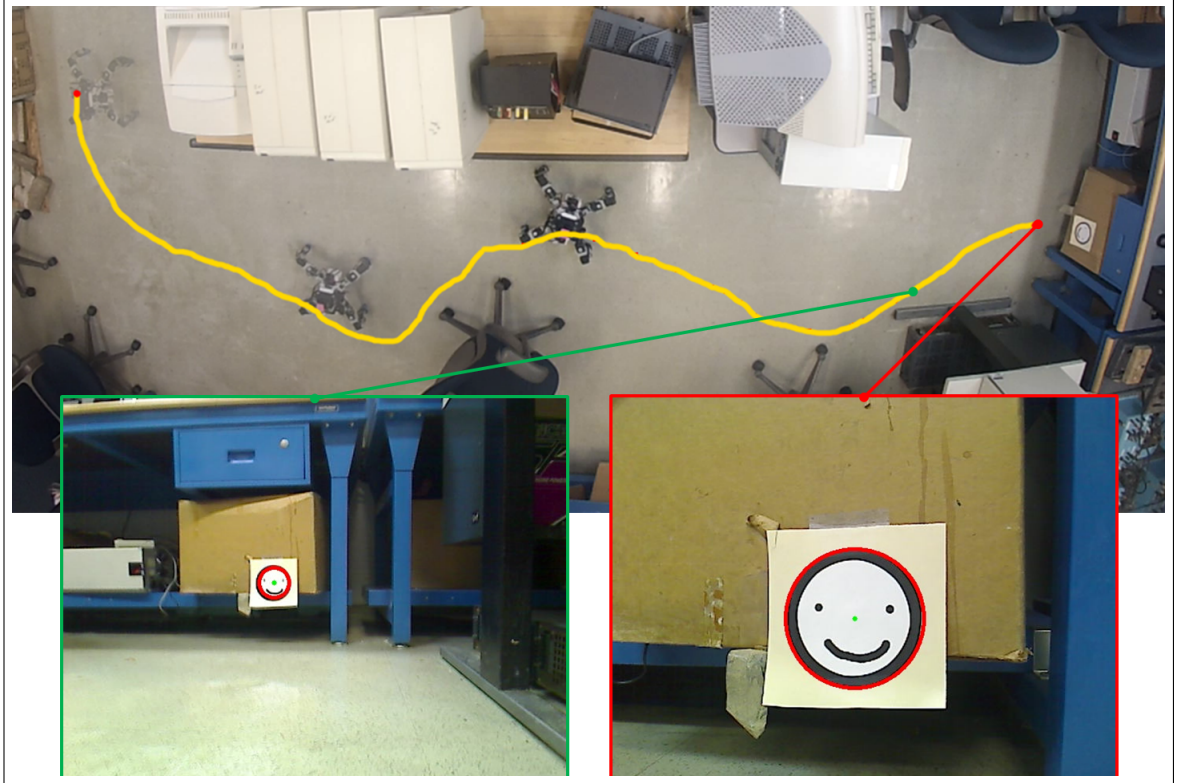


Figure 36: Path (shown in yellow) taken by robot through a real-world lab setting showing the robot’s view of the goal marker.

The composition of this hybrid command technique is motivated by two related subtasks:

1. to use the potential-fields algorithm during a wandering phase, when a target object is not in sight and
2. to guide the robot safely towards a target once in sight.

Moreover, camera-based tracking commands will have a greater influence on system navigation (through the variables  $v^r$  and  $\omega^r$ ) as the platform becomes closer to the desired target. A straight-forward way to achieve this is to use the relative size,  $r$ ,

of tracked features in the image frame, as will be described. With this in mind, a command-mixing scheme is defined as follows:

$$v(r) \equiv \begin{cases} e^{-c_{mix}(r-r_{mix})^2} & \text{if } r < r_{mix} \\ 1 & \text{else} \end{cases}$$

$$\begin{bmatrix} v^r \\ \omega^r \end{bmatrix} = v(r) \begin{bmatrix} v_C^r \\ \omega_C^r \end{bmatrix} + (1 - v(r)) \begin{bmatrix} v_L^r \\ \omega_L^r \end{bmatrix} \quad (6.6)$$

where  $c_{mix}$  is a sensitivity parameter; and  $r_{mix}$  defines a registered feature size which will cause the robot shift full priority to the camera-based navigation scheme. The reasoning for such an approach hinges on the assumption that when the platform is further away from a goal, there is a higher probability that it will encounter an obstacle. Conversely, when the goal becomes closer to the platform, it is assumed that the number of obstacles between the robot and the target is small, making it safer to promote the importance of reaching the target in sight. It is defined that if a feature is not visible within the current view of the camera, then  $r = 0$ .

Figure 36 shows the robot’s path through a real-world environment. In this trial, the robot is setup to detect a circular target marker which is placed such that it will fall into the robot’s gaze. The efficacy of this navigation scheme is highlighted, particularly, when the robot successfully rounds a chair in its way. Additionally, the robot successfully detects and reaches a target marker. The robot’s view of the target marker from further away and upon reaching the target are also shown in this figure. In each image, the perimeter and center of the target marker are highlighted to show the feature characteristics determined by the robot.

## 6.2 Towards Rough Terrain Navigation

### 6.2.1 Terrain Mapping from 2D scans

The BlueFoot platform composes 3D point clouds from a series of 2D LIDAR scans and associated trunk orientation estimates,  $\hat{\theta}_b$ , which are generated using a calibrated EKF routine. LIDAR articulation is achieved by slowly pitching the trunk over an angular range  $\theta_{b,x} \in [-\theta_{s,min}, \theta_{s,max}]$  while keeping the platform’s feet planted. The angular trajectory of  $\theta_{b,x}$  is discretized into  $K$  divisions, which defines the number scan-levels used in composing a 3D cloud, and further, an angular scan resolution about the  $x$ -axis. The rate of scan completion is dependent upon the spinning rate of the LIDAR.

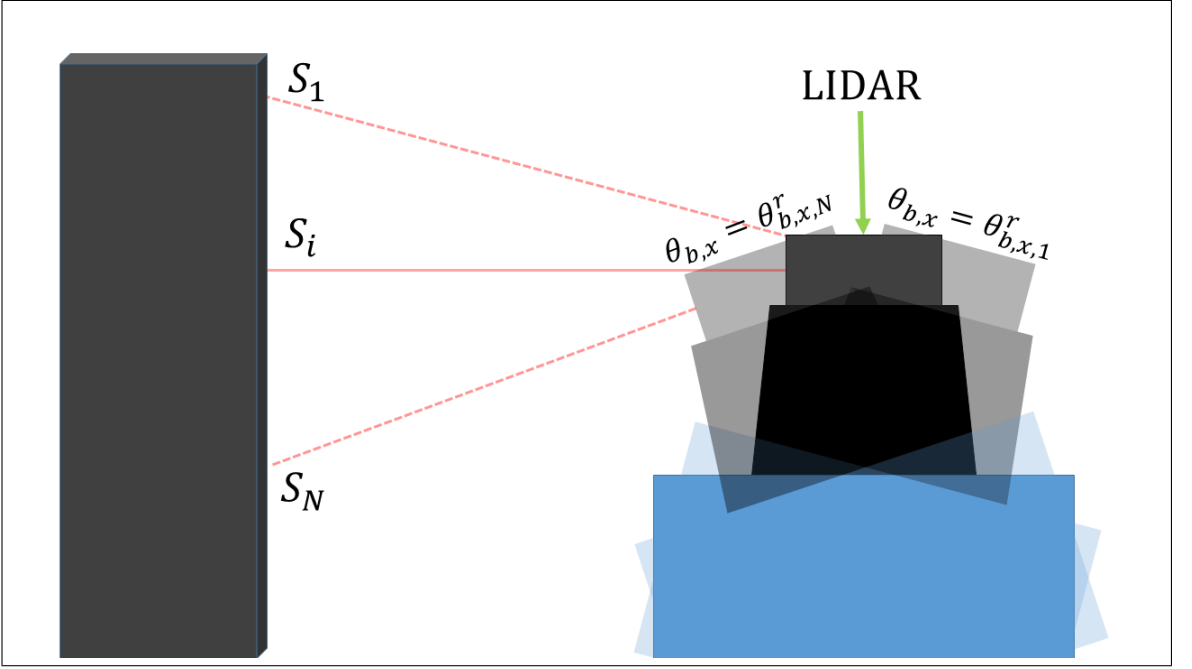


Figure 37: LIDAR swept over a range of angles,  $\theta_{b,x} \in [\theta_{b,x,1}^r, \theta_{b,x,N}^r]$ .

Furthermore, the pitch of the trunk is controlled during a scanning routine as follows:

$$\begin{aligned}\theta_{b,x,k}^* &= (\theta_{s,max} - \theta_{s,min}) \left( \frac{k}{K} \right) + \theta_{s,min} \\ \dot{\theta}_{b,x}^r &= \alpha_\theta (\theta_{b,x,k}^* - \hat{\theta}_{b,x}) \\ \forall k &\in \{1, \dots, K\}\end{aligned}\tag{6.7}$$

where  $k$  is a step-counter which is incremented each time the LIDAR completes a full scan cycle; and  $\alpha_\theta$  is a scalar, proportional gain factor. Given this formulation, the approximate rate of completion for a full 3D-scan,  $\tilde{f}_{scan}$ , is as follows:

$$\tilde{f}_{scan} \approx \frac{1}{K} \frac{\Delta\theta_L}{\omega_L} \tag{6.8}$$

where  $\Delta\theta_L$  and  $\omega_L$  are the angular range and spinning rate of the LIDAR, respectively.

As previously mentioned, particular trunk configurations are achieved as a aggregation of leg configurations. The inverse kinematic solution for each leg is solved, incorporating a desired trunk position and orientation, yielding a controlled trunk pose, as defined in Section 4.1.2. Moreover, the sweeping (pitching) range which BlueFoot can achieve during a scanning sequence is limited by the kinematic-feasibility of each  $k^{th}$  trunk pose that must be attained. For example, BlueFoot can pitch which cover a range of  $\pm 30$  degrees when configured in its default stance (see Table 12).

A single scan is taken at each  $k^{th}$  pose of the sweeping trajectory. The newly acquired scan is transformed from the LIDAR sensor frame,  $O_L$ , to the world frame,  $O_0$ , by a homogeneous transformation  $H_0^L$  which is defined as follows

$$H_0^L = H_b^L H_0^b \quad (6.9)$$

where  $H_0^b$  is a transformation from  $O_0$  to the trunk frame  $O_b$ , as defined in Chapter IV; and  $H_b^L$  defines a transformation from the frame  $O_b$  to the LIDAR frame,  $O_L$ .  $H_b^L$  is necessary for knowing the position of the LIDAR head with respect world frame, as the sensor itself has some offset and rotation relative to the robot's body. Each 2D point from  $x_i \in S$  from a raw LIDAR scan,  $S \subset \mathcal{R}^2$ , is transformed into a 3D scan segment,  $\bar{S}_k \subset \mathcal{R}^3$ , with respect to the frame  $O_0$  by:

$$\begin{bmatrix} \bar{x}_{i,k} \\ 1 \end{bmatrix} = H_b^L H_0^b \begin{bmatrix} x_i \\ 0 \\ 1 \end{bmatrix} \forall x_i \in S \quad (6.10)$$

where  $\bar{x}_{i,k} \in \bar{S}_k$  is a point within the  $k^{th}$  3D scan segment  $\bar{S}_k$ . After the sweeping routine is complete, 3D scan segments are composed into a final point cloud,  $\bar{S}$  by:

$$\bar{S} = \bigcup_{k=1}^{N_s} \bar{S}_k \quad (6.11)$$

where  $N_s$  defines the number of scans taken during the sweeping routine. For the sake of simplicity, it is assumed that the trunk's position,  $p_b$ , is fixed and the body is completely ridged during a 3D scanning routine (*i.e.*,  $\dot{p}_b = 0$ ). In the results to be presented, it will be shown that this is a reasonable assumption, as the robot is not walking and the trunk is pitched sufficiently slowly over the angular sweeping range. A slow sweep rate ensures that perturbations caused by vibrations during trunk rotation are small, and thus do not cause for significant deviations in LIDAR scan points. These vibrations result mainly from foot slippage and actuator noise.

### 6.2.2 Height-map Generation from a 3D point cloud

3D point clouds can be converted into height-maps to represent surfaces. Here a height-map will be represented via an associated discrete space  $\mathbb{Z}^M \subset \mathbb{Z}^2$  with a coordinate system  $O_M$ . Height-map representations are convenient for use in planning as they can be used to assign costs to path transitions in a straightforward way. Height-map information is represented as a matrix  $\mathcal{M} \in \mathcal{R}^{n \times m}$  with height elements  $m_{i,j}$ . A set

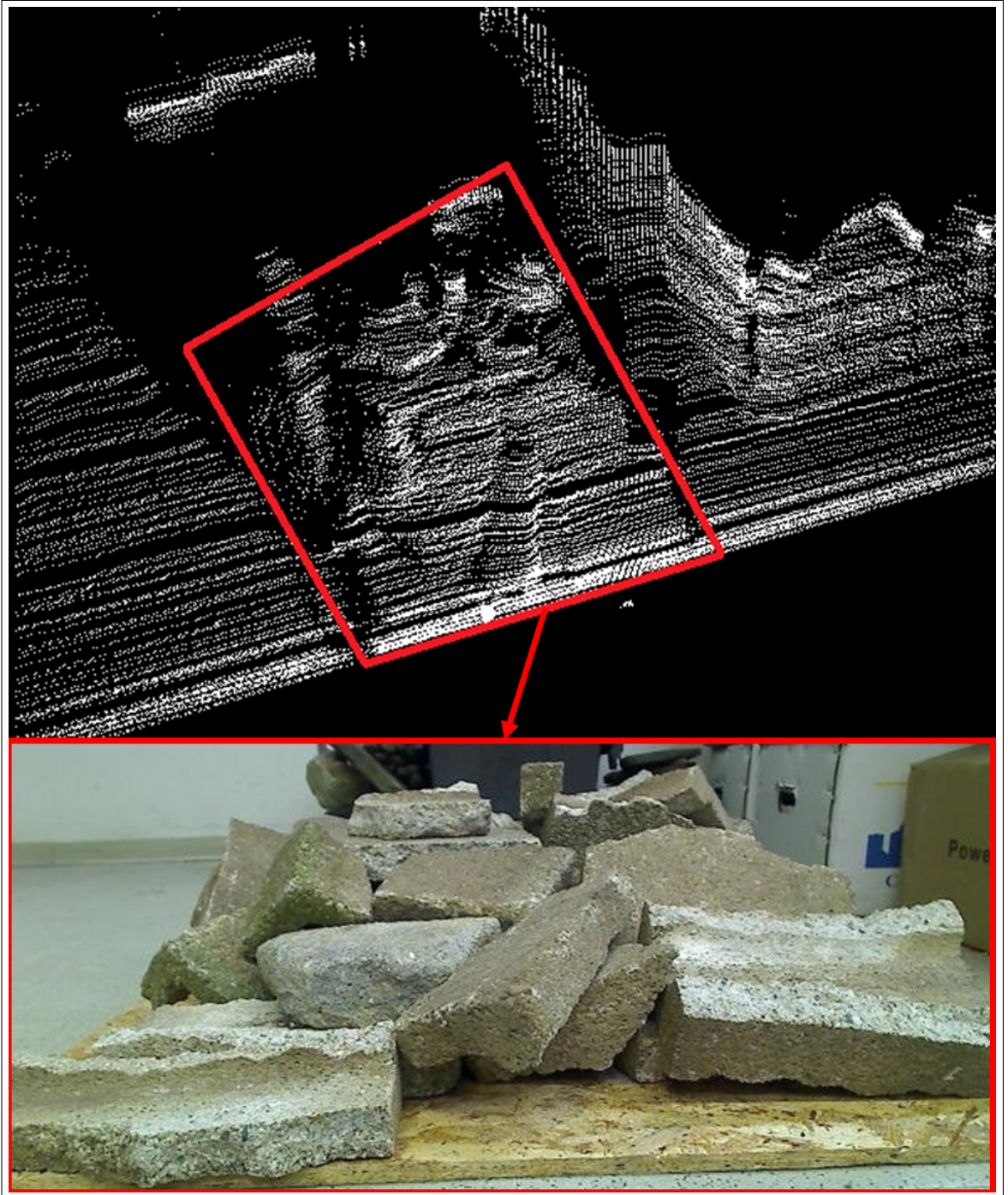


Figure 38: Original 3D point-cloud of terrain patch (*top*) and corresponding view from robot's on-board camera (*bottom*).

of indices  $\bar{p} = \{i, j\} \in \mathbb{Z}^{\mathcal{M}}$  is used to refer to the element  $m_{i,j}$  in  $\mathcal{M}$  and, simultaneously, a planar location with respect to the  $O_{\mathcal{M}}$  frame. Thus, the notations  $m_{i,j}$  and  $\mathcal{M}(\bar{p})$  will be used interchangeably to represent a height stored in the height-map matrix  $\mathcal{M}$ .

To create the height-map, a  $w \times d$  region of interest (ROI) with a relative location  $\bar{p}_0^{ROI}$  in  $O_0$  is first selected. This region is then discretized in  $(nm)$  subregions. The dimensions  $w$  and  $d$  of the ROI represent lengths along  $x$ -axis and  $y$ -axis respectively. The notation  $\mathbb{R}^{\mathcal{M}} \subset \mathcal{R}^3$  will be used to represent the set of points contained within the ROI. Moreover, the space  $\mathbb{Z}^{\mathcal{M}}$  is used to represent a discretized analogue to  $\mathbb{R}^{\mathcal{M}}$ , where each position  $\{i, j\} \in \mathbb{Z}^{\mathcal{M}}$  represents the  $i^{th}, j^{th}$  subregion of the ROI. Moreover, each subregion has an associated height of  $m_{i,j}$  stored in  $\mathcal{M}$ . An ROI selected from a source point cloud  $\bar{S}$  will be represented as  $\bar{S}_{ROI} \subset \mathcal{R}^3$ . It is assumed that the location,  $\bar{p}_0^{ROI}$ , and size of this ROI are determined via some auxiliary detection algorithm. Such a detection algorithm:

1. selects an area with high terrain variation (large changes in gradient),
2. determines  $\bar{p}_0^{ROI}$ ,
3. and determines the bounding region of the ROI.

For the results shown in this section, an exemplary ROI has been manually selected from an existing 3D point cloud. An algorithm which fulfills the above mentioned detection requirements has yet to be fully explored under the scope of this project.

The point  $\bar{p} \in \mathbb{Z}^{\mathcal{M}}$  is used to represent the location of a discrete subregion that is  $(w/m) \times (d/n)$  area. A corresponding height for that subregion is stored in  $m_{i,j}$ , and is selected as the largest  $z$ -component of any point that falls within said subregion. The transformation from a point cloud element,  $\bar{x}$ , to an element within the discretized height-map frame can be described by:

$$\begin{bmatrix} \bar{p} \\ m_{i,j} \end{bmatrix} = \begin{bmatrix} i \\ j \\ \frac{m}{m_{i,j}} \end{bmatrix} = \left[ \begin{bmatrix} n/d & 0 & 0 \\ 0 & m/w & 0 \\ 0 & 0 & 1 \end{bmatrix} \left( \begin{bmatrix} 0 & -1 & 0 \\ 1 & 0 & 0 \\ 0 & 0 & 1 \end{bmatrix} (\bar{x} - \bar{p}_0^{ROI}) + \begin{bmatrix} d \\ 0 \\ 0 \end{bmatrix} \right) \right] \quad (6.12)$$

where  $\lceil \cdot \rceil$  is an element-wise ceiling function which takes a vector argument  $(\cdot)$ .

Depending on the density of the source point cloud, the basic height-map conversion process has the potential to produce relatively sparse height-maps. To deal with this, a dilation and smoothing routine is used to fill in gaps in  $\mathcal{M}$ . During dilation, each non-zero height element within the map is expanded into a region around an existing element [66]. Dilation parameters are tuned so that uniform surface representation with

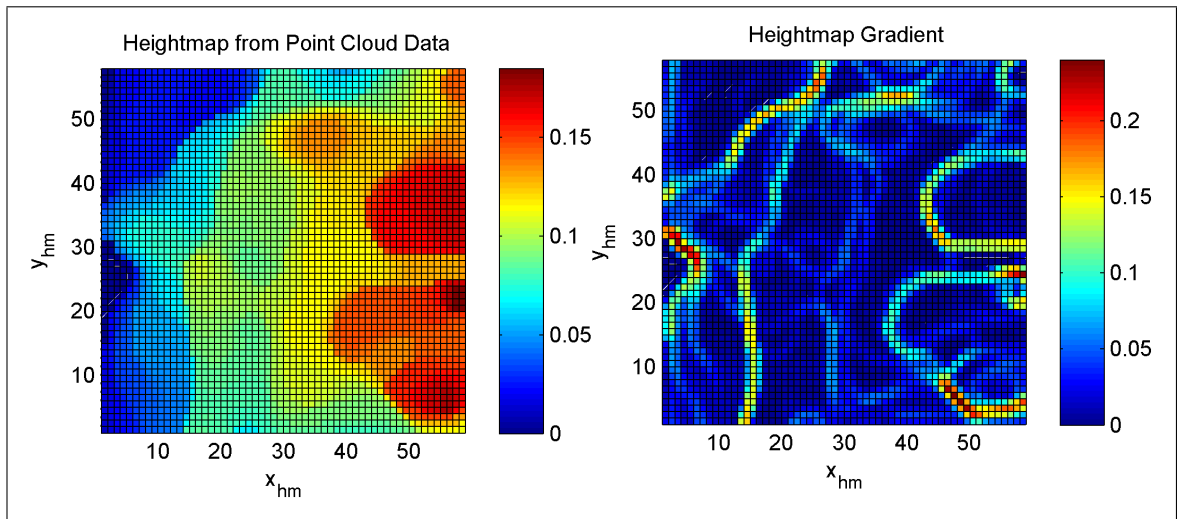


Figure 39: A height-map (*left*) and its corresponding gradient (*right*).

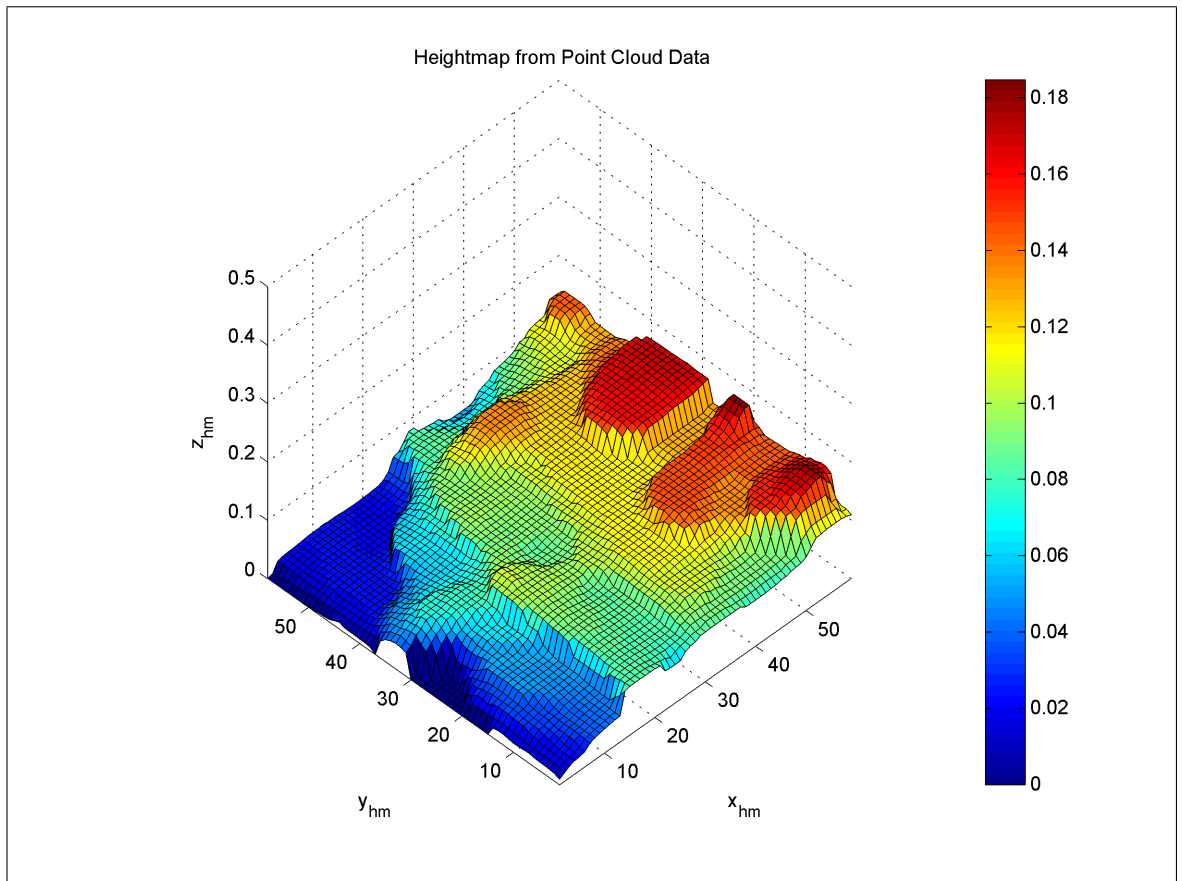


Figure 40: Height-map showing terrain variation.

minimal gaps between non-zero height elements is achieved. Finally, a median filter is applied to the dilated height-map to smooth transitions between elements.

The full height-map conversion process (from a 3D point cloud) is summarized in Algorithm 3. In this algorithm, *isolateROI* represents a function which locates a region of interest within the point cloud  $\bar{S}$ ; *subdivIndex* performs the transformation in (6.12), which generates indices  $(i, j) \in \mathbb{Z}^{\mathcal{M}}$  corresponding to a point in  $O_0$ ; *dilateFeatures* performs a calibrated image-dilation routine; and *medianFilter* performs a standard image median filter routine with a  $w \times w$  window size. Once a height-map has been generated, a corresponding gradient, as shown in Figure 39, is generated using a Sobel image gradient operation (from OpenCV). The image gradient operation is represented by the function *imageGradientSobel*.

---

**Algorithm 3** 3D ROI point cloud to height-map conversion.

---

```

init  $\mathcal{M} = 0, \nabla\mathcal{M}, m, n, w, d, \bar{S}, \bar{p}_0^{ROI}$ 
 $\{\bar{S}_{ROI}, \bar{p}_0^{ROI}\} = \text{isolateROI}(\bar{S})$ 
for all  $\bar{x}_k \in \bar{S}_{ROI}$  do
     $[i, j] = \text{subdivIndex}([\bar{x}_k]_x, [\bar{x}_k]_y, \bar{p}_0^{ROI}, w, d, m, n)$ 
    if  $[\bar{x}_k]_z > m_{i,j}$  then
         $m_{i,j} \leftarrow [\bar{x}_k]_z$ 
    end if
end for
 $\mathcal{M} \leftarrow \text{dilateFeatures}(\mathcal{M})$ 
 $\mathcal{M} \leftarrow \text{medianFilter}(\mathcal{M}, w)$ 
 $\nabla\mathcal{M} = \text{imageGradientSobel}(\mathcal{M})$ 

```

---

### 6.2.3 An approach for cost assignment from a height-map

A discrete height-map space can be converted to a cost representation for the purpose of foot-placement planning over rough terrain. Here, a cost-tensor,  $\mathcal{C} \in \mathcal{R}^{n \times m \times l}$ , is used to represent a discrete cost space. Each element  $c_{i,j,u}$  in  $\mathcal{C}$  represents a transition cost for a particular location  $(i, j, u)$ . The first and second dimensions of  $\mathcal{C}$  (of size  $n$  and  $m$ ) directly correspond to the width and depth of the discretized height-map space  $\mathbb{Z}^{\mathcal{M}}$ . The third dimension represents a discretization of the robot's yaw state,  $\theta_{b,z} \in [-\pi, \pi]$  into  $l$  subdivisions. In the sections to follow, the notation  $\mathcal{C}(\bar{p}^{\mathcal{M}}, u)$  and  $\mathcal{C}(i, j, u)$  will be used interchangeably to refer to a cost-element,  $c_{i,j,u}$ , from the transition-cost tensor  $\mathcal{C}$ .

The mapping between a height-map,  $\mathcal{M}$ , and cost-tensor,  $\mathcal{C}$ , is represented as follows:

$$\{\mathcal{C} = f(\mathcal{M}, \Gamma) : \mathcal{R}^{n \times m} \rightarrow \mathcal{R}^{n \times m \times l}\} \quad (6.13)$$

where  $\Gamma$  is a static configuration matrix used to describe the nominal spacing between the robot's feet.  $\Gamma$  is composed as follows:

$$\Gamma \equiv \{\bar{p}_{1,e}^{\mathcal{M}}, \bar{p}_{2,e}^{\mathcal{M}}, \bar{p}_{3,e}^{\mathcal{M}}, \bar{p}_{4,e}^{\mathcal{M}}\}$$

where  $\bar{p}_{v,e}^{\mathcal{M}} = [i_v, j_v]^T \in \mathbb{Z}^{\mathcal{M}}$  represents the position of each  $v^{th}$  foot in the height-map space with  $i_v \in \{1, \dots, m\}$  and  $j_v \in \{1, \dots, n\}$ . By formulating cost with respect to static foot configurations, planning is simplified to finding a trajectory for body position. Target foot positions are then generated relative to planned body locations during trajectory execution using  $\Gamma$  and (6.14), to follow. The mapping,  $f(\mathcal{M}, \Gamma)$ , has been formulated with respect to three main cost elements:

1. variation in height between all current footholds
2. terrain steepness around any foothold
3. and net robot rotation at each path-step.

The first cost element is chosen to penalize configurations in which the robot must stand on non-level terrain. This aids in ensuring that the kinematic workspace of each leg is not compromised by reducing the amount of “stretching” the robot has to perform in order to attain a particular configuration atop the terrain. The second cost element is used deter the robot from attempting to plan footholds atop overly steep terrain. The final cost element is used to ensure the robot does not plan to perform any large changes in direction while traversing the terrain, which could cause for needless motion (perhaps even loops) in the planned path.

To perform the conversion between  $\mathcal{M}$  and  $\mathcal{C}$ , a *moving* foothold matrix  $\Gamma'(\bar{p}_b^{\mathcal{M}}, u) \in \mathbb{Z}^{2 \times 4}$  is first defined as follows:

$$\Gamma'(\bar{p}_b^{\mathcal{M}}, u) = [R_z^{\mathcal{M}}(\gamma(u))\Gamma] + \bar{p}_b^{\mathcal{M}}B \quad (6.14)$$

where  $\bar{p}_b^{\mathcal{M}} = [i, j]^T \in \mathbb{Z}^{\mathcal{M}}$  and  $u \in \{1, \dots, l\}$  are discrete representations of the robot's trunk position and yaw within the cost-space, respectively;  $R_z^{\mathcal{M}}(\gamma(u)) \in \mathcal{R}^{2 \times 2}$  represents

a rotation in the  $\mathbb{Z}^{\mathcal{M}}$  plane; and  $B = [1, 1, 1, 1]$ .  $\{\gamma(u) : \mathbb{Z} \rightarrow \mathcal{R}\}$  represents a linear mapping from the index  $u$  to a robot yaw in  $O_{\mathcal{M}}$ , which is defined explicitly as follows:

$$\gamma(u) = 2\pi \left( \frac{u}{l} \right) - \pi \in [-\pi, \pi] \quad (6.15)$$

The cost-tensor is then generated as follows:

$$\begin{aligned} \Gamma' &\equiv \Gamma'(\bar{p}_b^{\mathcal{M}}, u) \\ \mathcal{H}_v &= \mathcal{M}(\text{col}(\Gamma')_v) \\ \delta\mathcal{H}_v &= \nabla\mathcal{M}(\text{col}(\Gamma')_v) \\ \mathcal{C}(\bar{p}_b^{\mathcal{M}}, u) &= k_{\text{var}} \text{var}(\mathcal{H}) + k_{\delta} \sum_{v=1}^4 \delta\mathcal{H}_v^2 + k_{\theta} \gamma^2(u) \end{aligned} \quad (6.16)$$

$\forall \bar{p}_b^{\mathcal{M}} \in \mathbb{Z}^{\mathcal{M}}$ ,  $\forall u \in \{1, \dots, l\}$ , and  $v \in \{1, 2, 3, 4\}$ , where  $\mathcal{H}$  is a set of heights at each moving-foothold position in  $\mathcal{M}$ ;  $\delta\mathcal{H}$  is a set of corresponding elements from the gradient matrix  $\nabla\mathcal{M}$ ;  $\text{var}(*)$  computes the variance between the elements of a vector argument (\*);  $k_{\text{var}}$ ,  $k_{\delta}$  and  $k_{\theta}$  are scalar weighting parameters; and  $\text{col}(*)_v$  extracts the  $v^{\text{th}}$  column from the matrix argument (\*). Figure 41 shows two projections of the sample cost-tensor for fixed robot orientations of  $\theta_z = 0$  and  $\theta_z = \pi/4$ . The configuration matrix,  $\Gamma$ , is setup such that feet of the robot are spaced 330 mm apart, with respect to  $O_0$ . This corresponds to the nominal foot spacing of BlueFoot's default stance. The cost-tensor shown in Figure 41 was generated using the height-map and corresponding gradient shown in Figure 39.

$\mathcal{C}$  is used to generate an optimal,  $N$ -step path, which is comprised of  $N$  discrete robot configurations. Moreover, the problem of planning a path over rough terrain is setup as a minimization of an  $N$ -step cost functional defined as follows:

$$J(N) = \sum_{k=0}^N \mathcal{C}(\bar{p}_{b,k}^{\mathcal{M}}, u_k) \quad (6.17)$$

Here,  $\mathcal{C}(\bar{p}_{b,k}^{\mathcal{M}}, u_k)$  plays the role of a tabular objective function. An optimal path can be found from  $\mathcal{C}$  using an  $A^*$ -based path planning algorithm, for example [67]. This method has yet to be fully explored in the scope of this project, but is widely accepted as a standard technique for optimal path planning in discrete spaces. Here, a sub-optimal approach is taken, which will be presented next. Paths generated using the cost-tensor  $\mathcal{C}$  can be mapped back into  $O_0$  using the corresponding inverse mappings of (6.12) and  $\gamma(u)$ , and interpolated to generate smooth trajectories.

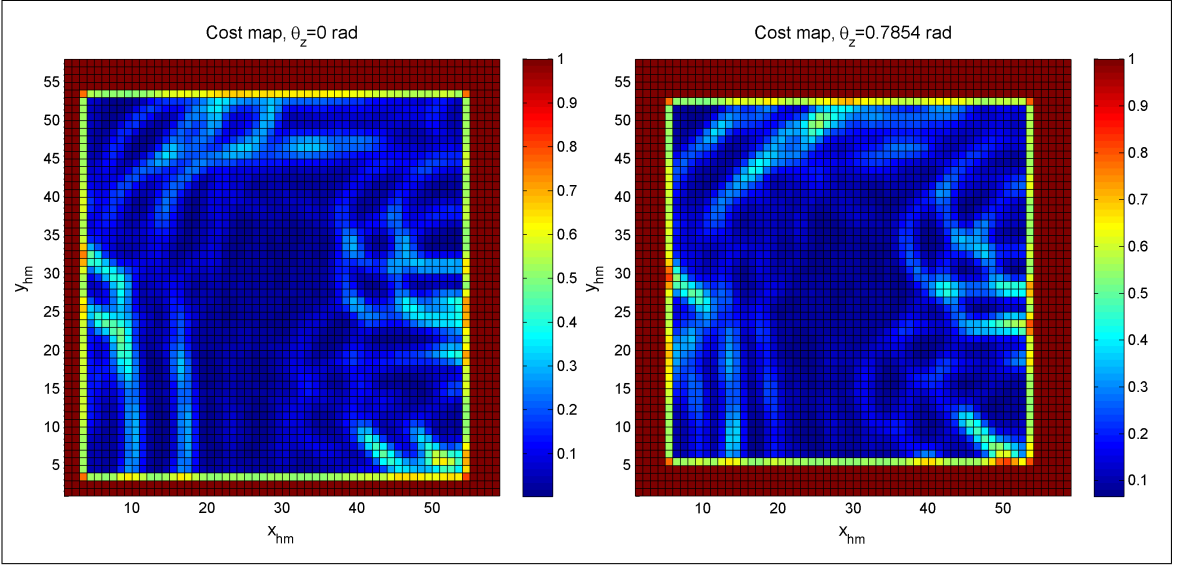


Figure 41: Projections of a sample cost-tensor generated from the height-map shown in Figure 39.

#### 6.2.4 A sliding-window approach for sub-optimal rough terrain planning

A sub-optimal planning algorithm is formulated as a preliminary method for terrain planning using the cost-tensor  $\mathcal{C}$ . In this algorithm, navigation way-points are generated through a series of successive optimizations upon finite windows of  $\mathcal{C}$ . Each optimization step is used to plan a body position  $\bar{p}_{b,k}^{\mathcal{M}}$  way-point and an orientation  $u_k$ , starting from an arbitrary initial position,  $\bar{p}_{b,0}^{\mathcal{M}}$  and orientation  $u_0$ . Each optimization step takes the form:

$$\begin{aligned} & \min_{\psi_k, \lambda_k} \mathcal{C}(\psi_k, \lambda_k) \\ \text{s.t. } & \psi_k \in \mathbb{Z}_k^w \\ & \lambda_k \in \mathbb{Z}_k^u \end{aligned} \tag{6.18}$$

where  $\psi_k = \{i_{\psi,k}, j_{\psi,k}\}$ ; and  $\mathbb{Z}_k^w \subset \mathbb{Z}^{\mathcal{M}}$  and  $\mathbb{Z}_k^u \subset \{1, \dots, l\}$  are moving, asymmetric windows about each  $(k-1)^{th}$  way-point position and orientation, respectively, defined as follows:

$$\begin{aligned} & \mathbb{Z}_k^w \text{ s.t.} \\ & i_{\psi,k} \in \{(i_{b,k-1} - d_w), (i_{b,k-1} - d_w + 1), \dots, (i_{b,k-1} + d_w)\} \\ & j_{\psi,k} \in \{(j_{b,k-1} + 1), \dots, (j_{b,k-1} + d_w)\} \\ & \mathbb{Z}_k^u \equiv \{(u_{k-1} - d_u), (u_{k-1} - d_u + 1), \dots, (u_{k-1} + d_u)\} \end{aligned} \tag{6.19}$$

|                  | <b>T1</b> | <b>T2</b> | <b>T3</b> | <b>T4</b> |
|------------------|-----------|-----------|-----------|-----------|
| $d_w = d_u = 1$  | 24.9012   | 25.1534   | 28.9889   | 29.9231   |
| $d_w = d_u = 5$  | 20.2524   | 21.8537   | 23.8874   | 20.7319   |
| $d_w = d_u = 15$ | 16.8602   | 21.8307   | 19.4236   | 23.5314   |
| $d_w = d_u = 30$ | 19.3791   | 19.0536   | 23.6496   | 23.6142   |

Table 13: Sum of costs for four path-planning trials with varying initial positions varying optimization windows.

with  $\psi_k = (i_{\psi,k}, j_{\psi,k})$ ;  $p_{b,k-1}^{\mathcal{M}} = (i_{b,k-1}, j_{b,k-1}) \in \mathbb{Z}^{\mathcal{M}}$ , as previously defined; and  $d_w > 0$  and  $d_u > 0$  being integer window-size parameters. The asymmetry of these windows in the  $j_{\psi,k}$  coordinate direction ensures that the  $k^{th}$  way point is planned forward from the  $(k-1)^{th}$  way-point in the  $y$ -axis direction (*i.e.*, such that there is no back-tracking). The local optimizers  $\psi_k^*$  and  $\lambda_k^*$ , represent the coordinates at which the objective function in (6.18) is minimized. They are used to generate a  $k^{th}$  trajectory way-point by:

$$\begin{aligned} i_{b,k} &= i_{b,k-1} + \text{sign}(i_{\psi,k}^* - d_w/2 - 1) \\ j_{b,k} &= j_{b,k-1} + \text{sign}(j_{\psi,k}^* - 1) \\ u_k &= u_{k-1} + \text{sign}(\lambda_k^* - d_u/2 - 1) \end{aligned} \quad (6.20)$$

where  $\text{sign}(n)$  is an operator such that:

$$\text{sign}(n) \equiv \begin{cases} +1 & \text{if } n > 0 \\ -1 & \text{otherwise} \end{cases} \quad (6.21)$$

Figures 42 through 45 show simulated path-planning results over the terrain originally depicted in Figure 38. Simulations were configured such that a path is planned from a starting point near the  $y = 0$  in the real-world coordinate from, to the opposite side of the terrain patch moving in the  $y$ -axis direction. In each simulation group, the  $x$ -coordinate of the initial position  $p_{b,0}^0$  and initial orientation,  $u_0$ , are varied for each trial. A single window size for  $d_w$  and  $d_u$  is configured for each simulation group. The resulting planned paths are displayed with respect real-world coordinates, mapped from the  $O_{\mathcal{M}}$  frame. Each planned path is smoothed using a moving-average filter. Table 13 summarizes the total cost of each path taken for each trial, with respect to a selected window size.

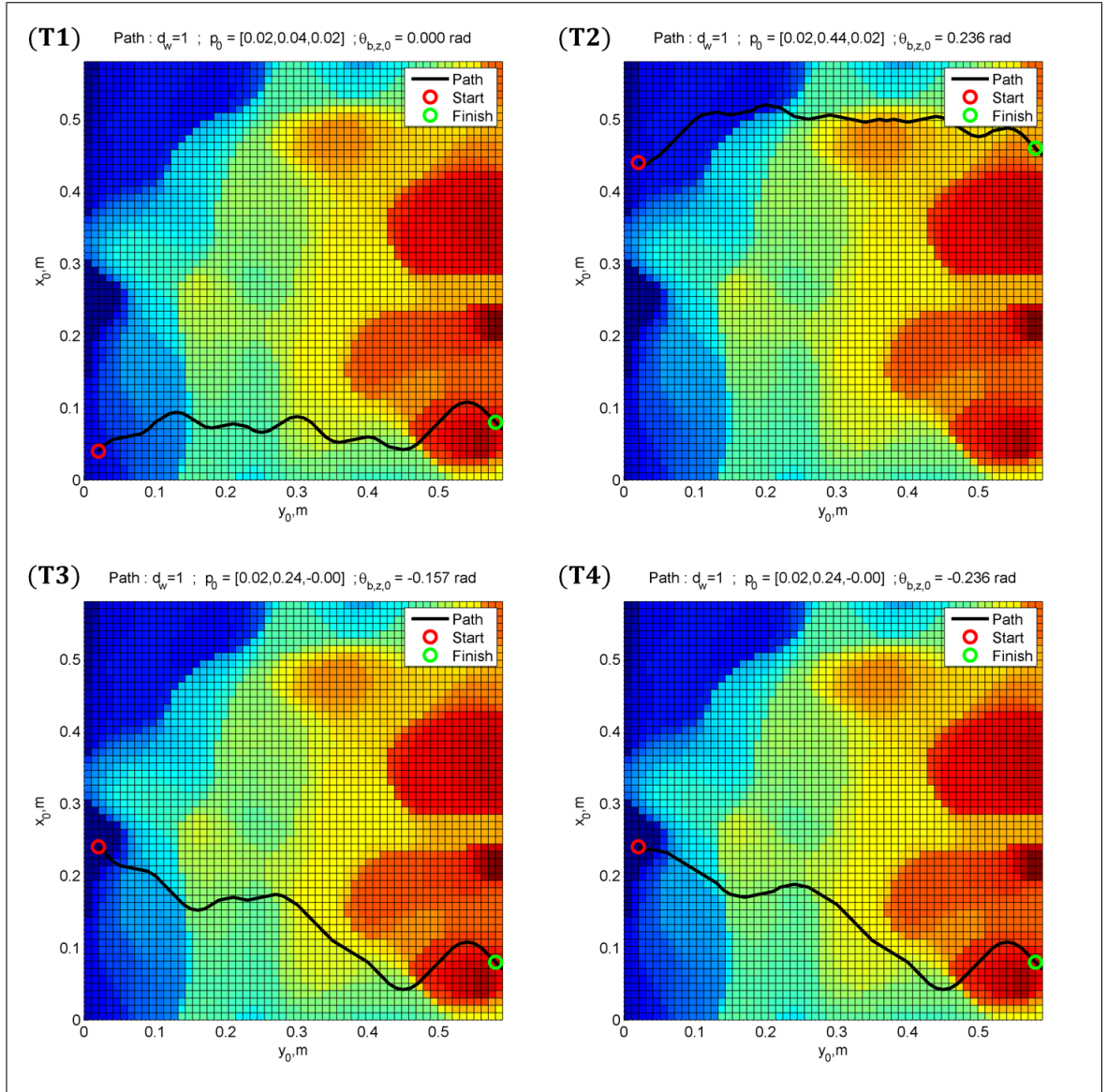


Figure 42: Path planned over rough terrain with  $d_w = d_u = 1$ .

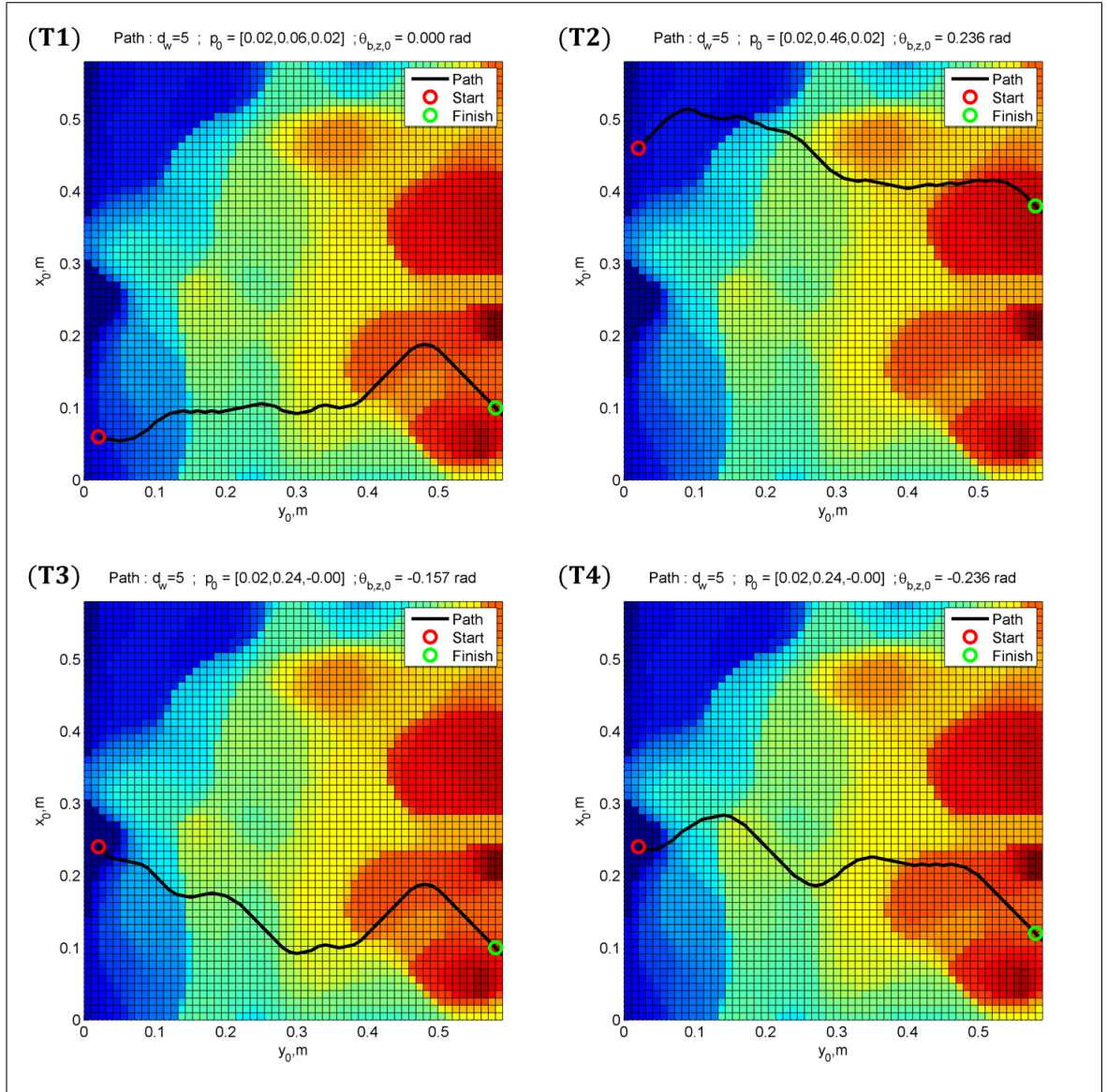


Figure 43: Path planned over rough terrain with  $d_w = d_u = 5$ .

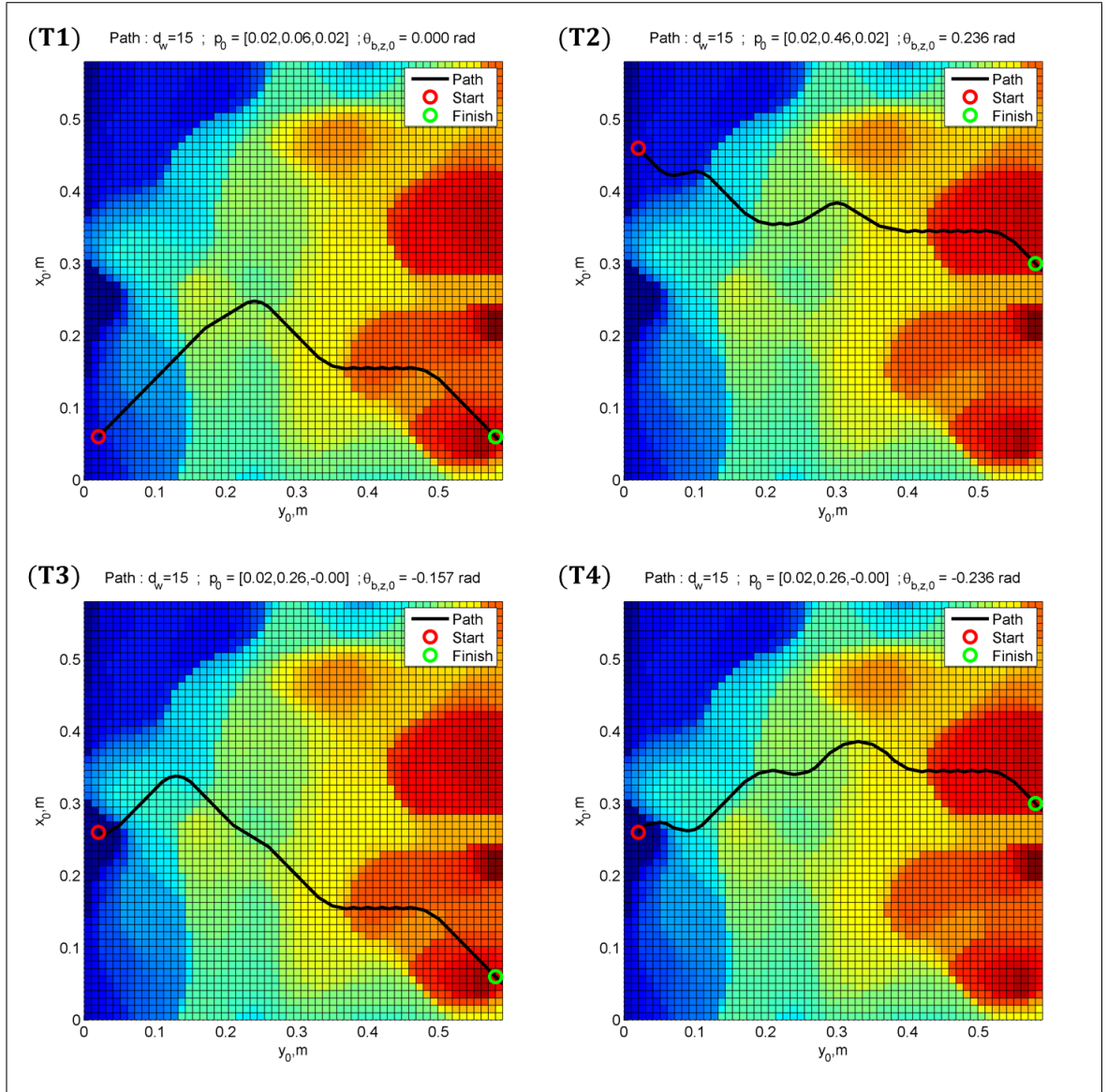


Figure 44: Path planned over rough terrain with  $d_w = d_u = 15$ .

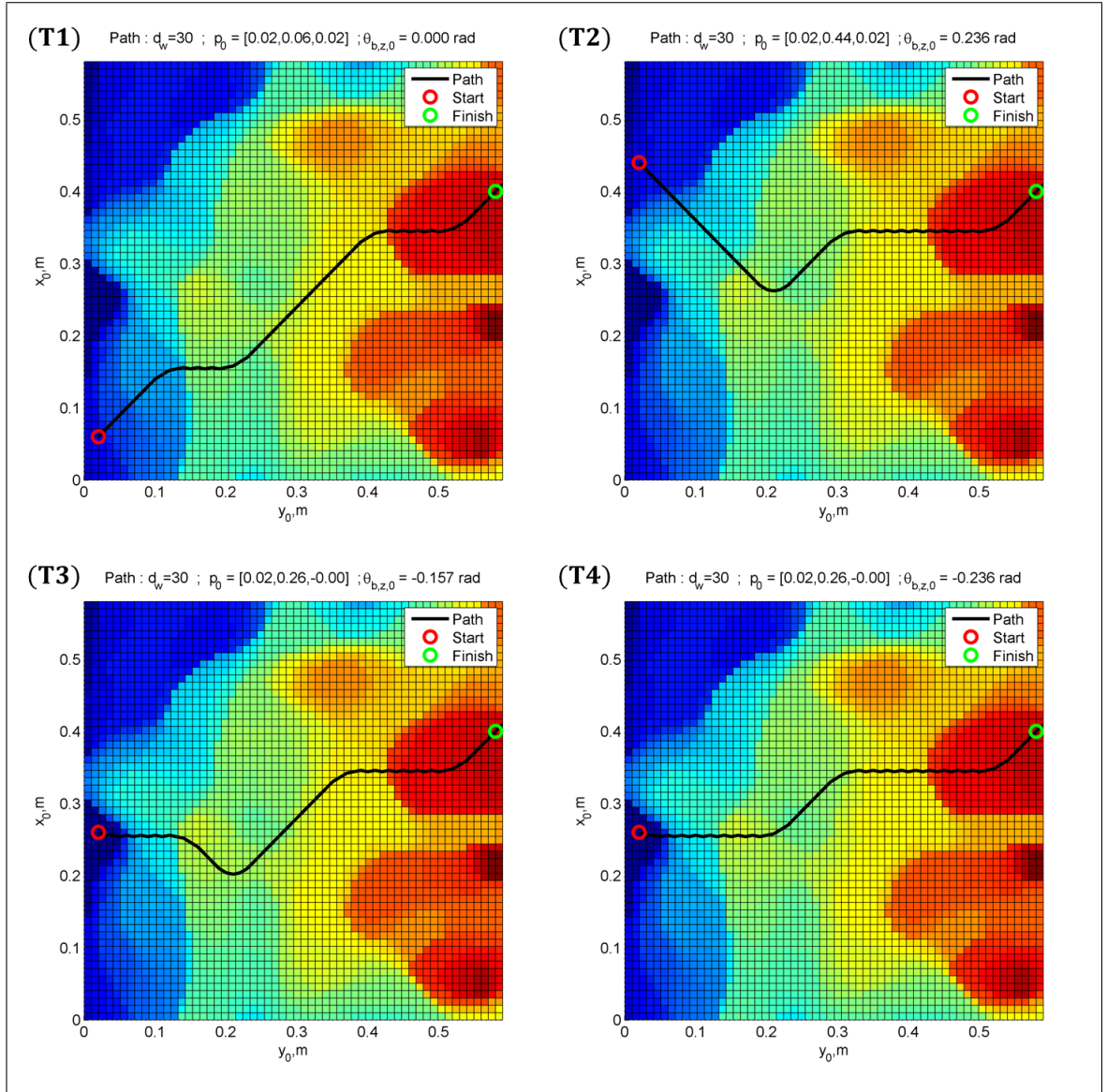


Figure 45: Path planned over rough terrain with  $d_w = d_u = 30$ .

### 6.2.5 Surface Reconstruction

3D surface reconstruction is carried out according to a process for normal-estimation detailed in [44]. According to this procedure, 3D surfaces are reconstructed from point cloud,  $\bar{S}$ , by fitting a collection of flat polygonal elements to successive point clusters which fall within a range  $d_s$  of each point in  $\bar{x}_i \in \bar{S}$ . Each of these estimated elements is represented by a surface-normal which emanates from each  $\bar{x}_i$  within the source cloud.

The raw 3D point cloud,  $\bar{S}$ , which is typically dense, is down-sampled and smoothed before a normal estimation algorithm is applied. Point cloud down-sampling is performed using a voxel-grid technique, which discretizes the point cloud space into a voxel-space. The voxel-space consists of stacked cuboids of a particular side-length. Each cubic unit of the voxel space is parameterized by a single voxel side-length dimension  $d_{vox}$ . The voxel-grid filter generates a single-point from all points which fall within a voxel region. A KD-tree search technique is used to find points which are contained by a particular voxel region. This technique offers higher efficiency over a brute-force search for neighboring points. This voxel-grid down-sampling technique produces a reduced representation of the original cloud,  $\hat{S}$ . Empirical results have shown that  $\hat{S}$  can contain up to ten to twenty times less points than the original cloud,  $\bar{S}$ . This reduced-point cloud representation greatly reduces the computational effort needed to process the point cloud  $\hat{S}$ .

---

**Algorithm 4** Finding good places to step from a 3D point cloud.

---

```

init  $\hat{S}, \bar{S}, \bar{S}^*, d_{vox}, \vec{u}^r, e, e_{max}$ 
 $\hat{S} = \text{voxelGridFilter}(\bar{S}, d_{vox})$ 
 $\hat{S} \leftarrow \text{movingLeastSquaresFilter}(\hat{S})$ 
 $\hat{N} = \text{estimateNormals}(\hat{S})$ 
for all  $\vec{n}_i \in N$  do
     $e = 1 - (\vec{u}^r)^T \vec{n}_i$ 
    if  $e < e_{max}$  then
         $\bar{S}^* \leftarrow \bar{S}^* \cup \bar{x}_i$ 
    end if
end for

```

---

Next, the resulting cloud,  $\hat{S}$ , is regularized using a moving least-squares filter. This filter creates a smoothed point cloud by performing a sequence polynomial fits over

a moving subset of points. Once regularized, normals are estimated from the point cloud via a plane fitting method, as described in [68]. Planes are estimated using Principle Component Analysis (PCA) on clusters of points [69]. The standard PCA algorithm provides a least-squares plane fit by way of dimensional reduction, yielding best-fit description for a set 3D points as a 2D manifold [46]. The full surface-normal estimation algorithm is provided in Algorithm 1. A point cloud with estimated surface normals is shown in Figures 46 and 47.

Algorithm 4 is used convert a 3D point cloud into an augmented point-cloud with normal vectors. This augmented cloud is then used to find “flat” regions within the reconstructed surface. This is performed for the purpose of footstep planning. Flat regions are located using the computed surface normals. The alignment of each  $i^{th}$  normal,  $\vec{n}_i$ , is compared to a reference unit vector,  $\vec{u}^r$ , by taking a dot product. This dot-product operation produces an alignment error  $e \in [0, 2]$ . Points with associated normals whose alignment error is less than a scalar error bound,  $e_{max}$ , are selected as surfaces fit for walking (*i.e.*, flat). Obviously, not all surfaces which satisfy this alignment criteria represent surfaces which are fit for traversal. Beyond normal estimation, several additional post processing operations are necessary. Namely, the resulting point cloud must be segmented into regions which are traversable by the robot.

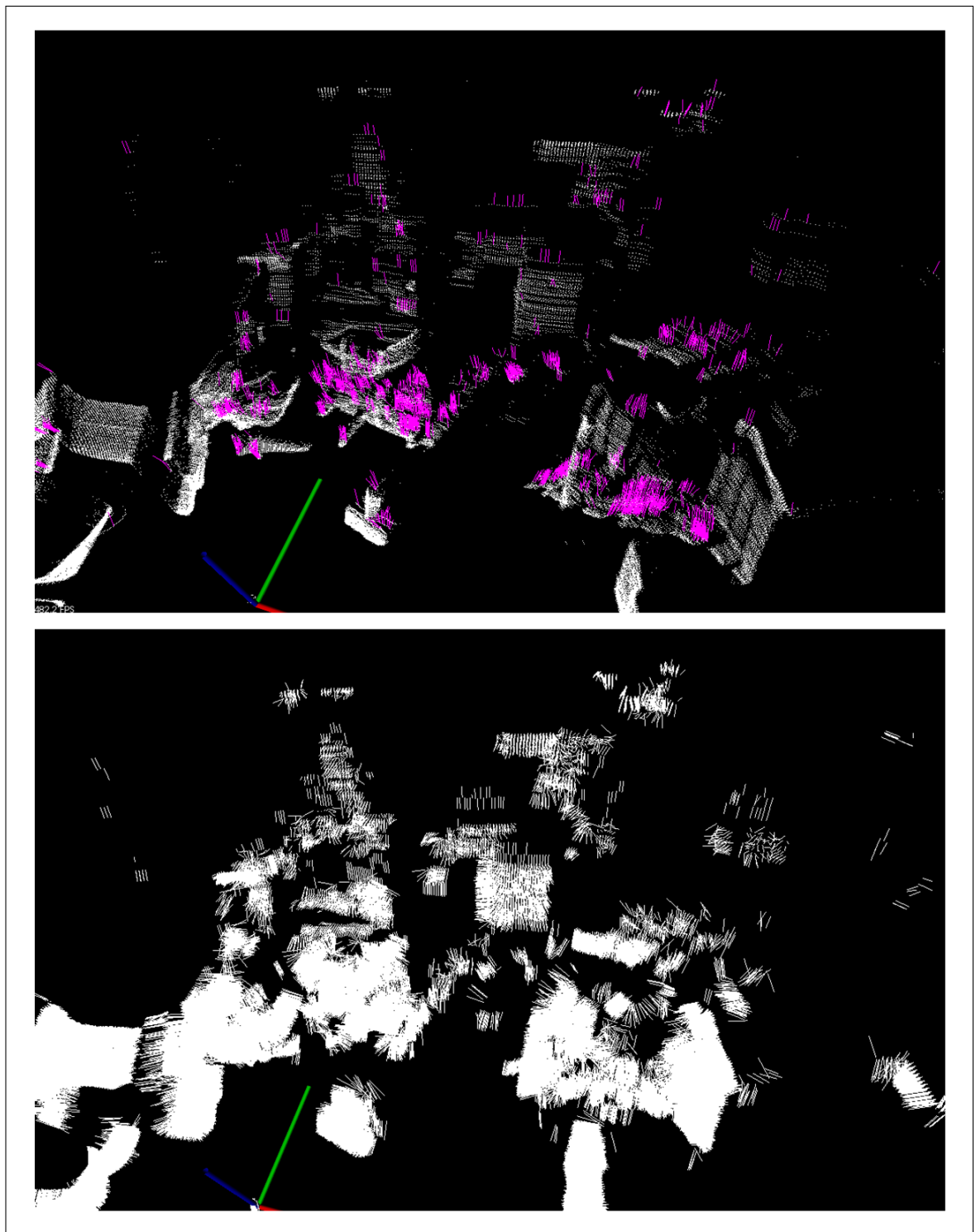


Figure 46: Point cloud generated from sequential scans of a room showing flat-surface candidates (*top*) and 3D point cloud with estimated normals (*bottom*).

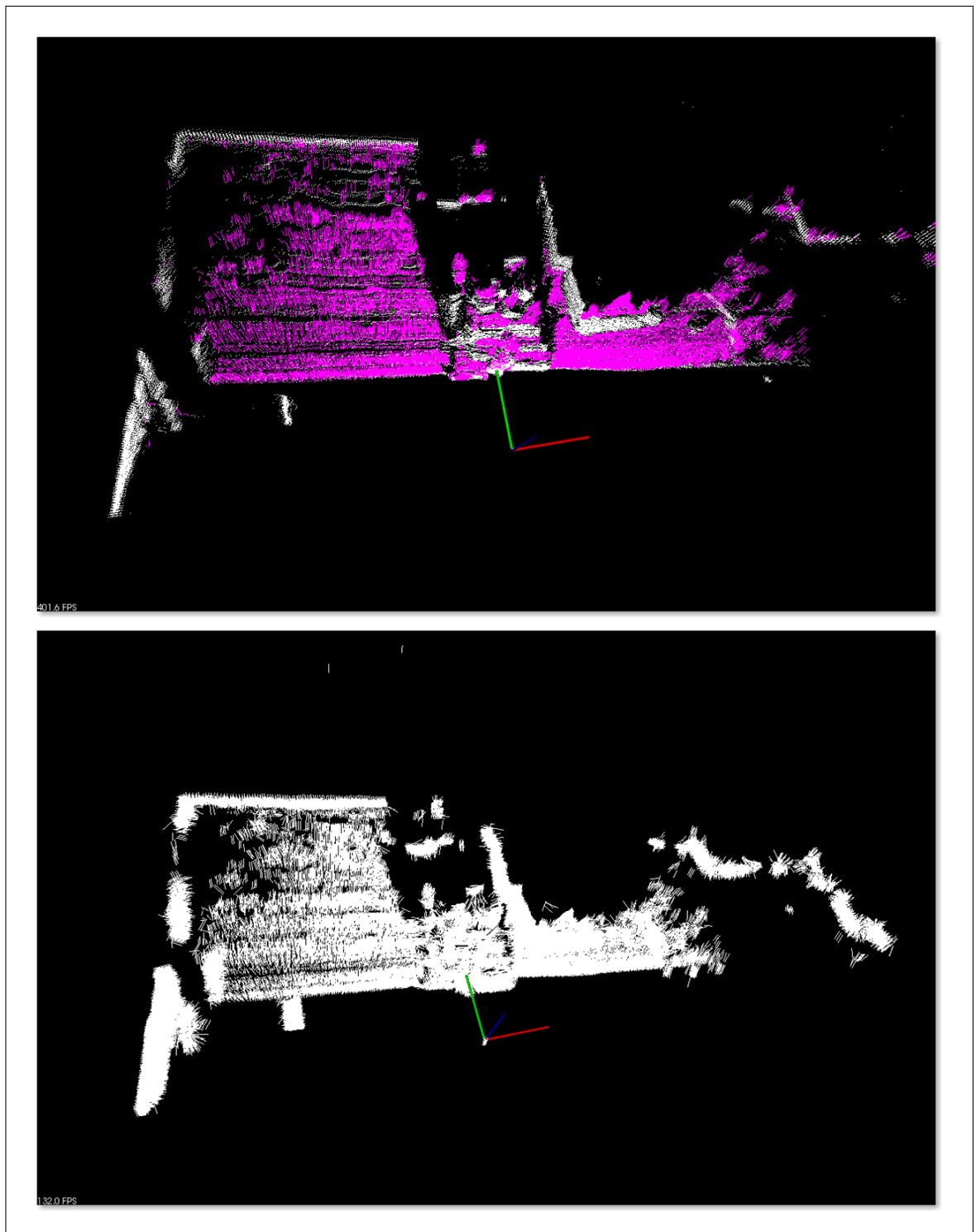


Figure 47: Point cloud generated from sequential scans of a floor with obstacles showing flat-surface candidates (*top*) and 3D point cloud with estimated normals (*bottom*).

## CHAPTER VII

### Concluding Remarks

This thesis has provided a comprehensive summary of the design and control of the BlueFoot quadruped platform. Namely, BlueFoot's structural makeup; component devices; software architecture; gait and stability control; and related navigation control mechanisms have been described in detail. Results from simulated and actual trials have been provided to demonstrate the performance of routines used to control the BlueFoot platform. This final section will provide some insight about future directions for the BlueFoot project, including future directions with work regarding the design of the BlueFoot platform; and with work regarding its control and navigation.

Future work regarding the design of the existing BlueFoot platform will focus on redesigning the structure of BlueFoot's legs. The platform currently requires servos which generate higher torque outputs, particularly at its upper joints. The torque output of BlueFoot's current joint servos have shown to be adequate for moderate locomotion tasks, but may not be powerful enough for more demanding tasks over extended periods of operation. Currently, servos which actuate the upper joints tend to overheat during operation, causing them to shut down. Joint shut down is a safety feature which is part of the servo control software. This indicates that these servos are constantly operating near the output limits, even during moderately demanding tasks. To the same end, it would also be beneficial to re-incorporate series elastic joints into the robot's design for the purpose of generating more fluid gait motions and relieving dynamic torque loading during impact. The incorporation of series elastic joints would also allow for faster gaits and extended this project toward possible future studies regarding under-actuated quadruped gait control.

Future work involving the control of the BlueFoot platform will mainly focus on research into algorithms for optimal motion planning and traversal over irregular terrain, as well as optimal whole-body motion planning towards sensor articulation and dynamic gait stability applications. In regards to rough-terrain planning, supporting algorithms

must also be developed for the classification of rough terrain regions. Such routines will be necessary for deducing whether or not an area of terrain is of high irregularity; as well as whether or not the terrain is traversable or needs to be traversed in order to reach a goal location. The associated area will be mapped and represented using the surface reconstruction mechanisms detailed in this thesis. Finally, an adaptive footstep and body-placement planner will be used to navigate the robot over rough terrain.

The ultimate goal of this research is to design a set of control-laws for the BlueFoot platform such that the robot can simultaneously map the surrounding terrain and update its foot placement planning in real time. There are many situations wherein incremental terrain mapping and re-planning is necessary, especially in situations where information about upcoming terrain is incomplete. Specifically, one such situation arises when the terrain is dynamic, such as when the terrain can be modified when the robot makes contact with it. Another obvious situation arises when the robot can only partially perceive upcoming terrain from its current vantage point. This could occur if the terrain being mapped was taller than the effective viewing height of the vision sensor being utilized to generate the associated terrain map.

In the event of missing terrain data, current implementations utilize approximations for terrain beyond the portions which are immediately perceivable, such as those described in [70]. Along with improving these types of techniques, it is also important to develop a set of techniques which can be used to navigate the robot based on a continuously updated terrain map. In BlueFoot's case, this would mean that the robot must execute a coordinated set of motions which allow it to articulate its LIDAR sensor, for the purpose of effective terrain mapping, while also walking over said terrain. From this, a complicated whole-body motion planning problem arises. The solution to such a problem would need to address a method for generating optimal body-motion trajectories, which simultaneously achieve a stable robot configuration during gaiting, while also generating effective sweeping motions for terrain scanning with the body-mounted LIDAR. This problem also demands an accurate localization of the robot. For this, methods for simultaneous localization and mapping in 3D will have to be explored. Additionally, terrain features could be used to localize the robot based on its kinematic configuration. In such a localization scheme, robot orientation, foot contact, and joint position data could be used to estimate the robot's kinematic pose from sets of terrain features representing possible foot contact points.

Additional problems arise from the root rough-terrain planning problem, including

an assignment of cost to the act of actually mapping a region of terrain. In this regard, one must consider the time and effort (energy demands, computational effort, storage demands etc.) required for completing a terrain map of a particular region. In BlueFoot’s case, a significant amount of control effort is spent during terrain scanning. If we consider a routine similar to BlueFoot’s current terrain-scanning routine, in which the robot comes to a complete stop before sweeping its body to generate varying scan levels, then the cost of generating information about the upcoming terrain manifests in both the time and physical energy spent collecting terrain information. In a more elegant control scheme, where the robot simultaneously moves and maps its terrain, this cost manifests as extra energy exerted in the act of articulating the robot’s body. From these considerations arises a question about how a robot agent can somehow predict the cost of mapping an area of terrain, from a smaller set of terrain features, before exerting the full required effort for acquiring a more detailed representation of a particular region. The robot could also learn to predict which terrains have a higher potential for successful traversal.

## Appendix A

### Leg Jacobian with respect to frame $O_{i,0}$

$$\begin{aligned}
J_{i,e}^{i,0} &= \begin{bmatrix} j_{1,1}^{i,0} & \cdots & j_{1,4}^{i,0} \\ \vdots & \ddots & \vdots \\ j_{6,1}^{i,0} & \cdots & j_{6,4}^{i,0} \end{bmatrix} \\
j_{1,1}^{i,0} &= -s_{i,1}(2a_1 + 2a_3c_{i,23} + 2a_2c_{2,i} + a_4c_{i,234})/2 \\
j_{1,2}^{i,0} &= -c_{i,1}(a_3s_{i,23} + a_2s_{2,i} + a_4s_{i,234}/2) \\
j_{1,3}^{i,0} &= -c_{i,1}(a_3s_{i,23} + a_4s_{i,234}/2) \\
j_{1,4}^{i,0} &= -a_4s_{i,234}c_{i,1}/2 \\
j_{2,1}^{i,0} &= c_{i,1}(2a_1 + 2a_3c_{i,23} + 2a_2c_{2,i} + a_4c_{i,234})/2 \\
j_{2,2}^{i,0} &= -s_{i,1}(a_3s_{i,23} + a_2s_{2,i} + (a_4s_{i,234})/2) \\
j_{2,3}^{i,0} &= -s_{i,1}(a_3s_{i,23} + a_4s_{i,234}/2) \\
j_{2,4}^{i,0} &= -a_4s_{i,234}s_{i,1}/2 \\
j_{3,2}^{i,0} &= a_3c_{i,23} + a_2c_{2,i} + a_4c_{i,234}/2 \\
j_{3,3}^{i,0} &= a_3c_{i,23} + a_4c_{i,234}/2 \\
j_{3,4}^{i,0} &= a_4c_{i,234}/2 \\
j_{4,2}^{i,0} &= j_{4,3}^{i,0} = j_{4,4}^{i,0} = s_{i,1} \\
j_{5,2}^{i,0} &= j_{5,3}^{i,0} = j_{5,4}^{i,0} = -c_{i,1} \\
j_{6,1}^{i,0} &= 1 \\
j_{6,4}^{i,0} &= j_{6,3}^{i,0} = j_{6,2}^{i,0} = j_{4,1}^{i,0} = j_{5,1}^{i,0} = j_{3,1}^{i,0} = 0
\end{aligned}$$

See Appendix C for a summary of abbreviations.

## Appendix B

### Fixed-base Leg Dynamics

#### General Form

$$\tau = M(q_i)\ddot{q}_i + C(q_i, \dot{q}_i)\dot{q}_i + G(q_i, \vec{g})$$

**Mass Matrix,  $M(q_i)$**

$$\begin{aligned}
M_{11} &= m_{i,1} + m_{i,2} + m_{i,3} + m_{i,4} + (m_{i,4}s_{i,1}^2(2a_1 + 2a_3c_{i,23} + 2a_2c_{i,2} + a_4c_{i,234})^2)/4 \\
&\quad + (m_{i,3}c_1^2(2a_1 + a_3c_{i,23} + 2a_2c_{i,2})^2)/4 \\
&\quad + (m_{i,3}s_{i,1}^2(2a_1 + a_3c_{i,23} + 2a_2c_{i,2})^2)/4 \\
&\quad + (a_1^2m_{i,1}c_1^2)/4 + (a_1^2m_{i,1}s_{i,1}^2)/4 \\
&\quad + (m_{i,2}c_1^2(2a_1 + a_2c_{i,2})^2)/4 + (m_{i,2}s_{i,1}^2(2a_1 + a_2c_{i,2})^2)/4 \\
&\quad + (m_{i,4}c_1^2(2a_1 + 2a_3c_{i,23} + 2a_2c_{i,2} + a_4c_{i,234})^2)/4 \\
M_{22} &= m_{i,2} + m_{i,3} + m_{i,4} + (a_2^2m_{i,2})/4 + a_2^2m_{i,3} + a_2^2m_{i,4} \\
&\quad + (a_3^2m_{i,3})/4 + a_3^2m_{i,4} + (a_4^2m_{i,4})/4 + a_2a_4m_{i,4}c_{i,34} + a_2a_3m_{i,3}c_{i,3} \\
&\quad + 2a_2a_3m_{i,4}c_{i,3} + a_3a_4m_{i,4}c_{i,4} \\
M_{33} &= m_{i,3} + m_{i,4} + (a_3^2m_{i,3})/4 + a_3^2m_{i,4} + (a_4^2m_{i,4})/4 + a_3a_4m_{i,4}c_{i,4} \\
M_{44} &= (m_{i,4}(a_4^2 + 4))/4 \\
M_{12} &= M_{21} = 0 \\
M_{13} &= M_{31} = 0 \\
M_{14} &= M_{41} = 0 \\
M_{23} &= M_{32} = m_{i,3} + m_{i,4} + (a_3^2m_{i,3})/4 + a_3^2m_{i,4} + (a_4^2m_{i,4})/4 + (a_2a_4m_{i,4}c_{i,34})/2 \\
&\quad + (a_2a_3m_{i,3}c_{i,3})/2 + a_2a_3m_{i,4}c_{i,3} + a_3a_4m_{i,4}c_{i,4} \\
M_{24} &= M_{42} = (m_{i,4}(a_4^2 + 2a_2a_4c_{i,34} + 2a_3a_4c_{i,4} + 4))/4 \\
M_{34} &= M_{43} = (m_{i,4}(a_4^2 + 2a_3c_{i,4}a_4 + 4))/4
\end{aligned}$$

## Correolis Matrix, $C(q_i, \dot{q}_i)$

$$\begin{aligned}
C_{11} &= -\dot{q}_{i,3}((m_{i,4}c_1^2(2a_3s_{i,23} + a_4s_{i,234})(2a_1 + 2a_3c_{i,23} + 2a_2c_{i,2} + a_4c_{i,234}))/2 \\
&\quad + (m_{i,4}s_{i,1}^2(2a_3s_{i,23} + a_4s_{i,234})(2a_1 + 2a_3c_{i,23} + 2a_2c_{i,2} + a_4c_{i,234}))/2 \\
&\quad + (a_3m_{i,3}s_{i,23}c_1^2(2a_1 + a_3c_{i,23} + 2a_2c_{i,2}))/2 + (a_3m_{i,3}s_{i,23}s_{i,1}^2(2a_1 + a_3c_{i,23} + 2a_2c_{i,2}))/2) \\
&\quad - \dot{q}_{i,2}((a_2^2m_{i,2}s_{i,2,2})/4 + a_2^2m_{i,3}s_{i,2,2} + a_2^2m_{i,4}s_{i,2,2} + (a_4^2m_{i,4}S_{2,2(34)})/4 + (a_3^2m_{i,3}s_{i,2,23})/4 \\
&\quad + a_3^2m_{i,4}s_{i,2,23} + a_1a_3m_{i,3}s_{i,23} + 2a_1a_3m_{i,4}s_{i,23} + a_1a_2m_{i,2}s_{i,2} + 2a_1a_2m_{i,3}s_{i,2} + 2a_1a_2m_{i,4}s_{i,2} \\
&\quad + a_3a_4m_{i,4}s_{i,2,2(34)} + a_2a_3m_{i,3}s_{i,2,23} + 2a_2a_3m_{i,4}s_{i,2,23} + a_1a_4m_{i,4}s_{i,234} + a_2a_4m_{i,4}s_{2,2(34)}) \\
&\quad - (a_4m_{i,4}s_{i,234}\dot{q}_{i,4}(2a_1 + 2a_3c_{i,23} + 2a_2c_{i,2} + a_4c_{i,234}))/2) \\
C_{12} &= -\dot{q}_{i,1}((a_2^2m_{i,2}s_{i,2,2})/4 + a_2^2m_{i,3}s_{i,2,2} + a_2^2m_{i,4}s_{i,2,2} + (a_4^2m_{i,4}S_{2,2(34)})/4 + (a_3^2m_{i,3}s_{i,2,23})/4 \\
&\quad + a_3^2m_{i,4}s_{i,2,23} + a_1a_3m_{i,3}s_{i,23} + 2a_1a_3m_{i,4}s_{i,23} + a_1a_2m_{i,2}s_{i,2} + 2a_1a_2m_{i,3}s_{i,2} + 2a_1a_2m_{i,4}s_{i,2} \\
&\quad + a_3a_4m_{i,4}s_{i,2,2(34)} + a_2a_3m_{i,3}s_{i,2,23} + 2a_2a_3m_{i,4}s_{i,2,23} + a_1a_4m_{i,4}s_{i,234} + a_2a_4m_{i,4}s_{2,2(34)}) \\
C_{13} &= -\dot{q}_{i,1}((m_{i,4}c_1^2(2a_3s_{i,23} + a_4s_{i,234})(2a_1 + 2a_3c_{i,23} + 2a_2c_{i,2} + a_4c_{i,234}))/2 \\
&\quad + (m_{i,4}s_{i,1}^2(2a_3s_{i,23} + a_4s_{i,234})(2a_1 + 2a_3c_{i,23} + 2a_2c_{i,2} + a_4c_{i,234}))/2 \\
&\quad + (a_3m_{i,3}s_{i,23}c_1^2(2a_1 + a_3c_{i,23} + 2a_2c_{i,2}))/2 + (a_3m_{i,3}s_{i,23}s_{i,1}^2(2a_1 + a_3c_{i,23} + 2a_2c_{i,2}))/2) \\
C_{14} &= -(a_4m_{i,4}s_{i,234}\dot{q}_{i,1}(2a_1 + 2a_3c_{i,23} + 2a_2c_{i,2} + a_4c_{i,234}))/2 \\
C_{21} &= \dot{q}_{i,1}((a_2^2m_{i,2}s_{i,2,2})/4 + a_2^2m_{i,3}s_{i,2,2} + a_2^2m_{i,4}s_{i,2,2} \\
&\quad + (a_4^2m_{i,4}S_{2,2(34)})/4 + (a_3^2m_{i,3}s_{i,2,23})/4 + a_3^2m_{i,4}s_{i,2,23} \\
&\quad + a_1a_3m_{i,3}s_{i,23} + 2a_1a_3m_{i,4}s_{i,23} + a_1a_2m_{i,2}s_{i,2} + 2a_1a_2m_{i,3}s_{i,2} \\
&\quad + 2a_1a_2m_{i,4}s_{i,2} + a_3a_4m_{i,4}s_{i,2,2(34)} + a_2a_3m_{i,3}s_{i,2,23} + 2a_2a_3m_{i,4}s_{i,2,23} \\
&\quad + a_1a_4m_{i,4}s_{i,234} + a_2a_4m_{i,4}s_{2,2(34)}) \\
C_{22} &= -a_2\dot{q}_{i,3}(a_4m_{i,4}S_{34} + a_3m_{i,3}s_{i,3} + 2a_3m_{i,4}s_{i,3}) - a_4m_{i,4}(a_2S_{34} + a_3s_{i,4})\dot{q}_{i,4} \\
C_{23} &= -a_2\dot{q}_{i,2}(a_4m_{i,4}S_{34} + a_3m_{i,3}s_{i,3} + 2a_3m_{i,4}s_{i,3}) - a_2\dot{q}_{i,3}(a_4m_{i,4}S_{34} + a_3m_{i,3}s_{i,3} \\
&\quad + 2a_3m_{i,4}s_{i,3}) - a_4m_{i,4}(a_2S_{34} + a_3s_{i,4})\dot{q}_{i,4} \\
C_{24} &= -a_4m_{i,4}(a_2S_{34} + a_3s_{i,4})(\dot{q}_{i,2} + \dot{q}_{i,3} + \dot{q}_{i,4}) \\
C_{31} &= \dot{q}_{i,1}((m_{i,4}c_1^2(2a_3s_{i,23} + a_4s_{i,234})(2a_1 + 2a_3c_{i,23} + 2a_2c_{i,2} + a_4c_{i,234}))/2 \\
&\quad + (m_{i,4}s_{i,1}^2(2a_3s_{i,23} + a_4s_{i,234})(2a_1 + 2a_3c_{i,23} + 2a_2c_{i,2} + a_4c_{i,234}))/2 \\
&\quad + (a_3m_{i,3}s_{i,23}c_1^2(2a_1 + a_3c_{i,23} + 2a_2c_{i,2}))/2 + (a_3m_{i,3}s_{i,23}s_{i,1}^2(2a_1 + a_3c_{i,23} + 2a_2c_{i,2}))/2) \\
C_{32} &= a_2\dot{q}_{i,2}(a_4m_{i,4}S_{34} + a_3m_{i,3}s_{i,3} + 2a_3m_{i,4}s_{i,3}) - a_3a_4m_{i,4}s_{i,4}\dot{q}_{i,4} \\
C_{33} &= -a_3a_4m_{i,4}s_{i,4}\dot{q}_{i,4} \\
C_{34} &= -a_3a_4m_{i,4}s_{i,4}(\dot{q}_{i,2} + \dot{q}_{i,3} + \dot{q}_{i,4}) \\
C_{41} &= (a_4m_{i,4}s_{i,234}\dot{q}_{i,1}(2a_1 + 2a_3c_{i,23} + 2a_2c_{i,2} + a_4c_{i,234}))/2 \\
C_{42} &= a_4m_{i,4}(a_2s_{i,34} + a_3s_{i,4})\dot{q}_{i,2} + a_3a_4m_{i,4}s_{i,4}\dot{q}_{i,3} \\
C_{43} &= a_3a_4m_{i,4}s_{i,4}(\dot{q}_{i,2} + \dot{q}_{i,3}) \\
C_{44} &= 0
\end{aligned}$$

### Gravity Matrix, $G(q_i, \vec{g})$

$$\begin{aligned}
G_1 &= \|\vec{g}\| m_{i,1} (a_1(\vec{g}_y)c_1 - a_1(\vec{g}_x)s_{i,1}) \\
G_2 &= -\|\vec{g}\| m_{i,2} (a_2(\vec{g}_x)c_1 s_{i,2} - a_2 c_{i,2}(\vec{g}_z) + a_2(\vec{g}_y)s_{i,1}s_{i,2}) \\
G_3 &= -\|\vec{g}\| m_{i,3} (a_3 s_{i,23}(\vec{g}_y)s_{i,1} - a_3 c_{i,23}(\vec{g}_z) + a_3 s_{i,23}(\vec{g}_x)c_1) \\
G_4 &= -\|\vec{g}\| m_{i,4} (a_4 s_{i,234}(\vec{g}_x)c_1 - a_4 c_{i,234}(\vec{g}_z) + a_4 s_{i,234}(\vec{g}_y)s_{i,1})
\end{aligned}$$

with  $\vec{g} = [\vec{g}_x, \vec{g}_y, \vec{g}_z]^T \in \Re^3$  being a gravity vector pointing relative to the base-frame  $O_{i,0}$ .

*See Appendix C for a summary of abbreviations.*

## Appendix C

### Summary of Trigonometric Abbreviations

$$\begin{aligned}
s_{i,1} &= \sin(q_{i,1}) \\
c_{i,1} &= \cos(q_{i,1}) \\
s_{i,234} &= \sin(q_{i,2} + q_{i,3} + q_{i,4}) \\
c_{i,234} &= \cos(q_{i,2} + q_{i,3} + q_{i,4}) \\
s_{i,2} &= \sin(q_{i,2}) \\
c_{i,2} &= \cos(q_{i,2}) \\
s_{i,23} &= \sin(q_{i,2} + q_{i,3}) \\
c_{i,23} &= \cos(q_{i,2} + q_{i,3}) \\
s_{i,2.2} &= \sin(2(q_{i,2})) \\
c_{i,2.2} &= \cos(2(q_{i,2})) \\
s_{i,2.23} &= \sin(2(q_{i,2} + q_{i,3})) \\
c_{i,2.23} &= \cos(2(q_{i,2} + q_{i,3})) \\
s_{i,2.2(34)} &= \sin(2q_{i,2} + (q_{i,3} + q_{i,4})) \\
c_{i,2.2(34)} &= \cos(2q_{i,2} + (q_{i,3} + q_{i,4}))
\end{aligned}$$

where

$$q_i = [q_{i,1}, q_{i,2}, q_{i,3}, q_{i,4}]^T \in \Re^4$$

is a vector of joint variables corresponding to each  $i^{th}$  leg.

- [1] R.B. McGhee and A.A. Frank. On the stability properties of quadruped creeping gaits. *Mathematical Biosciences*, 3(0):331 – 351, 1968.
- [2] J.K. Hodgins and M. Raibert. Adjusting step length for rough terrain locomotion. *IEEE Transactions on Robotics and Automation*, 7(3):289–298, Jun 1991.
- [3] R. Altendorfer, N. Moore, H. Komsuoglu, M. Buehler, Jr. Brown, H.B., D. Mc-Mordie, U. Saranli, R. Full, and D.E. Koditschek. RHex: A Biologically Inspired Hexapod Runner. *Autonomous Robots*, 11(3):207–213, 2001.
- [4] J.Z. Kolter, M.P. Rodgers, and A.Y. Ng. A control architecture for quadruped locomotion over rough terrain. In *IEEE International Conference on Robotics and Automation*, pages 811–818, May 2008.
- [5] Tedrake R. Kuindersma S. Wieber, P.-B. Modeling and control of legged robots. In Siciliano and Khatib, editors, *Springer Handbook of Robotics, 2nd Ed*, Lecture Notes in Control and Information Sciences, chapter 48. Springer Berlin Heidelberg, 2015.
- [6] Y. Fukuoka, H. Kimura, Y. Hada, and K. Takase. Adaptive dynamic walking of a quadruped robot 'Tekken' on irregular terrain using a neural system model. In *IEEE International Conference on Robotics and Automation*, volume 2, pages 2037–2042 vol.2, Sept 2003.
- [7] Joaquin Estremera and Kenneth J. Waldron. Leg Thrust Control for Stabilization of Dynamic Gaits in a Quadruped Robot. In Teresa Zieliska and Cezary Zieliski, editors, *Romansy 16*, volume 487 of *CISM Courses and Lectures*, pages 213–220. Springer Vienna, 2006.
- [8] Marc Raibert, Kevin Blankespoor, Gabriel Nelson, and Rob Playter. BigDog, the Rough-Terrain Quaduped Robot, 2008.
- [9] C. Semini. *HyQ Design and Development of a Hydraulically Actuated Quadruped Robot*. PhD thesis, Apr 2010.
- [10] J.R. Rebula, P.D. Neuhaus, B.V. Bonnlander, M.J. Johnson, and J.E. Pratt. A Controller for the Littledog quadruped walking on Rough Terrain. In *IEEE International Conference on Robotics and Automation*, pages 1467–1473, April 2007.

- [11] M. Ajallooeian, S. Pouya, A Sproewitz, and A.J. Ijspeert. Central Pattern Generators augmented with virtual model control for quadruped rough terrain locomotion. In *IEEE International Conference on Robotics and Automation*, pages 3321–3328, May 2013.
- [12] Simon Rutishauser, A Sprowitz, L. Righetti, and A.J. Ijspeert. Passive compliant quadruped robot using Central Pattern Generators for locomotion control. pages 710–715, Oct 2008.
- [13] Auke Jan Ijspeert. Central pattern generators for locomotion control in animals and robots: A review. *Neural networks*, 21(4), 2008.
- [14] P. Arena. The central pattern generator: a paradigm for artificial locomotion. *Soft Computing*, 4(4):251–266, 2000.
- [15] L. Righetti and A.J. Ijspeert. Programmable central pattern generators: an application to biped locomotion control. pages 1585–1590, May 2006.
- [16] Vitor Matos and Cristina P. Santos. Omnidirectional locomotion in a quadruped robot: A CPG-based approach. In *IEEE/RSJ International Conference on Intelligent Robots and Systems*, pages 3392–3397, Oct 2010.
- [17] G. Endo, J. Morimoto, J. Nakanishi, and G. Cheng. An empirical exploration of a neural oscillator for biped locomotion control. In *Robotics and Automation, 2004. Proceedings. ICRA '04. 2004 IEEE Int. Conf. on*, volume 3, pages 3036–3042 Vol.3, April 2004.
- [18] Paolo Arena. A mechatronic lamprey controlled by analog circuits. In *MED'01 9th Mediterranean Conference on Control and Automation*. IEEE, June 2001.
- [19] Bernhard Klaassen, Ralf Linnemann, Dirk Spenneberg, and Frank Kirchner. Biomimetic walking robot scorpion: Control and modeling. *Robotics and Autonomous Systems*, 41(23):69 – 76, 2002. Ninth International Symposium on Intelligent Robotic Systems.
- [20] P. Arena, L. Fortuna, M. Frasca, and G. Sicurella. An adaptive, self-organizing dynamical system for hierarchical control of bio-inspired locomotion. *Systems, Man, and Cybernetics, Part B: Cybernetics, IEEE Transactions on*, 34(4):1823–1837, Aug 2004.

- [21] Shinkichi Inagaki, Hideo Yuasa, and Tamio Arai. {CPG} model for autonomous decentralized multi-legged robot systemgeneration and transition of oscillation patterns and dynamics of oscillators. *Robotics and Autonomous Systems*, 44(34):171 – 179, 2003. Best papers presented at IAS-7.
- [22] Shinkichi Inagaki, Hideo Yuasa, Takanori Suzuki, and Tamio Arai. Wave {CPG} model for autonomous decentralized multi-legged robot: Gait generation and walking speed control. *Robotics and Autonomous Systems*, 54(2):118 – 126, 2006. Intelligent Autonomous Systems 8th Conference on Intelligent Autonomous Systems (IAS-8).
- [23] A. Billard and A.J. Ijspeert. Biologically inspired neural controllers for motor control in a quadruped robot. In *Neural Networks, 2000. IJCNN 2000, Proceedings of the IEEE-INNS-ENNS International Joint Conference on*, volume 6, pages 637–641 vol.6, 2000.
- [24] Giorgio Brambilla, Jonas Buchli, and AukeJan Ijspeert. Adaptive four legged locomotion control based on nonlinear dynamical systems. In Stefano Nolfi, Gianluca Baldassarre, Raffaele Calabretta, JohnC.T. Hallam, Davide Marocco, Jean-Arcady Meyer, Orazio Miglino, and Domenico Parisi, editors, *From Animals to Animats 9*, volume 4095 of *Lecture Notes in Computer Science*, pages 138–149. Springer Berlin Heidelberg, 2006.
- [25] J. Buchli, F. Iida, and A.J. Ijspeert. Finding resonance: Adaptive frequency oscillators for dynamic legged locomotion. In *Intelligent Robots and Systems, 2006 IEEE/RSJ International Conference on*, pages 3903–3909, Oct 2006.
- [26] K. Tsujita, K. Tsuchiya, and A. Onat. Adaptive gait pattern control of a quadruped locomotion robot. In *Intelligent Robots and Systems, 2001. Proceedings. 2001 IEEE/RSJ International Conference on*, volume 4, pages 2318–2325 vol.4, 2001.
- [27] K. Tsujita, H. Toui, and K. Tsuchiya. Dynamic turning control of a quadruped robot using oscillator network. In *Robotics and Automation, 2004. Proceedings. ICRA '04. 2004 IEEE International Conference on*, volume 3, pages 2613–2618 Vol.3, April 2004.
- [28] Miomir K. Vukobratovi. Contribution to the study of anthropomorphic systems. *Kybernetika*, 08(5):(404)–418, 1972.

- [29] J.-I. Yamaguchi, A. Takanishi, and I. Kato. Development of a biped walking robot compensating for three-axis moment by trunk motion. In *Intelligent Robots and Systems '93, IROS '93. Proceedings of the 1993 IEEE/RSJ International Conference on*, volume 1, pages 561–566 vol.1, Jul 1993.
- [30] P. Sardain and G. Bessonnet. Forces acting on a biped robot. center of pressure-zero moment point. *Trans. Sys. Man Cyber. Part A*, 34(5):630–637, September 2004.
- [31] A. Goswami. Foot rotation indicator (fri) point: a new gait planning tool to evaluate postural stability of biped robots. In *Robotics and Automation, 1999. Proceedings. 1999 IEEE International Conference on*, volume 1, pages 47–52 vol.1, 1999.
- [32] Tsungnan Lin, B.G. Horne, P. Tino, and C.L. Giles. Learning long-term dependencies in NARX recurrent neural networks. *Neural Networks, IEEE Transactions on*, 7(6):1329–1338, Nov 1996.
- [33] Grant P. M. Chen S., Billings S. A. Non-linear system identification using neural networks. In *Int. Journal of Control*, volume 51 of *Lecture Notes in Control and Information Sciences*, pages 1191–1214. Taylor and Francis, 1990.
- [34] Salah El Hihi and Yoshua Bengio. Hierarchical recurrent neural networks for long-term dependencies, 1996.
- [35] S. A Billings. *Nonlinear system identification : NARMAX methods in the time, frequency, and spatio-temporal domains*. John Wiley and Sons Ltd, 2013.
- [36] Oliver Nelles. Neural networks with internal dynamics. In *Nonlinear System Identification*, pages 645–651. Springer Berlin Heidelberg, 2001.
- [37] David E. Rumelhart, Geoffrey E. Hinton, and Ronald J. Williams. Neurocomputing: Foundations of research. chapter Learning Representations by Backpropagating Errors, pages 696–699. MIT Press, Cambridge, MA, USA, 1988.
- [38] David E. Rumelhart, Richard Durbin, Richard Golden, and Yves Chauvin. Backpropagation. chapter Backpropagation: The Basic Theory, pages 1–34. L. Erlbaum Associates Inc., Hillsdale, NJ, USA, 1995.

- [39] Raúl Rojas. The backpropagation algorithm. In *Neural Networks: A Systematic Introduction*, chapter 7. Springer-Verlag New York, Inc., New York, NY, USA, 1996.
- [40] N. Hogan. Impedance control: An approach to manipulation. In *American Control Conference, 1984*, pages 304–313, June 1984.
- [41] Y. Koren and J. Borenstein. Potential field methods and their inherent limitations for mobile robot navigation. In *Robotics and Automation, 1991. Proceedings., 1991 IEEE International Conference on*, pages 1398–1404 vol.2, Apr 1991.
- [42] F. Arambula Coso and M.A. Padilla Castaeda. Autonomous robot navigation using adaptive potential fields. *Mathematical and Computer Modelling*, 40(910):1141 – 1156, 2004.
- [43] P. Krishnamurthy and F. Khorrami. Godzilla: A low-resource algorithm for path planning in unknown environments. *Journal of Intelligent and Robotic Systems*, 48(3):357–373, 2007.
- [44] Radu Bogdan Rusu. *Semantic 3D Object Maps for Everyday Manipulation in Human Living Environments*. PhD thesis, Computer Science department, Technische Universitaet Muenchen, Germany, October 2009.
- [45] Radu Bogdan Rusu and Steve Cousins. 3D is here: Point Cloud Library (PCL). In *IEEE International Conference on Robotics and Automation (ICRA)*, Shanghai, China, May 9-13 2011.
- [46] K. Pearson. On lines and planes of closest fit to systems of points in space. *Philosophical Magazine*, 2(6):559–572, 1901.
- [47] Alberto Demichelis. Squirrel, the programming language, 2011.
- [48] G. Bradski. *Dr. Dobb's Journal of Software Tools*.
- [49] Beman Dawes. Boost C++ Libraries, 2005. [Online; <http://www.boost.org/>].
- [50] wxWidgets, Cross-Platform GUI Library, 2015. [Online; <https://www.wxwidgets.org/>].
- [51] P.-B. Wieber. Holonomy and nonholonomy in the dynamics of articulated motion. In Moritz Diehl and Katja Mombaur, editors, *Fast Motions in Biomechanics and*

- Robotics*, volume 340 of *Lecture Notes in Control and Information Sciences*, pages 411–425. Springer Berlin Heidelberg, 2006.
- [52] Russel Smith. Open Dynamics Engine, 2008. [Online; <http://www.ode.org/>].
  - [53] Kiyotoshi Matsuoka. Sustained oscillations generated by mutually inhibiting neurons with adaptation. *Biological Cybernetics*, 52(6):367–376, 1985.
  - [54] J.J. Collins and Ian Stewart. Hexapodal gaits and coupled nonlinear oscillator models. *Biological Cybernetics*, 68(4):287–298, 1993.
  - [55] Meng Yee (Michael) Chuah Park, Hae-Won and Sangbae Kim. Quadruped bounding control with variable duty cycle via vertical impulse scaling. 2014.
  - [56] Y. Fukuoka, H. Yasushi, and F. Takahiro. A simple rule for quadrupedal gait generation determined by leg loading feedback: a modeling study. *Sci. Rep.*, 5, 2015.
  - [57] Luiz Castro, Cristina P. Santos, Miguel Oliveira, and Auke Ijspeert. Postural Control on a Quadruped Robot Using Lateral Tilt: A Dynamical System Approach. In Herman Bruyninckx, Libor Peuil, and Miroslav Kulich, editors, *European Robotics Symposium 2008*, volume 44 of *Springer Tracts in Advanced Robotics*, pages 205–214. Springer Berlin Heidelberg, 2008.
  - [58] Jia-wang Li, Chao Wu, and Tong Ge. Central pattern generator based gait control for planar quadruped robots. *Journal of Shanghai Jiaotong University*, 19(1):1–10, 2014.
  - [59] S. Kajita, F. Kanehiro, K. Kaneko, K. Fujiwara, K. Harada, K. Yokoi, and H. Hirukawa. Biped walking pattern generation by using preview control of zero-moment point. In *IEEE International Conference on Robotics and Automation*, volume 2, pages 1620–1626 vol.2, Sept 2003.
  - [60] Katie Byl, Alec Shkolnik, Sam Prentice, Nick Roy, and Russ Tedrake. Reliable Dynamic Motions for a Stiff Quadruped. *International Symposium on Experimental Robotics*, pages 319–328, 2009.
  - [61] A. Takanishi, M. Tochizawa, T. Takeya, H. Karaki, and I. Kato. Realization of dynamic biped walking stabilized with trunk motion under known external force.

In KennethJ. Waldron, editor, *Advanced Robotics: 1989*, pages 299–310. Springer Berlin Heidelberg, 1989.

- [62] R. Kurazume, T. Hasegawa, and K. Yoneda. The sway compensation trajectory for a biped robot. In *Robotics and Automation, 2003. Proceedings. ICRA '03. IEEE International Conference on*, volume 1, pages 925–931 vol.1, Sept 2003.
- [63] Roberto Battiti. First and second-order methods for learning: between steepest descent and newton's method. *Neural Computation*, 4:141–166, 1992.
- [64] G. D. Magoulas, M. N. Vrahatis, and G. S. Androutsakis. Improving the convergence of the backpropagation algorithm using learning rate adaptation methods. *Neural Comput.*, 11(7):1769–1796, oct 1999.
- [65] S. Nissen. Implementation of a fast artificial neural network library (FANN). Technical report, Department of Computer Science University of Copenhagen (DIKU), 2003. <http://fann.sf.net>.
- [66] G. Bradski and A. Kaehler. *Learning OpenCV*, chapter Image Morphology. O'Reilly Media, 2008.
- [67] P.E. Hart, N.J. Nilsson, and B. Raphael. A formal basis for the heuristic determination of minimum cost paths. *Systems Science and Cybernetics, IEEE Transactions on*, 4(2):100–107, July 1968.
- [68] Niloy J. Mitra and An Nguyen. Estimating surface normals in noisy point cloud data. In *Proceedings of the Nineteenth Annual Symposium on Computational Geometry*, SCG '03, pages 322–328, New York, NY, USA, 2003. ACM.
- [69] Edward Castillo, Jian Liang, and Hongkai Zhao. Point cloud segmentation and denoising via constrained nonlinear least squares normal estimates. In Michael Breu, Alfred Bruckstein, and Petros Maragos, editors, *Innovations for Shape Analysis, Mathematics and Visualization*, pages 283–299. Springer Berlin Heidelberg, 2013.
- [70] J.Z. Kolter, Youngjun Kim, and A.Y. Ng. Stereo vision and terrain modeling for quadruped robots. In *Robotics and Automation, 2009. ICRA '09. IEEE International Conference on*, pages 1557–1564, May 2009.